Optimisation and control of shear flows

by

Antonios Monokrousos

May 2011 Technical Report Linné Flow Centre KTH, Mechanics Royal Institute of Technology SE-100 44 Stockholm, Sweden Akademisk avhandling som med tillstånd av Kungliga Tekniska Högskolan i Stockholm framlägges till offentlig granskning för avläggande av teknologie doktorsexamen fredagen den 27 Maj 2011 kl
 10:00 i K1, Kungliga Tekniska Högskolan, Lindstedtsv. 5 (D3), Entréplan, Stockholm. ${\hbox{\Large @}}$ Antonios Monokrousos 2011 Universitetsservice US–AB, Stockholm 2011

Optimisation and control of shear flows

Antonios Monokrousos

Linné Flow Centre, Department of Mechanics, Royal Institute of Technology (KTH)

SE-100 44 Stockholm, Sweden

Abstract

Transition to turbulence and flow control are studied by means of numerical simulations for different simple shear flows. Linear and non-linear optimisation methods using the Lagrange multiplier technique are employed.

In the linear framework as objective function the standard disturbance kinetic energy is chosen and the constraints involve the linearised Navier—Stokes equations. We consider both the optimal initial condition leading to the largest disturbance energy growth at finite times and the optimal time-periodic forcing leading to the largest asymptotic response for the case of the flat plate boundary layer excluding the leading edge. The optimal disturbances for spanwise wavelengths of the order of the boundary layer thickness are streamwise vortices exploiting the lift-up mechanism to create streaks. For long spanwise wavelengths it is the Orr mechanism combined with the amplification of oblique wave packets that is responsible for the disturbance growth. Also linear optimal disturbances are computed around a leading edge and the effect of the geometry is considered. It is found that two-dimentional disturbances originating upstream, relative to the leading edge of the plate are inefficient at generating a viable disturbance, while three dimentional disturbances are more amplified.

In the non-linear framework a new approach using ideas from non-equilibrium thermodynamics is developed. We determine the initial condition on the laminar/turbulent boundary closest to the laminar state. Starting from the general evolution criterion of non-equilibrium systems we propose a method to optimise the route to the statistically steady turbulent state, i.e. the state characterised by the largest entropy production. This is the first time information from the fully turbulent state is included in the optimisation procedure. The method is applied to plane Couette flow. We show that the optimal initial condition is localised in space for realistic flow domains, while the disturbance visits bent streaks before breakdown.

Feedback control is applied to the bypass-transition scenario with high levels of free-stream turbulence. The flow is the flat-plate boundary layer. In this scenario low frequency perturbations enter the boundary layer and streamwise elongated disturbances emerge due to non-modal growth. The so-called streaky structures are growing in amplitude until they reach high enough energy levels and break down into turbulent spots via their secondary instability. When control is applied in the form of wall blowing and suction, the growth of the streaks is delayed, which implies a delay of the whole transition process. Additionally,

a comparison with experimental work is performed demonstrating a remarkable agreement in the disturbance attenuation once the differences between the numerical and experimental setup are reduced.

Open-loop control with wall travelling waves by means of blowing and suction is applied to a separating boundary layer. For downstream travelling waves we obtain a mitigation of the separation of the boundary layer while for upstream travelling waves a significant delay in the transition location accompanied by a modest reduction of the separated region.

Descriptors: shear flows, flow control, optimal disturbances, Lagrange method, transition to turbulence, non-linear dynamics

Preface

This thesis deals with optimisation and control of shear flows. The main advisor for the project is Prof. Dan Henningson. Prof. Luca Brandt has acted as co-advisor. A brief overview of the basic concepts and methods is presented in the first part. The second part is a collection of the following articles:

Paper 1.

A. Monokrousos, E. Åkervik, L. Brandt & D. S. Henningson, 2010 Global three-dimentional optimal disturbances in the Blasius boundary-layer flow using time-steppers. *J. Fluid Mech.* 650, 181-214

Paper 2.

A. Monokrousos, L. Brandt, C. Mavriplis & D. S. Henningson, 2011 Optimal disturbances above and upstream a flat plate with an elliptic leading edge. $Technical\ report$

Paper 3.

A. Monokrousos, A. Bottaro, L. Brandt, A. Di Vita & D. S. Henningson, 2011

Non-equilibrium thermodynamics and the optimal path to turbulence in shear flows. *Phys. Rev. Lett.* 106, 134502

Paper 4.

A. Monokrousos, L. Brandt, P. Schlatter & D. S. Henningson, 2008 DNS and LES of estimation and control of transition in boundary layers subject to free-stream turbulence. *Int. J. Heat and Fluid Flow*, 29, *Issue 3 841-855*

Paper 5.

A. Monokrousos, F. Lundell & L. Brandt, 2010

Feedback control of boundary layer bypass transition: comparison of a numerical study with experiments. AIAA J., 48 (8), 1848-1851

Paper 6.

A. Monokrousos & L. Brandt, 2011

Control of a separating boundary layer with travelling waves on the wall. $Technical\ report$

V



Κι αν πτωχική την βρεις, η Ιθάκη δεν σε γέλασε. Έτσι σοφός που έγινες, με τόση πείρα, ήδη θα το κατάλαβες η Ιθάκες τι σημαίνουν.

Κωνσταντίνος Π. Καβάφης (1863–1933)

Abstract	iii
Preface	V
Part I	1
Chapter 1. Introduction	2
Chapter 2. Theoretical Background 2.1. Governing Equations 2.2. State-Space Formulation 2.3. Objective Function and the Lagrangian Approach 2.4. Flow Cases	4 4 5 6 7
Chapter 3. Optimal Disturbances 3.1. Linear Optimal Disturbances 3.2. Non-linear Optimal Disturbances	11 11 15
Chapter 4. Flow Control 4.1. Feedback Control 4.2. Open-loop Control	20 20 26
Chapter 5. Numerical Codes 5.1. Simson 5.2. Nek5000	27 27 27
Chapter 6. Conclusions and Outlook	29
Chapter 7. Summary of papers and division of work between authors	31
Acknowledgements	35
Bibliography	37
Part II	39
Paper 1. Global optimal disturbances in the Blasius boundary- layer flow using time-steppers	41
Paper 2. Optimal disturbances above and upstream a flat plate with an elliptic leading edge	85
Paper 3. Non-equilibrium thermodynamics and the optimal path to turbulence in shear flows	103

Paper 4.	DNS and LES of estimation and control of transition in			
	boundary layers subject to free-stream turbulence	115		
Paper 5.	Feedback control of boundary layer bypass transition	a:		
	Experimental and numerical progress	153		

Paper 6. Control of a separating boundary Layer with travelling waves on the wall

Part I Introduction

CHAPTER 1

Introduction

Fluids are all around us. We experience them in all kind of manners and ways. We jump into the water for a swim and feel how it is opposing us but at the same time keeping us afloat; we feel the wind around us when we run or bike, we throw a flat stone in the lake and watch it bouncing a few times before it sinks; we have a sip from a glass of red wine. However, hardly ever we realise and even less often we understand the complicated phenomena taking place within them.

It always amazes me how we are able to conceive and describe immense processes, light years away, like the birth of a star or its cataclysmic death or we have theories that can explain microscopic phenomena like few sub-atomic particles interacting and combining to give us a huge variety of elements found in nature; yet again something so familiar and commonplace like the flow of the water out of an open tap or down a small stream elude us: suddenly and for no apparent reason the simple smooth laminar flow turns into a chaotic and turbulent motion.

The shift of a flow from the laminar to turbulent state is called transition to turbulence and it has been the subject of study for more than a century. This thesis deals with problems of the kind and also attempts to shed some light on how to apply *control* and try to prevent a transition like the one described above. However, the more complicated the flow configuration becomes *i.e.* the geometrical and physical characteristics of the solid objects that the fluid interacts with, the less intuitive or apparent the transition mechanisms are.

In real flows often (but not always) the transition is initiated by small amplitude perturbations and we can assume that their dynamics can be described, at least at an initial stage, by linear theory. However, whether transition will occur or not does not depend solely on the perturbation amplitude but also on its shape in space. Thus, there must be some perturbations that are more efficient at initiating transition than others. These are called *optimal disturbances* and they can help us understand the transition process.

The scientific questions of how and why we get transition to turbulence are sometimes replaced with the more engineering type of questions of when and where; we are more interested in quantifying the phenomenon than explaining it. Answering the first questions might be tedious and long and in the end we

may get no real answer. However, if do manage to get answers, it becomes much easier to address the engineering problem. In the long run it will be worth the effort. However, what I believe really matters, even if final answers elude or disappoint us, is the "journey" and how we learnt of new things we would never have thought to look for in the first place.

CHAPTER 2

Theoretical background

2.1. Governing equations

This thesis is concerned with the stability, transition and control of simple shear flows subject to external disturbances. The system of partial differential equations (PDE) used to model the flow are the incompressible Navier-Stokes equations:

$$\partial_t \mathbf{u} + (\mathbf{u} \cdot \nabla) \mathbf{u} = -\nabla p + Re^{-1} \Delta \mathbf{u} + \mathbf{f},$$
 (2.1)

$$\nabla \cdot \mathbf{u} = 0, \tag{2.2}$$

where $\mathbf{u} = (u(\mathbf{x},t),v(\mathbf{x},t),w(\mathbf{x},t))^T$ is the velocity field and p the pressure. All the quantities are non-dimensionalised with respect to some typical length and velocity scale present in the flow. The term \mathbf{f} is a forcing function that can assume different roles. For instance, we apply flow control or seek optimal forcing functions. Re is the Reynolds number which is defined:

$$Re = \frac{UL}{\nu} \,. \tag{2.3}$$

U and L are velocity and length scales while ν is the kinematic viscosity of the fluid.

In some cases we choose to assume perturbations of small amplitude that evolve around a steady base flow. The equations that describe the dynamics of these perturbations are a linearised version of 2.1. The use of optimisation theory along with a linear system of governing equations gives us insight on the mechanisms that bring an infinitesimal disturbance to finite amplitudes and potentially trigger transition to turbulence. The model describing the dynamics of these small perturbations are therefore the linearised Navier-Stokes equations,

$$\partial_t \mathbf{u}' + (\mathbf{U} \cdot \nabla) \mathbf{u}' + (\mathbf{u}' \cdot \nabla) \mathbf{U} = -\nabla p + Re^{-1} \Delta \mathbf{u}' + \mathbf{f},$$
 (2.4)

$$\nabla \cdot \mathbf{u}' = 0, \tag{2.5}$$

where $\mathbf{U}=(U(\mathbf{x}),V(\mathbf{x}),W(\mathbf{x}))^T$ is the base flow we study and $\mathbf{u}'=(u(\mathbf{x},t),v(\mathbf{x},t),w(\mathbf{x},t))^T$ is the small perturbation representing the departure from the base flow. $\mathbf{u}=\mathbf{U}+\mathbf{u}'$ would be the total velocity vector. $\mathbf{x}=(x,y,z)^T$ is the spatial position vector where x corresponds to the streamwise, y to the wall-normal and z to the spanwise direction. In the cases studied here all the base flows have at least one homogeneous direction, so they can be written:

 $\mathbf{U} = (U(x,y),V(x,y),0)^T$. This allows us to consider Fourier decomposition along the spanwise direction and treat each Fourier mode independently. This reduces a big three-dimensional problem into several smaller two-dimensional ones which from the computational standpoint is advantageous.

In the rest of this introduction we will drop the primes and use \mathbf{u} as our main variable. In the studies based on linear theory, \mathbf{u} will be perturbation from the base flow while in the non-linear case \mathbf{u} will be the total velocity field, base flow plus perturbation.

2.2. State-Space formulation

As it can also be seen from equations (2.4) and (2.5) for incompressible flows the pressure only acts as a Lagrange multiplier to enforce the constrain of divergence-free velocity fields. The pressure itself can be formally expressed as a function of the velocity vector $\mathbf{u} = (u, v, w)^T$ enabling the use of \mathbf{u} as the state variable and to re-write the equations in a compact form (Kreiss *et al.* 1994). The momentum part of the forced linearized Navier–Stokes equations can be written as

$$\partial_t \mathbf{u} = -(\mathbf{U} \cdot \nabla)\mathbf{u} - (\mathbf{u} \cdot \nabla)\mathbf{U} + Re^{-1}\Delta\mathbf{u} + \nabla p + \mathbf{f}, \tag{2.6}$$

where the pressure is a known function of the divergence-free velocity field ${\bf u}$ and base flow ${\bf U}$

$$\Delta p = -\nabla \cdot ((\mathbf{U} \cdot \nabla)\mathbf{u} + (\mathbf{u} \cdot \nabla)\mathbf{U}). \tag{2.7}$$

Inversion of the Laplacian requires boundary conditions and formally we may obtain these by projecting (2.6) on the outwards pointing normal of the domain \mathbf{n} . The solution of (2.7) is denoted as $p = \mathcal{K}\mathbf{u}$ so we have with the following expression for the system operator

$$\mathcal{A} = -(\mathbf{U} \cdot \nabla) - (\nabla \mathbf{U}) + Re^{-1}\Delta + \nabla \mathcal{K}. \tag{2.8}$$

The resulting state space formulation of equation (2.6) reads

$$(\partial_t - \mathcal{A})\mathbf{u} - \mathbf{f} = 0, \quad \mathbf{u}(0) = \mathbf{u}_0, \tag{2.9}$$

with solution

$$\mathbf{u}(t) = \underbrace{\exp(\mathcal{A}t)\mathbf{u}_0}_{\text{initial value problem}} + \underbrace{\int_0^t \exp(\mathcal{A}\tau)\mathbf{f}(\mathbf{x}, t - \tau) \,d\tau}_{\text{forced problem}}.$$
 (2.10)

Alternatively \mathcal{A} may also be defined using semi-group theory, where it is referred to as an infinitesimal generator. First, the evolution operator $\mathcal{T}(t)$ is defined as the operator that maps a solution at time t_0 to time $t_0 + t$.

$$\mathbf{u}(t+t_0) = \mathcal{T}(t)\mathbf{u}(t_0). \tag{2.11}$$

The infinitesimal generator of $\mathcal{T}(t)$, \mathcal{A} , is defined through the action of \mathcal{T} for an infinitesimal amount of time δt

$$A\mathbf{u} = \lim_{\delta t \to 0} \frac{\mathcal{T}(\delta t)\mathbf{u} - \mathbf{u}}{\delta t}.$$
 (2.12)

See also Trefethen et al. (1993) and Bagheri et al. (2009).

2.3. Objective function and the Lagrangian approach

The optimisation method employed here is called the Lagrange approach. The idea originates from classical mechanics where the Lagrangian is an alternative way to write the energy of a dynamical system. Using calculus of variations one seeks minima of the Lagrangian which often correspond to preferred (by the system) states. The method is generalised so that new states (still solutions to the original PDE) are recovered that correspond to extrema of a chosen quantity/functional of the system. Additional constraints, apart from the governing equations themselves, can be added according to the needs of a specific problem. Once the Lagrangian is set-up it is a calculus problem to build a new set of PDEs whose solution not only satisfies the original PDE but is additionally an extremum with respect to the chosen objective. The chosen functional is known as objective function and the method is referred to as the Lagrange multiplier technique.

The objective function we choose depends on the type of problem we aim to solve. When linear theory is employed the standard choice is the kinetic energy of the perturbation field since this indicates a measure of the departure from the laminar profile. However, when non-linear optimisation is performed this choice becomes less obvious and other alternatives are explored (see section 3.2). In any case we should always use a quadratic objective function to ensure a well-posed optimisation.

The constraints can be either physical, for instance the need to have a divergence-free velocity field (part of the governing equations) or *ad hoc* like the demand to have an initial condition of unit amplitude. We introduce the norm based on the kinetic energy of the perturbations

$$\|\mathbf{u}(t)\|^2 = (\mathbf{u}(t), \mathbf{u}(t)) = \int_{\Omega} \mathbf{u}^H \mathbf{u} \, d\Omega.$$
 (2.13)

The general form of the Lagrangian used throughout this thesis is

$$\mathcal{L} = (\text{Objective function}) - (\mathbf{u}^*, (\text{Gov. Eqs})) - (\sigma, (\text{Additional constraints}))$$

The quantities \mathbf{u}^* and σ are called Lagrange multipliers and they are part of the final system of PDEs. The Lagrange multiplier \mathbf{u}^* , attached to the governing equations, is a solution to a PDE similar to the original governing equations and is called the *adjoint* variable or co-state variable.

We apply this method to both the linear and non-linear problem. For the linear case we study two types of problems. One is finding optimal perturbations, that is structures in the flow that lead to final states with the maximum disturbance energy while the other is designing controllers that when applied to a flow minimise the perturbation kinetic energy of the system.

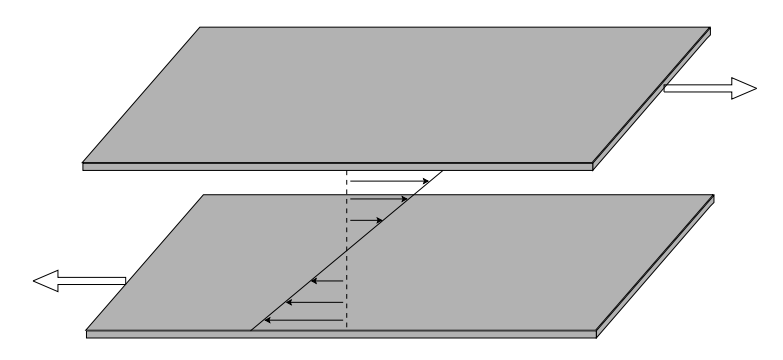


FIGURE 2.1. The plane Couette flow. The large white arrows indicate the direction of the moving walls. The thin arrows indicate the linear variation of the velocity as one moves from the lower wall to the upper.

2.4. Flow cases

We consider various shear flows. In some projects the interest is shifted towards very simple generic flow cases where understanding of the mechanisms is relatively easy or intuitive since new ideas are tested in terms of methodology. In others, well established methods were used and the interest is more towards applying them to complex problems where physical understanding is lacking.

All the flow cases fall under the category of "simple shear flows" where direct numerical simulations (DNS) and well-resolved large eddy simulations (LES) are possible. In particular we studied Couette flow, flat-plate-boundary layer flow, leading edge flow and a case of separating boundary layer flow. A short description of each follows.

2.4.1. Plane Couette flow

Plane Couette flow is a shear flow that is created in a channel between two infinitely wide and long parallel walls that move towards opposite directions with a constant speed U. It is arguably the simplest wall-bounded shear flow. There is only one inhomogeneous direction (the wall-normal) and the profile for the laminar case is a linear function of the distance from the wall. Additionally it can be shown that for any Reynolds number it is asymptotically stable i.e. linear perturbations eventually decay. In practise, when simulating numerically this flow the domain is truncated and periodic boundary conditions are imposed along the wall-normal directions.

The computational domain is a rectangular box:

$$\Omega = [-\frac{L_x}{2}, \frac{L_x}{2}] \times [-h, h] \times [-\frac{L_z}{2}, \frac{L_z}{2}]$$

where L_x and L_z are the lengths of the domain in the two wall-parallel directions and h the half-width of the channel. We assume Dirichlet boundary conditions on the two walls with the streamwise velocity $\mathbf{u}|_{y=\pm h} = (\pm U, 0, 0)^T$

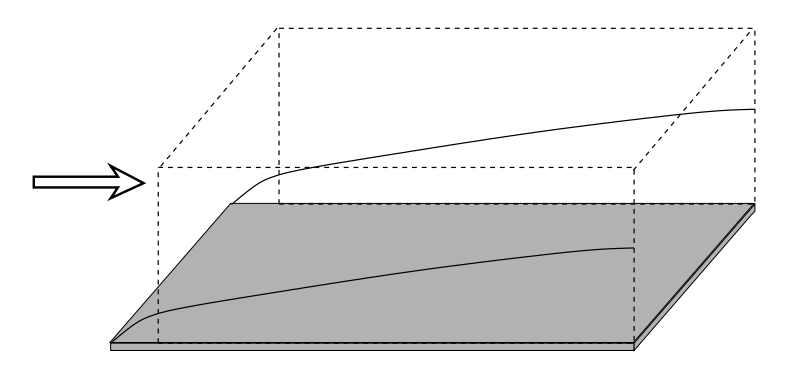


FIGURE 2.2. The boundary layer flow. The dashed lines indicate the computational box. The arrow shows the direction of the flow.

and periodic conditions along the wall-normal directions. The bulk Reynolds number is defined:

$$Re = \frac{Uh}{\nu}$$
.

2.4.2. Flat plate boundary layer flow

The flat plate-boundary-layer flow also known as the Blasius boundary layer is a shear flow with two inhomogeneous directions. This case models the flow above a flat plate excluding the leading edge of the plate. This simplifies substantially the numerical simulation. Our computational box begins some distance downstream from the leading edge and we assume that there is already formed a Blasius boundary layer at the inflow which grows downstream due to viscous diffusion.

Two different Reynolds numbers are commonly used in this flow case. For the most part the Reynolds number based on the displacement thickness δ^* ,

$$Re_{\delta^*} = \frac{U_{\infty}\delta^*}{\nu} \,, \tag{2.14}$$

but also the Reynolds number based on the distance from the leading edge x',

$$Re_x = \frac{U_\infty x'}{\nu} \,, \tag{2.15}$$

are used. ν is the kinematic viscosity.

This flow case is often used as a model for spatially developing flows in contrast to for example Couette flow where the base flow is constant along the flow direction. Another significant difference is that this is an inflow-outflow problem so disturbances are either generated inside the domain or enter the domain from the inflow, develop as they travel downstream and leave the domain through the outflow. From the stability standpoint this flow is a noise amplifier: incoming disturbances extract energy from the base flow exploiting

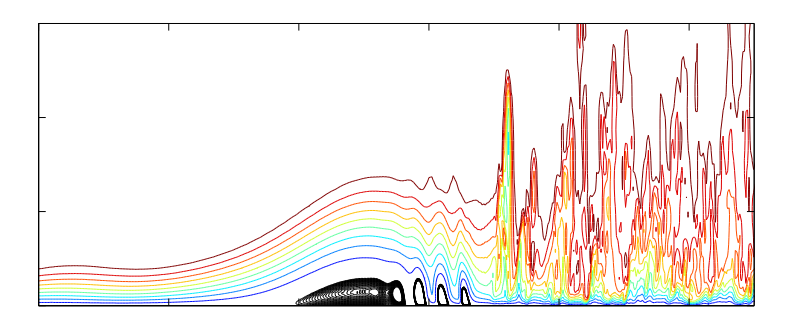


FIGURE 2.3. Flow visualisation of the separated boundary layer flow The streamwise velocity component is shown. The black isocontours mark negative velocities implying the existence of a separation bubble.

its convective instability and amplify until they propagate outside the domain. In this perspective the flow is locally unstable but globally stable.

2.4.3. Leading edge flow

The flow is similar to the previous case but now we include the leading edge of the plate. This adds essentially a geometrical feature which makes the flow case more particular. In the previous cases, the Reynolds number would uniquely characterise the flow. Here the specific shape of the leading edge and its bluntness also affect the flow.

This configuration allows to study how perturbations that originate upstream, outside the boundary layer penetrate and possibly trigger instabilities inside. This flow as well falls in the category of noise amplifiers and is globally stable. The base flow used for the stability analysis is computed by setting up the proper boundary conditions, and time-advancing the non-linear Navier-Stokes until a steady state is obtained. The boundary conditions are obtained by solving the irrotational Euler equations for the far field (Schrader *et al.* 2010).

2.4.4. Separating boundary layer flow

Separating flows are of interest in many applications. For instance, the flow around a bluff body is usually characterised by separation in the wake region which contribute a large portion of the total drag. In that sense one of the most classic examples is the separation of the flow around a cylinder at high Reynolds numbers. From the engineering standpoint separation control can lead to large benefits; in aerodynamics of aeroplane wings it is crucial to prevent separation at high-lift configuration *i.e.* during take-off and landing since this can lead to substantial decrease of the lift force.

Here we want to study a separating flow behind a curved surface of relatively low curvature. This can be modelled simply by considering a flat-plate

10 2. THEORETICAL BACKGROUND

boundary layer and imposing an external pressure gradient, first favourable and then adverse to model the leading and trailing sections of a solid object in the flow. The pressure gradient, chosen carefully, generates a separated region in the trailing section. Once the boundary layer is separated, breakdown to turbulence quickly occurs.

CHAPTER 3

Optimal disturbances

In this chapter the optimisation methods used to compute optimal disturbances are presented. The Lagrange multiplier technique is applied to various type of problems. First we apply the method to compute optimal disturbances that yield a maximum disturbance energy in the linear framework. Second we present an new approach to study transition to turbulence using optimisation in a non-linear setting. We seek the disturbance of minimal initial energy that optimally excites transition to turbulence.

3.1. Linear optimal disturbances

In the linear setting, we are interested in two different types of optimal disturbances. First we seek the initial condition $\mathbf{u}(0)$ that will have the maximum energy amplification at fixed time. Then we consider the spatial structure of the time-periodic forcing \mathbf{f} that creates the largest response at large times, that is when all transients effects have died out. The current analysis will therefore consider flow states induced by forcing or initial conditions, where a flow state is defined by the three-dimensional velocity vector field throughout the computational domain Ω at time t. These disturbances were computed of a flat-plate boundary layer flow, first excluding and then including the leading edge of the plate.

3.1.1. Initial condition

In the following we report the derivation relevant to the optimal initial condition. Here we assume the forcing term \mathbf{f} in (2.9) to be zero, so that only the first term on the right end side of the formal solution (2.10) is of interest. We wish to determine the unit norm initial condition $\mathbf{u}(0)$ yielding the maximum possible energy $(\mathbf{u}(T), \mathbf{u}(T))$ at a prescribed time T. We define the objective function, as the the kinetic energy of the perturbations at time T

$$\mathcal{J} = (\mathbf{u}(T), \mathbf{u}(T)). \tag{3.1}$$

Formally, the task is to maximise the above quadratic measure subject to two constraints: the flow needs to satisfy the governing equations (2.9) (the linearised Navier-Stokes) (without forcing) and the initial condition must have

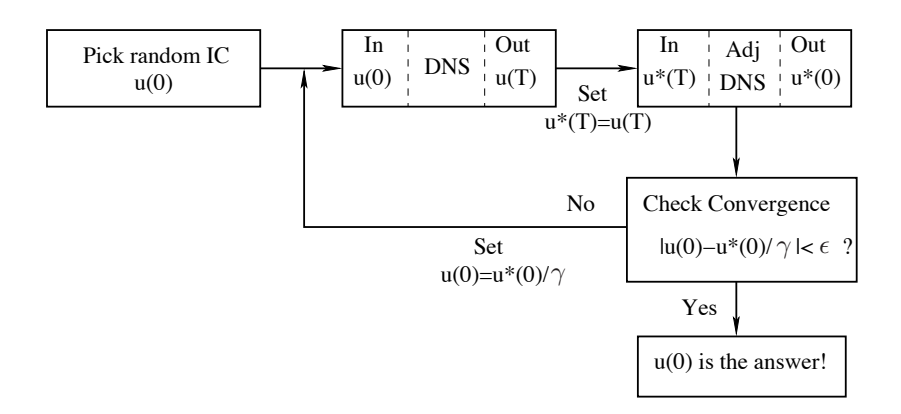


FIGURE 3.1. Power iterations scheme for the linear case.

unit norm $(\mathbf{u}(0), \mathbf{u}(0)) = 1$. By introducing Lagrange multipliers we may formulate an unconstrained optimisation problem for the functional

$$\mathcal{L}(\mathbf{u}, \mathbf{u}^*, \gamma) = (\mathbf{u}(T), \mathbf{u}(T)) - \int_0^T (\mathbf{u}^*, (\partial_t - \mathcal{A}) \mathbf{u}) d\tau - \gamma ((\mathbf{u}(0), \mathbf{u}(0)) - 1).$$
(3.2)

Therefore we need to determine $\mathbf{u}, \mathbf{u}(0), \mathbf{u}(T), \mathbf{u}^*$ and γ such that \mathcal{L} is stationary, necessary condition for first order optimality. Finding the stationary points of \mathcal{L} is equivalent to solving the eigenvalue problem

$$\gamma \mathbf{u}(0) = \exp(\mathcal{A}^{\dagger} T) \exp(\mathcal{A} T) \mathbf{u}(0), \qquad (3.3)$$

where $\exp(A^{\dagger}T)\exp(AT)$ is the forward and adjoint composite propagator whose leading eigenfunction is the optimal initial condition for time T. The iteration scheme above can be seen as a power iteration scheme finding the largest eigenvalue of the problem (3.3). The equations are solved iteratively as described in the block-diagram in figure (3.1). The method is applied in Paper 1.

Additionally the localised initial condition is studied where one chooses a specific region in space and seeks the optimal shape contained within the region (see Paper 1 for a detailed description). A sample result is shown in figure (3.2). It is a three-dimensional localised optimal disturbance for the case of the flat-plate boundary layer. The final time is T=1820. In the figure we plot the three velocity components of the optimal initial condition along with the corresponding response. A disturbance similar to a TS-wave is apparent while characteristic upstream-tilted structure is present in the initial condition. The wave-packet acquires a large initial growth while aligning itself with the wall-normal shear and continues to amplify as it travels downstream exploiting the convective instability of the Blasius boundary layer. Finally, it experiences an energy growth of the order of 1700.

We also computed optimal initial conditions and localised initial conditions for the flow case where the leading edge is included. Due to the geometry the

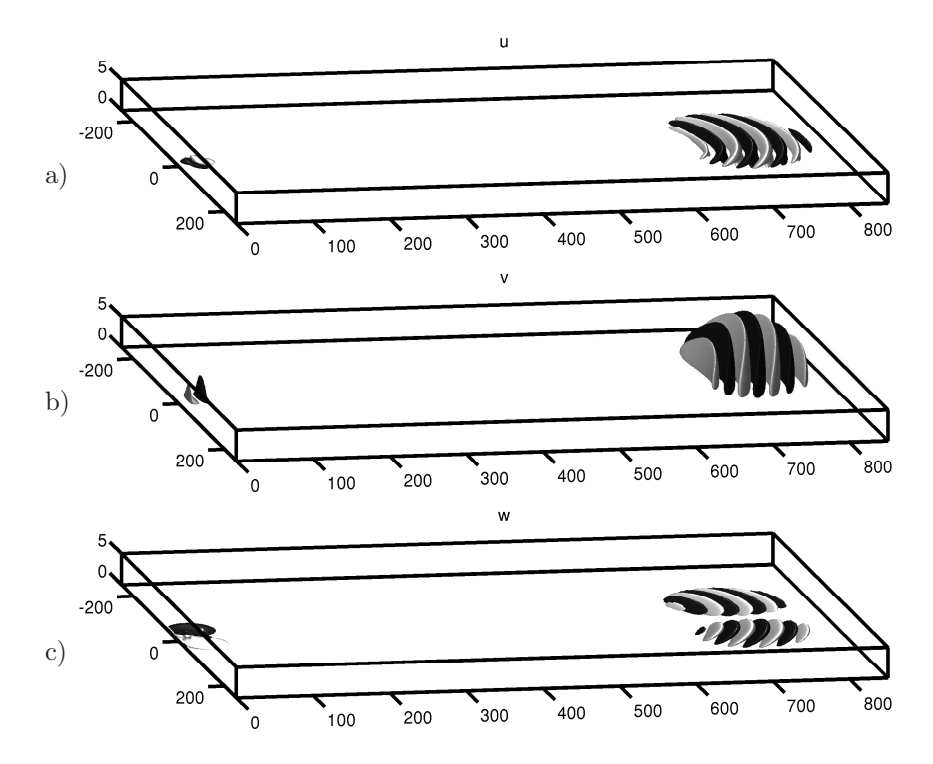


FIGURE 3.2. Optimal initial condition and response for 3d optimals for time T=1820. For the corresponding amplitudes of each structure look at table 1 in Paper 1. Note that we plot both the disturbance and the response in the same figure since they are well separated in space. a) streamwise, b) wall-normal and c) spanwise component.

computational cost of these simulations was significantly higher. Hence we only considered spanwise periodic disturbances. For results and discussion see Paper 2.

3.1.2. Forcing

This section will focus on the regime response of the system to time-periodic forcing. Since the formulation of the optimal forcing problem in this framework is novel we present the derivation of the new system more extensively. We assume zero initial conditions, $\mathbf{u}(0) = 0$, and periodic behaviour of the forcing function, *i.e.*

$$\mathbf{f} = \Re \left(\mathbf{f}(\mathbf{x}) \exp(i\omega t) \right), \quad \mathbf{f} \in \mathbb{C}, \quad \omega \in \mathbb{R},$$
 (3.4)

where \mathbf{f} is the spatial structure of the forcing, ω is its circular frequency and \Re denotes the real part. With these assumptions, the governing equations become

$$(\partial_t - \mathcal{A})\mathbf{u} - \Re\left(\mathbf{f}\exp(i\omega t)\right) = 0, \quad \mathbf{u}(0) = 0. \tag{3.5}$$

We wish to determine the spatial structure of the forcing \mathbf{f} with frequency ω in the limit of large times that maximises the regime response of the flow. The measure of the optimum is again based on the energy norm. We re-formulate the optimisation problem transforming it in the temporal frequency domain, thereby removing the time dependence. We assume time periodic behaviour and \mathbf{u} is replaced by the complex field $\tilde{\mathbf{u}}$ so that

$$\mathbf{u} = \Re \left(\tilde{\mathbf{u}} \exp(i\omega t) \right). \tag{3.6}$$

The resulting governing equations can then be written

$$(i\omega \mathcal{I} - \mathcal{A})\tilde{\mathbf{u}} - \mathbf{f} = 0. \tag{3.7}$$

Note that the spatial operator \mathcal{A} remains unchanged. The objective function is the disturbance kinetic energy of the regime response and the Lagrange function is formulated as follows.

$$\mathcal{L}(\tilde{\mathbf{u}}, \tilde{\mathbf{u}^*}, \gamma, \mathbf{f}) = (\tilde{\mathbf{u}}, \tilde{\mathbf{u}}) - (\tilde{\mathbf{u}^*}, (i\omega\mathcal{I} - \mathcal{A})\tilde{\mathbf{u}} - \mathbf{f}) - \gamma((\mathbf{f}, \mathbf{f}) - 1).$$
(3.8)

The time behaviour of the co-state or adjoint variable is also assumed to be periodic

$$\mathbf{u}^* = \Re\left(\tilde{\mathbf{u}^*} \exp(i\omega t)\right). \tag{3.9}$$

Taking variations of \mathcal{L} with respect to $\tilde{\mathbf{u}}$, $\tilde{\mathbf{u}^*}$, \mathbf{f} and γ gives

$$\delta \mathcal{L} = \left(\frac{\partial \mathcal{L}}{\partial \tilde{\mathbf{u}}^*}, \delta \tilde{\mathbf{u}}^*\right) + \left(\frac{\partial \mathcal{L}}{\partial \tilde{\mathbf{u}}}, \delta \tilde{\mathbf{u}}\right) + \left(\frac{\partial \mathcal{L}}{\partial \gamma}\right) \delta \gamma. \left(\frac{\partial \mathcal{L}}{\partial \mathbf{f}}, \delta \mathbf{f}\right) + \tag{3.10}$$

Finally we set $\delta \mathcal{L} = 0$ and obtain a system of equations

$$\left(\frac{\partial \mathcal{L}}{\partial \tilde{\mathbf{u}^*}}\right) = 0 \to -(i\omega \mathcal{I} - \mathcal{A})\tilde{\mathbf{u}} + \mathbf{f} = 0, \qquad (3.11)$$

$$\left(\frac{\partial \mathcal{L}}{\partial \tilde{\mathbf{u}}}\right) = 0 \to \tilde{\mathbf{u}} - (-i\omega \mathcal{I} - \mathcal{A}^{\dagger})\tilde{\mathbf{u}^*} = 0, \qquad (3.12)$$

$$\left(\frac{\partial \mathcal{L}}{\partial \gamma}\right) = 0 \to (\mathbf{f}, \mathbf{f}) - 1 = 0, \qquad (3.13)$$

$$\left(\frac{\partial \mathcal{L}}{\partial \mathbf{f}}\right) = 0 \to \mathbf{f} = \gamma^{-1} \tilde{\mathbf{u}}^*. \tag{3.14}$$

Equations (3.11) and (3.12) provide the two equations we have to solve, while equation (3.13) gives the normalisation condition and (3.14) provides the optimality condition. It can be shown that the above derivation using the Lagrange multiplier technique is equivalent to the standard matrix method when the resolvent norm is considered

$$\mathbf{f} = \frac{1}{\gamma} (-i\omega I - \mathcal{A}^{\dagger})^{-1} (i\omega I - \mathcal{A})^{-1} \mathbf{f}.$$
 (3.15)

The above formulation leads to matrix-free method for computing the pseudospectra of the given system. This is a new eigenvalue problem defining the spatial structure of the optimal forcing at frequency ω that is solved iteratively; the largest eigenvalue corresponds to the square of the resolvent norm

$$\gamma = \|(i\omega I - A)^{-1}\|^2. \tag{3.16}$$

The regime response for the direct and adjoint system is extracted from the numerical simulations by performing a Fourier transform of the velocity field during one period of the forcing.

The steps of the optimisation algorithm therefore are (similar to figure 3.1):

- (i) Integrate (3.5) forward in time and obtain the Fourier transform response $\tilde{\mathbf{u}}$ at the frequency of the forcing.
- (ii) $\tilde{\mathbf{u}}$ is used as a forcing for the adjoint system which in time domain is written

$$(-\partial_t - \mathcal{A}^{\dagger})\mathbf{u}^* - \Re\left(\tilde{\mathbf{u}}\exp(i\omega t)\right) = 0. \tag{3.17}$$

- (iii) A new forcing function is determined by normalising $\mathbf{f}^{n+1} = \tilde{\mathbf{u}}^*/\gamma$.
- (iv) If $|\mathbf{f}^{n+1} \mathbf{f}^n|$ is larger than a given tolerance, the procedure is repeated.

A sample result is shown in figure (3.3), the optimal forcing structure at spanwise wavenumber $\beta=0.6$ and zero frequency. The flow case is the flat plate boundary layer. The wall-normal and spanwise components of the forcing are displayed in figure (3.3a) and b) while the streamwise component is very weak. In contrast the streamwise velocity component of the response is dominant while the other two components negligible (3.3c). In this case lift-up effect is the prevailing mechanism where counter-rotation vortices parallel to the streamwise direction create streamwise streaks. This mechanism is characterised by strong component-wise energy transfer.

Additionally we computed localised optimal forcing functions with an attempt to compare with results for parabolized stability equations. The formulation is a combination of the localised initial condition and the optimal forcing. However, due to the high computational cost we were restricted only to the spanwise periodic case. A specific region in the streamwise direction is chosen and the optimal shape contained within the region is sought.

3.2. Non-linear optimal disturbances

In some shear flows (pipe, channel and Couette flows) transition is typically subcritical and initial perturbations of finite amplitudes are necessary. So far we have looked at optimisation of the disturbances in a linear framework, which is rather standard and well established method in the field (Schmid & Henningson 2001), and extended it to more complex geometries. This approach assumes that the most natural way to trigger turbulence is to maximise the departure from the base flow in a short time scale. This disturbance amplification will distort the base flow enough to cause breakdown. However, this is not the whole story. It has been shown by Pringle & Kerswell (2010) that linear optimal

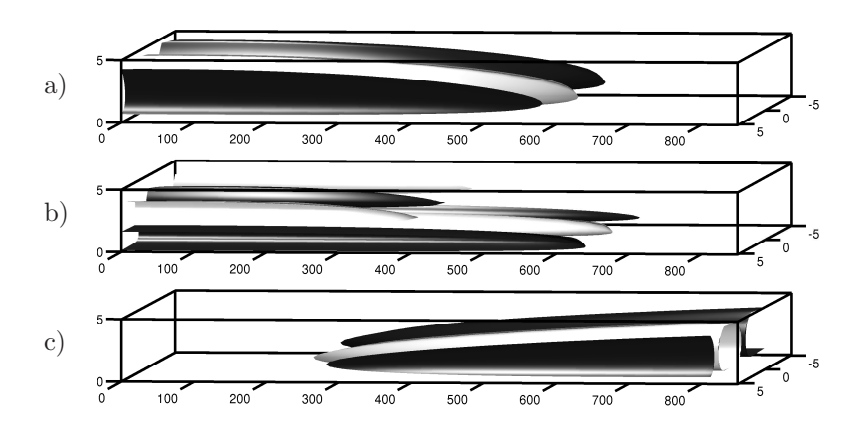


FIGURE 3.3. Isosurfaces of optimal forcing and response for the spanwise wavenumber $\beta=0.6$ subject to steady forcing. a) Wall-normal component of optimal forcing structure. b) Spanwise component of optimal forcing. c) Streamwise velocity component of the flow response. Both the forcing structures and the response are elongated in the streamwise direction.

disturbances are not always efficient to initiate transition to turbulence, and indeed it is often necessary to add noise.

The non-modal approach gives a lot of insight into the physical mechanisms responsible for energy growth in shear flows that experience subcritical transition and, together with weakly nonlinear models such as secondary instability analysis, have contributed to drawing a plausible picture of the early stages of the transition process. However, the later stages are inherently non-linear and linear theory fails.

Another approach that has lately been introduced is performing a similar type of optimisation but replacing the linearised Navier-Stokes with the corresponding non-linear (Pringle & Kerswell 2010; Cherubini *et al.* 2010). In these studies the authors use the full Navier–Stokes equations to show how nonlinearity can change the optimal which emerges from a linear transient growth analysis.

We have proposed a new method to determine the optimal initial condition where we use a non-linear framework and design our optimisation problem considering the fully turbulent field. Following the *General Evolution Criterion* (Glansdorff *et al.* 1964) of non-equilibrium systems, we maximise in a statistical sense the rate of entropy production. The criterion has been used before in a wide range of applications, shock-waves (Rebhan 1990), biology (Juretic & Zupanovic 2003), climate research (Paltridge 1979; Ozawa *et al.* 2003) and nuclear fusion (DiVita & Brusati 1995), although never, thus far, in the search for optimal turbulence-triggering disturbances.

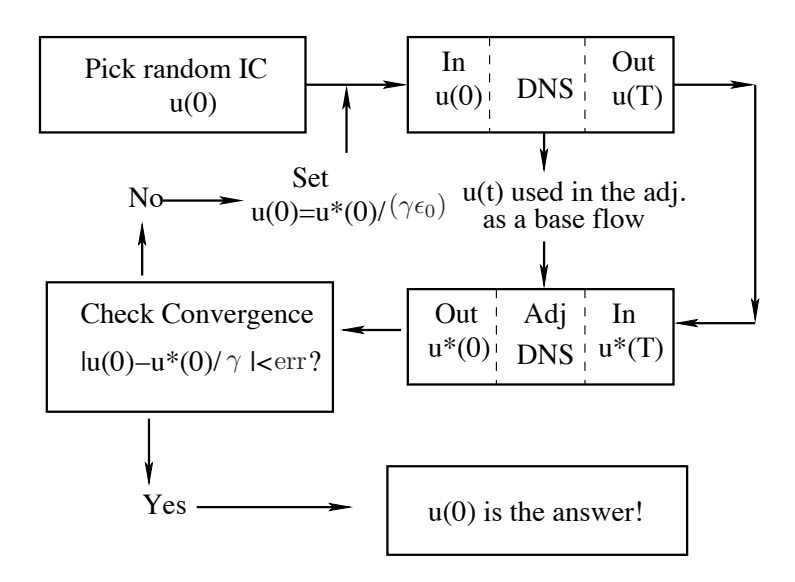


FIGURE 3.4. Power iterations scheme for the non-linear case.

The argument starts from Glansdorff et al. (1964) who demonstrated that for time invariant boundary conditions all systems eventually reach a statistically steady state. All shear flows are in non-equilibrium with their environment since there is continuous energy exchange through the walls and the Navier-Stokes equations can be viewed as a special case of the Boltzmann equation for systems for which the local thermodynamic equilibrium assumption is valid. Hence a fully developed turbulent flow, from the stand point of thermodynamics, is in a statistically steady state. A chaotic turbulent flow is indeed characterised by steady values of (space and time) averaged quantities, like mean velocities and fluctuations. The approach of the fluid system to a statistically steady state is central to the theory presented here.

The general evolution criterion implies that certain quantities obtain extreme values once the statistically steady state is reached. Malkus heuristic principle (Malkus 1956) claims that a viscous, turbulent, incompressible flow in statistically steady state maximises the total rate of viscous dissipation. Thus we choose our Lagrangian for this optimisation problem as:

$$\mathcal{L} = \mathcal{J} - \int_0^T \left[(\mathbf{u}^*, NS(\mathbf{u}))_E + (p^*, \nabla \cdot \mathbf{u})_E \right] dt$$
$$-\lambda(\|\mathbf{u}(0) - \mathbf{U}\|_E^2 - \epsilon_0), \tag{3.18}$$

with the subscript E denoting the energy inner product, *i.e.* the integral over the whole domain as for the case of the disturbance energy. In the above, \mathbf{u}^* , p^* and λ are the Lagrange multipliers, *i.e.* the adjoint variables, NS the nonlinear Navier–Stokes equations, and ϵ_0 the kinetic energy of the perturbation at t=0; \mathbf{u} is the velocity vector and \mathbf{U} the base flow. Since the system under

consideration is chaotic we will maximise the average value of the functional, integrating over a sufficiently long time interval. As introduced above, the objective function is the *time-averaged dissipation*

$$\mathcal{J} = \frac{1}{T} \int_0^T \frac{1}{Re} \left(\nabla \mathbf{u} : \nabla \mathbf{u} \right) dt \tag{3.19}$$

with T the final observation time. Maximising the time integral of the entropy production implies that we also obtain the fastest route to turbulence for any given value of the initial energy ϵ_0 . The equations are solved iteratively like in the linear case with some differences, most crucial, the need to store the full time-dependent velocity field from the forward iteration to be used in the adjoint. The procedure is described in the block-diagram in figure (3.4).

We run the optimisation problem for several values of ϵ_0 starting with a large value for ϵ_0 (where transition to turbulence is guaranteed) run it until convergence and gradually decrease it. At some point the amplitude of the initial condition will not be enough to get to turbulence no matter how long we run the optimisation. We postulate that, the initial condition obtained with this procedure is the one with the smallest possible amplitude that can trigger turbulence.

Including the turbulent field in the optimisation introduces one significant complication, namely the stochastic nature of the turbulent fluctuations render convergence in the standard way impossible. In particular the updated initial condition changes significantly for every iteration even in the proximity of an optimal. Therefore to improve convergence we include a relaxation term

$$\mathbf{u}(0)^{n+1} = (1 - \sigma)\mathbf{u}^*(0)^n + \sigma\mathbf{u}(0)^n, \qquad (3.20)$$

where $\mathbf{u}^*(0)^n$ is the final condition of the adjoint integration from the previous iteration and σ is a small number (here we used 0.05). Close to convergence, the relaxation term gives an ensemble average of the different initial conditions, since the values of the objective function (*i.e.* the statistics of the turbulent state) are basically constant.

This method is applied to the Couette flow where transition is subcritical for all Re. The structure of the initial condition and some intermediate stages of the transition prosses are shown in figure 3.5. The perturbation at t=0 is strongest in the cross-stream velocity components and, most interestingly, it appears localised in all three spatial directions. The initial evolution of the disturbance is reported in figures 3.5(b) and 4(c). The initial disturbance is inclined against the mean shear to extract more energy from the base flow via the Orr-mechanism At time t=10 the disturbance is up-right and still localised.

Transition is initiated by a pair of streamwise vortices that generate a single bent streak Cossu *et al.* (2010), see figure 3.5(c). The slow growth of the streak is associated to a decay of the cross-stream velocity components However, once the streak reaches a sufficient amplitude at $t \approx 70$, secondary instability sets

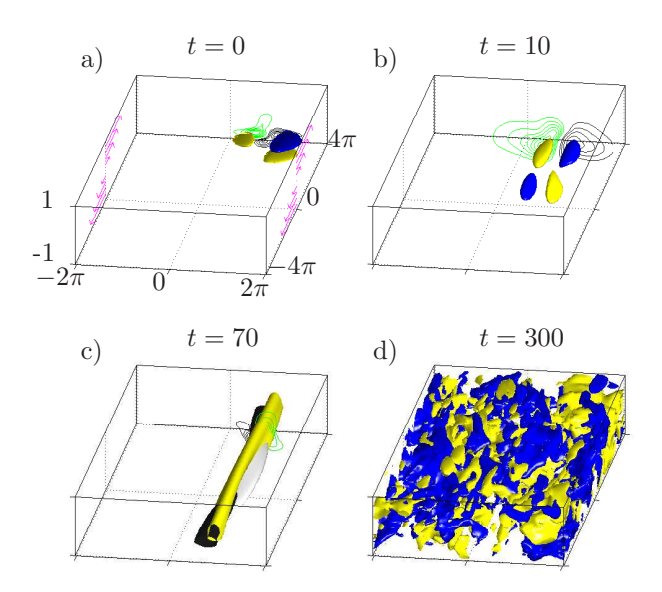


FIGURE 3.5. Optimal initial condition at the threshold level ϵ_{0T} , visualised through isosurfaces of positive and negative streamwise velocity perturbation, shown with pale (yellow) and dark (blue) colour. Contour lines show positive and negative spanwise velocity at $x=1.5\pi$. The base flow is indicated by the arrows along the sides in (a). Re=1500, domain size $4\pi\times2\times2\pi$. The isosurface level is 65% of the maximum value of each component: (a) $u_{max}^2=2.89\times10^{-5}$, (b) $u_{max}^2=2.89\times10^{-5}$, (c) $u_{max}^2=2.09\times10^{-3}$, (d) $u_{max}^2=2.07\times10^{-1}$.

in as spanwise oscillations induced by a staggered pattern of vorticity. Rapid breakdown to turbulence is then observed to occur at $t \approx 130$.

CHAPTER 4

Flow control

Flow control is used to alter the behaviour of a fluid with an active or passive mechanism in order to improve some characteristic. For example in aeroplane wings, vortex generators are added to promote transition to turbulence and reduce the chance of the boundary layer to separate and lead to loss of lift. Control can be divided in two different categories, feedback (or closed-loop) control and open-loop control.

In the case of the feedback control we need to have sensors and actuators and connect them with a control-law. In that case we gain real-time information about the flow state and can adapt our actuation to accommodate any possible changes in the flow. There are various methods to design the control law. Here we are interested in *optimal control*. The Lagrange multiplier technique can be applied to solve the optimal control problem as we solved the optimisation problems in the previous chapter. The objective is disturbance attenuation and transition delay. The problem is divided into two distinct and self-contained problems. This distinction is possible due to the separation principle (Skogestad & Postlethwaite 2005). The first problem is full-information control where assuming full state knowledge of the flow a feedback control signal is computed. Full-state knowledge is a strong requirement and we relax it by including an estimator based on wall measurements. The combination of an estimator and a full information controller is called compensator, where the control law is based on the estimated flow.

In the case of open-loop control we act without any real-time knowledge of the flow. This case can be less effective at times but it is much simpler to implement in a real situation. Usually it is based on physical intuition and empirical knowledge of the flow case it is applied to. We apply the method to a separating boundary layer and study the effect it has on transition to turbulence and as well as on the separation itself.

4.1. Feedback control

4.1.1. Full-information Control

In this section the design process of the full information controller is presented. Therefore it is assumed that the exact state of the system is known. The state-space formulation is adopted,

$$\partial_t \mathbf{u} = \mathcal{A}\mathbf{u} + \mathcal{B}_1 w_1 + \mathcal{B}_2 \phi \,, \tag{4.1}$$

where **u** is the state variable. \mathcal{B}_1w_1 is the forcing due to external excitations w_1 of stochastic nature and $\mathcal{B}_2\phi$ is the forcing from the control signal ϕ . The operator \mathcal{A} governs the dynamics of the augmented system (Chevalier *et al.* 2007a). The control is applied through non-homogeneous boundary conditions as a model for localised blowing and suction at the wall and a lifting procedure is adopted so that the formulation becomes compatible with classical control theory where the control signal is expressed in the equations as a forcing (Högberg & Henningson 2002). In the case of full state-feedback control the signal is calculated directly from the state q so $\mathcal{B}_2\phi = \mathcal{B}_2\mathcal{K}q$ where \mathcal{K} is the control gain.

The aim is to compute the optimal control gain \mathcal{K} so that the kinetic energy of the disturbances is minimised while at the same time the control effort is kept at low levels. To this end the following objective function is defined,

$$\mathscr{F} = \frac{1}{2} \int_0^T \left(\mathbf{u}^H \mathcal{Q} \mathbf{u} + \phi \mathcal{R} \phi \right) dt. \tag{4.2}$$

where $(\cdot)^H$ is the Hermitian transpose. The term $\mathbf{u}\mathcal{Q}\mathbf{u}$ corresponds to the kinetic energy of the perturbations where \mathcal{Q} is the energy norm operator. The second term in equation (4.2) represents the control effort where \mathcal{R} is the actuation penalty.

We apply the Lagrange multiplier technique to find the optimal solution to our problem. The Lagrangian is written as

$$\mathcal{L}(\mathbf{u}, \mathbf{u}^*, \phi) = \int_0^T \left[\frac{1}{2} \left(\mathbf{u}^H \mathcal{Q} \mathbf{u} + \phi \mathcal{R} \phi \right) - \mathbf{u}^* \left(\partial_t \mathbf{u} - \mathcal{A} \mathbf{u} - \mathcal{B}_2 \phi \right) \right] dt, \quad (4.3)$$

where \mathbf{u}^* is, as before the adjoint variable, representing the Lagrange multiplier. The stochastic term B_1w_1 is dropped since the deterministic approach is used for the full information control. The variation of the Lagrangian functional can be written as

$$\delta \mathcal{L} = \left(\frac{\partial \mathcal{L}}{\partial \mathbf{u}}\right) \delta \mathbf{u}^* + \left(\frac{\partial \mathcal{L}}{\partial \mathbf{u}^*}\right) \delta \mathbf{u} + \left(\frac{\partial \mathcal{L}}{\partial \phi}\right) \delta \phi. \tag{4.4}$$

Combining equations (4.3) and (4.4) and assuming $\delta \mathcal{L} = 0$ leads to the set of equations

$$\partial_t \mathbf{u}^* + \mathcal{A}^H \mathbf{u}^* + \mathcal{Q} \mathbf{u} = 0 \tag{4.5a}$$

$$-\partial_t \mathbf{u} + \mathcal{A}\mathbf{u} + \mathcal{B}_2 \phi = 0 \tag{4.5b}$$

$$\mathcal{R}\phi + \mathcal{B}_2^H \mathbf{u}^* = 0. \tag{4.5c}$$

A linear time dependent relation is assumed between the forward solution \mathbf{u} and the Lagrange multiplier $\mathbf{u}^* = X\mathbf{u}$. If we Insert this assumption into equation 4.5a, replace ϕ from equation 4.5b and add equations 4.5a and 4.5b, we arrive at the differential Riccati equation

$$\frac{\partial \mathcal{X}}{\partial t} + \mathcal{A}^H \mathcal{X} + \mathcal{X} \mathcal{A} - \mathcal{X} \mathcal{B}_2 \mathcal{R}^{-1} \mathcal{B}_2^H \mathcal{X} + \mathcal{Q} = 0. \tag{4.6}$$

The optimal \mathcal{K} is then given through the non-negative Hermitian solution \mathcal{X} of equation 4.6. A full derivation of the above equation is given by Lewis & Syrmos (1995). A simplified version arises if an infinite time horizon is assumed, yielding the steady-state Riccati equation

$$\mathcal{A}^{H}\mathcal{X} + \mathcal{X}\mathcal{A} - \mathcal{X}\mathcal{B}_{2}\mathcal{R}^{-1}\mathcal{B}_{2}^{H}\mathcal{X} + \mathcal{Q} = 0.$$

$$(4.7)$$

with the control gain computed from

$$\mathcal{K} = -\mathcal{R}^{-1}\mathcal{B}^H \mathcal{Q} \mathcal{X} \,. \tag{4.8}$$

4.1.2. Estimation

The estimator is designed to approximate the full three-dimensional velocity field from wall measurements in real time. Measurements are taken from the wall and the signal includes noise from the sensors. The estimator can be seen as a filter operator, also termed Kalman filter, where the equations governing the flow are used for the filtering process. Input is the measurements from the real flow and output the estimated flow.

In the estimation problem two flow fields are considered: The 'real' flow and the estimated flow. All the quantities that correspond to the estimated flow are marked with a hat $(\hat{\cdot})$. The estimated field is assumed to fulfil the following equation

$$\frac{\partial \hat{\mathbf{u}}}{\partial t} = \mathcal{A}\hat{\mathbf{u}} - L(r - \hat{r}) + \mathcal{B}_2 \phi, \qquad (4.9)$$

where L is the measurement gain and r indicates the measurements. The latter are extracted through the measurement operator \mathcal{C} and since the measurements process introduces noise, we write $r = \mathcal{C}\mathbf{u} + g$ and $\hat{r} = \mathcal{C}\hat{\mathbf{u}}$, where g is the measurement noise. The derivation below provides us with an operator L which optimally minimises the difference between the real and the estimated flow, namely the estimation error $\tilde{\mathbf{u}} = \mathbf{u} - \hat{\mathbf{u}}$. The governing equation for $\tilde{\mathbf{u}}$ reads

$$\frac{\partial \tilde{\mathbf{u}}}{\partial t} = (\mathcal{A} + L\mathcal{C})\tilde{\mathbf{u}} + \mathcal{B}_1 w_1 + Lg = \mathcal{A}_e \tilde{\mathbf{u}} + \mathcal{B}_1 w_1 + Lg. \tag{4.10}$$

We employ the stochastic approach instead of the deterministic used in the full-information control problem, since the equation is forced by stochastic inputs. We assume that the external disturbances w_1 and g are zero-mean stationary white noise Gaussian processes (Chevalier et al. 2007a). Since the system is forced by these stochastic processes, expected values of the relevant flow quantities are examined. In particular for the estimation problem the covariance of the estimation error, \mathcal{P} (Kailath & Hassibi 2000) is considered and, as for the full information control, a steady state is assumed. The covariance of the error satisfies the algebraic Lyapunov equation

$$\mathcal{A}_e \mathcal{P} + \mathcal{P} \mathcal{A}_e^H + \mathcal{B}_1 \mathcal{W} \mathcal{B}_1^H + L \mathcal{G} L^H = 0, \qquad (4.11)$$

where W and \mathcal{G} are the covariances of w_1 and g respectively. This equation along with the objective function, $\mathcal{F} = \tilde{r}^H \tilde{r}$ (amplitude of the measurement difference) form a new Lagrangian \mathcal{M} where the traces of the covariance matrices

are involved. The trace of covariance matrices correspond to *rms* (root-mean-square) values of the quantity under consideration (Hoepffner *et al.* 2005).

$$\mathcal{M} = trace(\mathcal{P}Q) + trace[\Lambda(\mathcal{A}_e \mathcal{P} + \mathcal{P} \mathcal{A}_e^H + L \mathcal{G} L^H + \mathcal{B}_1 \mathcal{W} \mathcal{B}_1^H)]$$
(4.12)

where Λ is the Lagrange multiplier. The first term in equation (4.12) is the objective function to be minimised and the second is the constraint coming from the Lyapunov equation satisfied by the covariance error. The Riccati equation that arises from optimising \mathcal{P} reads

$$\mathcal{AP} + \mathcal{PA}^H - \mathcal{PC}^H \mathcal{G}^{-1} \mathcal{CP} + \mathcal{B}_1 \mathcal{WB}_1^H = 0, \qquad (4.13)$$

with the estimation feedback gain given by $L = -\mathcal{PC}^H \mathcal{G}^{-1}$. For a similar derivation see also Bagheri *et al.* (2007). In this project the theory above is applied in a highly nonlinear case, where one may use the full (nonlinear) equations when solving the estimation problem (4.9) while the L is computed with the linear theory. This is the extended Kalman filter and it is expected to be more accurate than the standard Kalman filter.

4.1.3. Compensator

The compensator is the combination of full information control and state estimation. The measurements taken from the real flow are communicated to the estimator where they are used to compute the forcing needed to reproduce the perturbations present in the real flow. The actuation signal is computed from the estimated flow and it is applied to both the estimated and the real flow. Although both the control and estimation gains are computed for linear systems, the control and estimation is applied to the full nonlinear Navier-Stokes equations (Högberg et al. 2003c).

The model for the flow employed here is somewhat simplified when compared to the optimal disturbance case. A parallel base flow is assumed and thus the streamwise wavenumbers can be decoupled. Hence we are able to apply a Fourier transform along both the wall-parallel directions. We can treat each wavenumber pair individually and instead of solving one problem with a large number of degrees of freedom, we solve many smaller systems. This necessity arises from the fact that we employ a matrix-based method to solve the Riccati equation which would be intractable for the global problem. This assumption stands as a good approximation due to the slow viscous growth of the boundary layer.

The compensator problem assumes that measurements are taken and actuation is applied continuously over the whole domain. This theory is applied to a spatial boundary layer and both measurements and actuation are available only on a part of the domain (see figure 2 in Paper 4). Two regions need to be specified, one for the control and one for the estimator. For both regions, the local Blasius velocity profile is the base flow in the operator used to solve the problems introduced in the previous section. Once the control and estimation gains are calculated, the actuation forcing is limited to the actuation region by

a smooth transfer function in physical space with two smooth step functions around the chosen locations (Chevalier *et al.* 2007*a*).

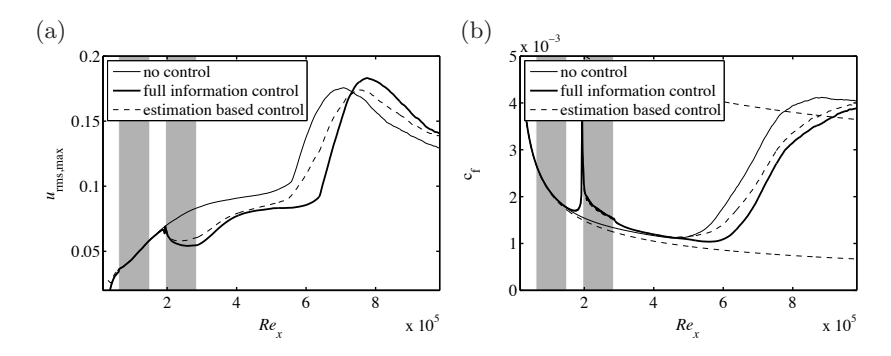


FIGURE 4.1. (a): Wall normal maximum u_{rms} ; (b): skin friction coefficient c_f . No control, ——; Full information control, ——; Compensator, ----. The shaded areas indicate the measurement and actuation region.

In figure 4.1 some sample results are shown. Figure 4.1a shows the wall-normal maximum of the rms-value of the streamwise velocity perturbation for the uncontrolled case and for both full information control and compensation. As observed, the growth of the the streaks is reduced within the control region. However, downstream of the control region, velocity fluctuations continue to grow. This can be explained by the presence of the free-stream turbulence above the boundary layer that is able to induce new perturbations inside the boundary layer.

4.1.4. Approaching the experiment

In this section we describe how we designed a numerical simulation that resembles the experiment done by Lundell (2007). Instead of the opposition control strategy used in the experiment we use the optimal control theory described above.

First we recall the differences between the actuator in the experiment and in the simulations. These pertains the way the control signal is calculated and the area over which control is applied. In the experiment opposition control is adopted where the amplitude of the suction velocity and the time delay between the sensor and the actuator are varied. In the simulation an optimisation of the distributed control is performed and no further tuning is required. Note however that the control signal is computed assuming linearly evolving disturbances and parallel base flow. Secondly, it should be mentioned that the control is active over a large area of the plate where relatively weak blowing/suction is applied in the case of the numerical simulations. Conversely, small holes with strong suction velocity are used in the experiment. Further, in the simulation

we apply control over the full spanwise width of the domain while in the experiment control sets are only stationed near the middle of the plate on an area about 20 mm wide of a total length 450mm.

These differences are reduced and further simulations were performed in order to study how much and if the two cases converge. The control strategy in terms of the way the control signal is calculated is not changed and the focus is put on the geometrical/functioning aspects of the actuator itself. In that context we first remove the blowing and keep only the suction. Then, we restrict the area of actuation to spanwise stripes and limit the streamwise extension of the area where suction is applied. Finally we employ a 'cheaper' control in order to obtain stronger suction to better mimic the experiment.

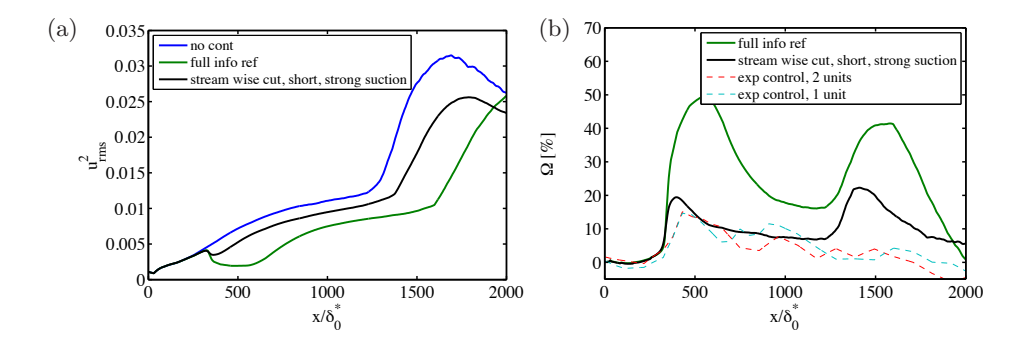


FIGURE 4.2. a) wall-normal maximum of u_{rms} and b) control efficiency Ω . Solid lines are simulations: blue: reference case, green line: control reference case, black line: control with only suction, spanwise and streamwise cut and cheaper control (stronger suction). Dashed lines from experiment.

In figure 4.2 we show the streak growth and the efficiency of the control Ω from the simulation where all the previous restriction on the actuator have been applied. Ω is the relative decrease of the disturbance level in the boundary layer due to the control,

$$\Omega = 1 - \frac{u_{rms,max,on}}{u_{rms,max,off}}.$$
(4.14)

For this case the control effect is similar for both the experiment and the simulation in the region where actuation is applied. However, downstream transition delay is observed only in the numerical control. This can be explained by the fact that in the experiment, control is applied near the middle of the plate and when transition occurs, fully developed turbulence 'invades' the controlled area from the uncontrolled sides.

4.2. Open-loop control

When it comes to flow cases that are more complex and the phenomena are inherently non-linear, the application of linear optimal control in the form presented above is less suitable. Furthermore feedback demands time-resolved knowledge of the flow state which is not always available. A simpler approach can be employed, namely open-loop control where the modifications that are applied in the flow target directly the base flow. In this case no real-time knowledge from the flow state is required and hence no sensors are needed, only actuators.

The case we consider is a separating boundary layer and we apply control with travelling waves on the wall. We investigated the influence of the parameters of the waves (wavenumber, frequency and amplitude) as well as their travelling direction (downstream and upstream).

We find that for a range of parameters the downstream travelling waves are able to eliminate the separation and result to a potential reduction in the form drag of the object moving through the fluid.

On the other hand the upstream travelling waves are attenuating the shedding that comes from the boundary layer leading to re-laminarise downstream.

CHAPTER 5

Numerical codes

Two different numerical codes have been used. The Couette flow, the flat-plate boundary layer and the separating boundary layer case were tackled with the fully-spectral numerical code Simson (Chevalier $et\ al.\ 2007b$). For the leading edge case the spectral element code Nek5000 was used.

5.1. Simson

In Simson, the three-dimensional, time dependent, incompressible Navier-Stokes equations are solved using a spectral method. The algorithm uses Fourier representation in the streamwise and spanwise directions and Chebyshev polynomials in the wall-normal direction, together with a pseudo-spectral treatment of the nonlinear terms. Dealiasing using the 3/2-rule is employed in the wall-parallel (Fourier) directions, whereas a slightly increased resolution is used in the wall-normal direction to reduce aliasing errors. The time is advanced with a four-step low-storage third-order Runge-Kutta method for the nonlinear terms and all the forcing contributions, and a second-order Crank-Nicolson scheme for the linear terms and boundary conditions. For the Couette flow case periodic boundary conditions are used in both wall-parallel direction so the Fourier representation accounts for that implicitly.

For the boundary layer flows, to correctly account for the downstream boundary-layer growth the spatial simulation approach is necessary. This requirement is combined with the periodic streamwise boundary condition by the implementation of a *fringe* region (Nordström *et al.* 1999; Lundbladh *et al.* 1999). In this region, positioned at the downstream end of the computational box occupying approximately 10% of the flow domain, a volume forcing is smoothly raised from zero to force the flow from the outflow to the desired inflow condition. The inflow consists of the laminar Blasius boundary layer and for the case of free-stream turbulence, spatially and temporally varying disturbances are superimposed in the fringe. Otherwise, for initial-value problems a localised perturbations is imposed elsewhere in the domain.

5.2. Nek5000

For the leading edge flow we have adopted the Nek5000 an open source spectral element code developed by Tufo & Fischer (2001); Fischer *et al.* (2008). The governing equations are solved by a weighted residual spectral element method

5. Numerical codes

Patera (1984), which allows multi-domain decomposition while preserving high order accuracy. The optimisation problem for the optimal initial condition is validated against previous results from the flat-plate boundary layer case without the leading edge. The code allows for curved surfaces and supports full MPI parallelisation. It has been proven to scale up to $O(10^5)$ processors.

CHAPTER 6

Conclusions

Numerical simulations of simple shear flows are performed. Optimal disturbances are computed and control is applied with the aim to either delay transition or mitigate separation. For the optimisations performed, the Lagrange multiplier method is used with quadratic objective functions.

The stability of the flat-plate boundary layer flow is studied. Linear optimal initial conditions leading to the largest possible energy amplification at time T and the optimal spatial structure of time-periodic forcing are considered. It is found that two mechanisms dominate the dynamics of this configuration. One corresponding to a combination of the Orr mechanism and the streamwise non-normality of the TS-wave and one to the lift-up effect inherent to spanwise wavelengths of the order of the boundary layer thickness. It is found that due to the long computational box and the relatively high Reynolds number, as well as due to the exponential-type of instability, the TS-wave has more potential for growth. However the streamwise constant structures known as streaks grow much faster and reach their maximum amplitude sooner. Including the leading edge of the plate in the computation, we studied the effect of the geometry to the stability of the boundary layer flow. We found that two-dimensional disturbances originating upstream from the plate are highly inefficient at triggering an unstable wave-packet while three-dimensional disturbances are exploiting the lift up mechanism very efficiently at an early stage and generate strong streamwise streaks inside the boundary layer. With these two projects we demonstrated that it is possible to perform modal and nonmodal linear stability analysis in complicated flow configuration that include geometrical elements by using time-steppers, i.e. by direct numerical simulation of the governing equations.

Non-linear optimisation is used to determine the initial condition of minimum energy leading to laminar/turbulent transition in plane Couette flow; to do this we have resorted to thermodynamics considerations. Using the general evolution criterion we have optimised the route to the statistically steady state the system wants to reach: this is the state of maximum entropy production which coincides with the turbulent state for large enough values of the Reynolds number and of the initial perturbation energy. Nonlinear optimisation is needed to determine this optimal initial condition and the energy threshold below which turbulence cannot ensue. For realistic domain sizes the optimal initial condition is localised in the three spatial directions. The transition path

is characterised by the occurrence of a single bent velocity streak whose oscillations increase rapidly at breakdown. Although computationally expensive, the approach proposed is not limited to simple flows, and the next step is to extend the present results to flows that are inhomogeneous in the streamwise direction.

A linear-based feedback control is applied in order to delay transition, in a flow with highly nonlinear behaviour. The estimator and controller are designed within the Linear Quadratic Regulator (LQR) framework where a parallel base flow is assumed to simplify the computation of the control gains. The results show that the control is able to reduce the energy of the streaks, responsible through their secondary instabilities for the considered bypass-transition scenario and thus delay the whole process. Additionally numerical simulations are performed for a flow case analogous to the experiment performed by Lundell (2007). The control strategy differs while the actuation characteristics are kept as close as possible. Remarkable agreement is achieved in terms of disturbance attenuation. Two main issues became apparent from the two control projects. The actuator technology will probably be decisive being the strongest limiting factor when it comes to implementing these type of control to an experimental setup.

On that front plasma actuators seem to be one possible answer and we show here the need and benefit to model these properly in numerical studies. In this way, numerical simulations can be used effectively to design control experiments. Furthermore there is a need for reducing the cost of the computation of the control signal, since the current formulation demands a full numerical simulation running as fast as the flow is changing in real time. This problem has been studied after the projects presented here were concluded using techniques for model reduction; these investigations have already provided very promising results (Bagheri *et al.* 2009; Semeraro *et al.* 2011).

Open-loop control is applied to a separating boundary layer by means of travelling waves on the wall. The waves are essentially alternating regions of blowing and suction. It is found that the downstream travelling waves can cancel separation while the upstream delay or eliminate the transition to turbulence. The effect of these waves on turbulent separation deserves further investigations.

CHAPTER 7

Summary of papers and division of work between authors

Paper 1

A. Monokrousos, E. Åkervik, L. Brandt & D. S. Henningson, 2010 Global three-dimensional optimal disturbances in the Blasius boundary-layer flow using time-steppers. *J. Fluid Mech.*650, 181-214

In this paper optimal disturbances are computed for the case of the flat-plate boundary-layer flow. Both the optimal initial condition leading to the largest growth at finite times and the optimal time-periodic forcing leading to the largest asymptotic response (pseudospectra) are considered. Lagrange multiplier technique is employed with objective function the kinetic energy of the flow perturbations and constraints the linearised Navier-Stokes equations. Additionally optimal disturbances are computed within a localised framework which for some cases are more relevant to physical situations. In general two different type of disturbances are recovered; the first is relevant to the modal mechanism of a TS-wavepacket ignited by Orr-like structures and convectively amplifying due to the streamwise non-normality; the second is relevant to streamwise elongated disturbances, called streaks, generated by counter-rotating streamwise vortices associated with the strong componentwise transfer of energy due to the lift-up effect. It was found that the first mechanism(s) is more pronounced because of both the long computational domain and the relatively high Reynolds number considered here.

The implementation of the adjoint DNS and the optimal initial condition and forcing power iteration scheme was performed by Antonios Monokrousos (AM) with feedback from Espen Åkervik (EÅ) and Luca Brandt (LB), whereas the Arnoldi iteration scheme using ARPACK method was implemented by EÅ. The computations were for the most part performed by AM except those performed with the Arnoldi method which were done by EÅ. The writing of the paper was done by AM, EÅ and LB with feedback from DH.

Paper 2

A. Monokrousos, L. Brandt, C. Mavriplis & D. S. Henningson, 2011 Optimal disturbances of flow above and upstream a flat plate with an elliptic leading edge. $Technical\ report$

Adjoint-based iterative methods are employed in order to compute optimal disturbances in the case of linear perturbations in a spatially growing boundary layer with an elliptic leading edge. The Lagrangian approach is used where an objective function is chosen and constraints are assigned. Power iterations a are used, both matrix-free methods, where the state is marched forward in time with a normal DNS solver and backward with the adjoint solver until a chosen criterion is fulfilled.

The implementation of the adjoint DNS and the optimal initial condition power iteration scheme was performed by AM with help from Catherine Mavriplis (CM), while the computations were done by AM. The writing of the paper was done by AM and LB with feedback from DH and CM.

Paper 3

A. Monokrousos, A. Bottaro, L. Brandt, A. Di Vita & D. S. Henningson, 2011

Non-equilibrium thermodynamics and the optimal path to turbulence in shear flows. *Phys. Rev. Lett.* 106, 134502

In this paper we use ideas from non-equilibrium thermodynamics to determine the initial condition on the laminar/turbulent boundary closest to the laminar state using nonlinear optimisation for the case of plane Couette flow. Resorting to the general evolution criterion of non-equilibrium systems we optimise the route to the statistically steady turbulent state, *i.e.* the state characterised by the largest entropy production. This is the first time information from the fully turbulent state is included in the optimisation procedure. We demonstrate that the optimal initial condition is localised in space for realistic flow domains.

The implementation of the non-linear optimisation scheme was performed by AM as well as the computations. The writing of the paper was done by AM, Alessandro Bottaro and LB with feedback from DH and Andrea Di Vita.

Paper 4

A. Monokrousos, L. Brandt, P. Schlatter & D. S. Henningson, 2008 DNS and LES of estimation and control of transition in boundary layers subject to free-stream turbulence. *Int. J. Heat and Fluid Flow*, 29, *Issue 3 841-855*

In this paper optimal control is considered where transition to turbulence occurs in a flat-plate boundary-layer flow subjected to high levels of free-stream turbulence. This scenario is denoted bypass transition and is characterised by the non-modal growth of streamwise elongated disturbances called streaks. Linear feedback control is applied in order to reduce the perturbation energy and consequently delay transition. Control is applied by blowing and suction at the wall and it is both based on the full knowledge of the instantaneous velocity field (i.e. full information control) and on the velocity field estimated from wall measurements.

The control is able to delay the growth of the streaks in the region where it is active, which implies a delay of the whole transition process. The flow field can be estimated from wall measurements alone: The structures occurring in the 'real' flow are reproduced correctly in the region where the measurements are taken. Downstream of this region the estimated field gradually diverges from the 'real' flow, revealing the importance of the continuous excitation of the boundary layer by the external free-stream turbulence. Control based on estimation, termed compensator, is therefore less effective than full information control.

The code development and computations relevant to the control part were performed by AM with feedback from LB. The code development and computations relevant to the LES part were performed by Philipp Schlatter (PS). Most of the paper has been written by AM with feedback from LB and DH except the LES part, which was written by PS with feedback from AM, LB and DH.

Paper 5

A. Monokrousos, F. Lundell & L. Brandt, 2010 Feedback control of boundary layer bypass transition: comparison of a numerical study with experiments. *AIAA J.*, 48 (8), 1848-1851

In this paper simulations of optimal feedback control have been performed for a flow configuration similar to that used by and disturbance attenuation as well as transition delay have been obtained. First, an effort is made to match the disturbance behaviour in the experimental flow case and in the simulation. Secondly control is applied in simulations of the matched system aiming at approaching the type of actuation used in the experiments (localised suction). Optimal feedback of the linear system is still the basis for computing the control signal. Remarkable agreement is obtained in terms of disturbance attenuation while the discrepancy in the transition delay can be explained by the fact that in the experiment the controlled region was very narrow in the spanwise direction. Consequently, the controlled region is contaminated by turbulence from the sides.

The experiments were performed by Fredrik Lundell (FL). The code development and computations relevant to the optimal control part were performed by AM with feedback from LB. The writing of the paper was 34

divided accordingly.

Paper 6

A. Monokrousos & L. Brandt, 2011

Control of a separating boundary layer with travelling waves on the wall. $Technical\ report$

Control of a separating boundary layer is applied by means of travelling waves of blowing and suction on the wall. We find that downstream travelling waves, even for very low amplitudes, are able to eliminate the separation and re-attach the boundary layer. Upstream travelling waves for relatively high amplitudes are able to reduce the separation and at the same time re-laminarise the flow.

The implementation of the wall actuation was bone by LB as well as the set-up of the base flow. The computations were done by AM. The writing of the paper was done by AM with feedback from LB.

Acknowledgements

The present thesis is the summary of about four and a half years of research in Prof. Dan S. Henningson's group at KTH Mechanics. This time has been invaluable for my knowledge of fluid mechanics but also enjoyable.

I would like to thank my supervisor Prof. Dan S. Henningson for being an endless source of inspiration. He provided in abundance both guidance and freedom during these years. I would also like to thank to my co-advisor Prof. Luca Brandt who has always demonstrated immense patience but also astonishing brilliance when it comes to solving problems and seemingly magical powers during the paper-writing! Prof. Philipp Schlatter is also acknowledged for his valuable advises on the numerical tools. Many thanks to Espen Åkervik and Prof. Fredrik Lundell for a very rewarding collaboration and to Prof. Alessandro Bottaro for a very pleasant and inspiring stay in Genova. I am grateful to David Tempelmann for several discussions and exchange of ideas. Also many thanks to Paul Fisher and prof. Catherine Mavriplis for their invaluable help with the numerical code Nek5000.

Sharing office with Johan Malm, Qiang Li and Onofrio Semeraro has been always a smooth and pleasant experience. Special thanks to Onofrio who taught me everything there is to know about Italian coffee brewing! Many thanks to the rest of the people in the group: prof. Ardeshir Hanifi, Lars-Uve Schrader, Yohann Duguet, Prof. Stefan Ivanell, Lailai Zhu, Shervin Bagheri, Reza Dadfar, Sasan Sarmast, Azad Noorani, Gaetano Sardina, Joy Klinkenberg, Armin Hosseini, Iman Lashgari, Milos Ilak, Mattias Chevalier, and Ruth Lambert as well as my good friends in the lab Gabriele Bellani, Emma Alenius, It has been great to work among interesting and fun people. Also many thanks to my friends Ruoli, Andreas V., Andreas C., Enrico, Amin, Zeinab and the rest of the research and administration people in the department.

I am grateful to my former advisor prof. Petros J. Ioannou who introduced me to fluid mechanics and also recommended me to come here to Stockholm. I would like to thank Prof. Peter J. Schmid and Prof. Carlo Cossu for several discussions.

I would like to thank my office mates in Genova: Ezio, Anais, Joel, Håkan and Divya for a very pleasant and stimulating four months in Italy.

36 ACKNOWLEDGEMENTS

I am grateful for the valuable comments of prof. Flavio Giannetti, Lailai Zhu and Alica Selmanovic on this manuscript.

The Swedish Research Council (Vetenskapsrådet) is gratefully acknowledged for funding this project. Computer time was provided by SNIC (Swedish National Infrastructure Centre).

Ευχαριστώ τιν οικογένεια μου, Δ ιονύση, Πόπη, Κλειώ και Φιντέλ για την αμερίστη υποστήριξη και υπομονή τους.

Ahmede i Emina, hvala vam na gostoprimstvu i pomoći. Alice, zahvaljujem ti na ljubavi i podršci. Tebi dugujem sve zabavno u protekle tri godine! Nevjerovatna si!

Bibliography

- Bagheri, S., Brandt, L. & Henningson, D. S. 2009 Input-output analysis, model reduction and control of the flat-plate boundary layer. *J. Fluid Mech.* **620**, 263–298.
- Bagheri, S., Hoepffner, J., Schmid, P. J. & Henningson, D. S. 2007 Inputoutput analysis and control design applied to a linear model of spatially developing flows. *Appl. Mech. Rev.* **62**(2) 020803
- Chevalier, M., Hoepffner, J., Åkervik, E. & Henningson, D. S. 2007a Linear feedback control and estimation applied to instabilities in spatially developing boundary layers. *J. Fluid Mech.* 588, 163–187, 167-187.
- Chevalier, M., Schlatter, P., Lundbladh, A. & S., Henningson D. 2007 A pseudo spectral solver for incompressible boundary layer flows. *Technical Report*, *Trita-Mek* 7.
- Cherubini, S., De Palma, P., Robinet, J.-Ch. & Bottaro, A. 2010 Rapid path to transition via nonlinear localized optimal perturbations in a boundary-layer flow. *Phys. Rev. E* 82(6), 066302.
- Cossu, C., Chevalier, M. & Henningson, D. S. 2010 Secondary optimal growth and subcritical transition in the plane poiseuille flow. In *Seventh IUTAM Symposium on Laminar-Turbulent Transition*, , vol. 18, pp. 129–134. Springer, Stockholm
- Di Vita, A. 2010 Maximum or minimum entropy production? how to select a necessary criterion of stability for a dissipative fluid or plasma. *Phys. Rev. E* 81 (4), 041137.
- DIVITA, A & BRUSATI, M 1995 Minimum entropy production principle due to ohmic dissipation in tokamaks and determination of non-inductive current density profiles on jet. *Plasma Physics and Controlled Fusion* 37 (10), 1075.
- FISCHER, P.F., LOTTES, J.W. & KERKEMEIER, S.G. 2008 nek5000 Web page. Http://nek5000.mcs.anl.gov.
- Glansdorff P. & I. Prigogine 1964 On a general evolution criterion in macroscopic physics. *Physica* 30(2), 351-374.
- HOEPFFNER, J., CHEVALIER, M., BEWLEY, T. R. & HENNINGSON, D. S. 2005 State estimation in wall-bounded flow systems. Part 1. Perturbed laminar flows. J. Fluid Mech. ${\bf 534},\,263-294.$
- HÖGBERG, M., BEWLEY, M. & HENNINGSON, D. S. 2003c Linear feedback control and estimation of transition in plane channel flow. J. Fluid Mech. 481, 149–175.

- HÖGBERG, M. & HENNINGSON, D. S. 2002 Linear optimal control applied to instabilities in spatially developing boundary layers. J. Fluid Mech. 470, 151–179.
- Juretic, Davor & Zupanovic, Pasko 2003 Photosynthetic models with maximum entropy production in irreversible charge transfer steps. *Computational Biology and Chemistry* 27 (6), 541 553.
- KAILATH, T. & HASSIBI, A. H. SAYED B. 2000 *Linear Estimation*. New Jersey: Prentice Hall.
- Kreiss, G., Lundbladh, A. & Henningson, D. S. 1994 Bounds for treshold amplitudes in subcritical shear flows. *J. Fluid Mech.* 270, 175–198.
- LEWIS, F. L. & SYRMOS, V. L. 1995 Optimal Control. New York: Wiley-Interscience.
- Lundell, F. 2007 Reactive control of transition induced by free-stream turbulence: an experimental demonstration. *J. Fluid Mech.* **585**, 41–71.
- Malkus, W. V. R. 1956 Outline of a theory of turbulent shear flow. *Journal of Fluid Mechanics* 1 (05), 521–539.
- NORDSTRÖM, J., NORDIN, N. & HENNINGSON, D. S. 1999 The fringe region technique and the Fourier method used in the direct numerical simulation of spatially evolving viscous flows. SIAM J. Sci. Comp. 20, 1365–1393.
- Ozawa, Hisashi, Ohmura, Atsumu, Lorenz, Ralph D. & Pujol, Toni 2003 The second law of thermodynamics and the global climate system: A review of the maximum entropy production principle. *Rev. Geophys.* 41 (4), 1 24.
- Paltridge, Garth W. 1979 Climate and thermodynamic systems of maximum dissipation. *Nature* **279** (6), 630 631.
- Patera A. T. 1984 A Spectral Element Method for Fluid Dynamics: Laminar Flow in a Channel Expansion. *J. Comp. Phys.* **54**, 468–488.
- Pringle, C. C. T. & Kerswell, R. 2011 Using Nonlinear Transient Growth to Construct the Minimal Seed for Shear Flow Turbulence. *Phys. Rev. Lett.* **105**, 154502.
- Rebhan, E. 1990 Maximum entropy production far from equilibrium: The example of strong shock waves. *Phys. Rev. A* 42 (2), 781–788.
- Schmid, P. J. & Henningson, D. S. 2001 Stability and Transition in Shear Flows. New York: Springer.
- Schrader, L.-U., Brandt, L., Mavriplis, C. & Henningson, D. S. 2010 Receptivity to free-stream vorticity of flow past a flat plate with elliptic leading edge. *J. Fluid Mech.* 653 (-1), 245–271.
- Semeraro, O., Bagheri, S., Brandt, L. & Henningson, D.S. 2011 Feedback control of three-dimensional optimal disturbances using reduced-order models. J. Fluid Mech. article in press
- Skogestad, S. & Postlethwaite, I. 2005 Multivariable feedback control, Analysis and Design, 2nd edition. West Sussex: Wiley.
- Trefethen, L. N., Trefethen, A. E., Reddy, S. C. & Driscill, T. A. 1993 Hydrodynamic stability without eigenvalues. *Science* **261**, 578–584.
- Tufo H. M. & Fischer P. F. 1999 Terascale spectral element algorithms and implementations. *Supercomputing, ACM/IEEE 1999 Conference*, Portland, USA.
- Tufo, H.M. & Fischer, P.F 2001 Fast parallel direct solvers for coarse grid problems. *Par. & Dist. Computing* **61(2)**, 151–177.

Part II

Papers

Paper 1

Global optimal disturbances in the Blasius boundary-layer flow using time-steppers

By Antonios Monokrousos, Espen Åkervik, Luca Brandt & Dan S. Henningson

Linné Flow Centre, Department of Mechanics Royal Institute of Technology, SE-100 44 Stockholm, Sweden

Journal of Fluid Mechanics, 650, 181-214, 2010

The global linear stability of the flat-plate boundary-layer flow to threedimensional disturbances is studied by means of an optimisation technique. We consider both the optimal initial condition leading to the largest growth at finite times and the optimal time-periodic forcing leading to the largest asymptotic response. Both optimisation problems are solved using a Lagrange multiplier technique, where the objective function is the kinetic energy of the flow perturbations and the constraints involve the linearised Navier-Stokes equations. The approach proposed here is particularly suited to examine convectively unstable flows, where single global eigenmodes of the system do not capture the downstream growth of the disturbances. In addition, the use of matrix-free methods enables us to extend the present framework to any geometrical configuration. The optimal initial condition for spanwise wavelengths of the order of the boundary layer thickness are finite-length streamwise vortices exploiting the lift-up mechanism to create streaks. For long spanwise wavelengths it is the Orr mechanism combined with the amplification of oblique wave packets that is responsible for the disturbance growth. It is found that the latter mechanism is dominant for the long computational domain and thus for the relatively high Reynolds number considered here. Three-dimensional localised optimal initial conditions are also computed and the corresponding wave-packets examined. For short optimisation times, the optimal disturbances consist of streaky structures propagating and elongating in the downstream direction without significant spreading in the lateral direction. For long optimisation times, we find the optimal disturbances with the largest energy amplification. These are wave-packets of TS-waves with low streamwise propagation speed and faster spreading in the spanwise direction. The pseudo-spectrum of the system for real frequencies is also computed with matrix-free methods. The spatial structure of the optimal forcing is similar to that of the optimal initial condition, and the largest response to forcing is also associated with the Orr/oblique wave mechanism, however less so than in the case of the optimal initial condition. The lift-up mechanism is most efficient at zero frequency and degrades slowly

for increasing frequencies. The response to localised upstream forcing is also discussed.

1. Introduction

The flat-plate boundary layer is a classic example of convectively unstable flows; these behave as broadband amplifiers of incoming disturbances. As a consequence, a global stability analysis based on the asymptotic behaviour of single eigenmodes of the system will not capture the relevant dynamics. From this global perspective all the eigenmodes are damped, and one has to resort to an input/output formulation in order to obtain the initial conditions yielding the largest possible disturbance growth at any given time and the optimal harmonic forcing. To do this, an optimisation procedure is adopted. The aim of this work is to investigate the global stability of the flow over a flat plate subject to external perturbations and forcing and to examine the relative importance of the different instability mechanisms at work, see discussion below. The approach adopted here can be extended to any complex flow provided a numerical solver for the direct and adjoint linearised Navier-Stokes equations is available.

Recently, the global stability of the spatially-evolving Blasius flow subject to two-dimensional disturbances has been studied within an optimisation framework by projecting the system onto a low-dimensional subspace consisting of damped Tollmien-Schlichting (TS) eigenmodes (Ehrenstein & Gallaire 2005). These results were extended by Åkervik et al. (2008), who found that by not restricting the spanned space to include only TS modes, the optimally growing structures could exploit both the Orr and TS wave packet mechanism and yield a substantially higher energy growth. The Orr mechanism (Orr 1907) was studied in the context of parallel shear flows using the Orr-Sommerfeld/Squire equations by Butler & Farrell (1992), who termed it the Reynolds stress mechanism. This instability extracts energy from the mean shear by transporting momentum down the mean momentum gradient through the action of the perturbation Reynolds stress. In other words disturbances that are tilted against the shear can borrow momentum from the mean flow while rotating with the shear until they are aligned with it. This mechanism is also referred to as wall-normal non-normality.

From the local point of view the TS waves appear as unstable eigenvalues of the Orr–Sommerfeld equation. In the global framework however the global eigenmodes belonging to the TS branch are damped (Ehrenstein & Gallaire 2005), and the evolution of TS waves consist of cooperating global modes that produce wave packets. Considering the model problem provided by the Ginzburg-Landau equation with spatially varying coefficients, Cossu & Chomaz (1997) demonstrated that the non-normality of the streamwise eigenmodes resulting from the local convective instabilities leads to substantial transient growth. This non-normality is revealed by the streamwise separation of

the direct and adjoint global modes induced by the basic flow advection; it is therefore also termed streamwise non-normality (Chomaz 2005).

It is now well established that when incoming disturbances exceed a certain amplitude threshold the flat-plate boundary layer is likely to undergo transition due to three-dimensional instabilities arising via the lift-up effect (Ellingsen & Palm 1975; Landahl 1980). This transient growth scenario, where streamwise vortices induce streamwise streaks by the transport of the streamwise momentum of the mean flow, was studied for a variety of shear flows in the locally parallel assumption (c.f. Butler & Farrell 1992; Reddy & Henningson 1993; Trefethen et al. 1993). The extension to the non-parallel flat plate boundary layer was performed at the same time by Andersson et al. (1999) and Luchini (2000) by considering the steady linear boundary-layer equations parabolic in the streamwise direction. In these investigations the optimal upstream disturbances are located at the plate leading edge and a Reynolds number independent growth was found for the evolution of streaks at large downstream distances. Levin & Henningson (2003) examined variations of the position at which disturbances are introduced and found the optimal location to be downstream of the leading edge. In this study, also low-frequency perturbations were considered, still within the boundary layer approximation. In the global framework an interpretation of the lift-up mechanism is presented e.g. in Marquet et al. (2008): Whereas the TS mechanism is governed by a transport of the disturbances by the base flow, the lift-up mechanism is governed by a transport of the base flow by the disturbances. Inherent to the lift up mechanism is the component-wise transfer of momentum from the two cross-stream to the streamwise velocity component (component-wise non-normality).

The standard way of solving the optimisation problems involved in the determination of optimal initial condition (or forcing) is to directly calculate the matrix norm of the discretised evolution operator (or the pseudo-spectrum of the resolvent) of the system. In the local approach, where the evolution is governed by the Orr-Sommerfeld/Squire equations it is clearly feasible to directly evaluate the matrix exponential or to invert the relevant matrix. In the global approach it is in general difficult and in some cases impossible to build the discretised system matrix. One possible remedy is to compute a set of global eigenmodes with iterative methods and project the flow system onto the subspace spanned by these eigenvectors. The optimisation is then performed in a low dimensional model of the flow: results for the flat-plate boundary layer can be found in Ehrenstein & Gallaire (2005); Åkervik et al. (2008) while two-dimensional and three-dimensional studies on separated flows were performed e.g. by Åkervik, Hopffner, Ehrenstein & Henningson (2007); Gallaire, Marquillie & Ehrenstein (2007); Ehrenstein & Gallaire (2008); Alizard, Cherubini & Robinet (2009)

However, the direct *matrix-free* approach followed here is preferable, if not indispensable, for more complicated flows. This amounts to solving eigenvalue problems using only Direct Numerical Simulations of the evolution operators.

This approach is commonly referred to as a time-stepper technique (Tuckerman & Barkley 2000); one of its first applications was to the linear stability analysis of a spherical Couette flow (Marcus & Tuckerman 1987a,b; Mamun & Tuckerman 1995). The time-stepper technique was then generalised to optimal growth calculations by introducing the adjoint evolution operator and solving the eigenvalue problem of the composite operator (Blackburn $et\ al.$ 2008; Barkley $et\ al.$ 2008) for backward facing step flow; it was subsequently applied to separation bubbles (Marquet $et\ al.$ 2008, 2009) and to the flat-plate boundary-layer flow subject to two-dimensional disturbances (Bagheri $et\ al.$ 2009a).

Thus, in this paper we study the stability of the flat-plate boundary-layer flow subject to three-dimensional disturbances from a global perspective using a time-stepper technique. The base flow has two inhomogeneous directions, namely the wall-normal and streamwise, thereby allowing a decoupling of Fourier modes in the spanwise direction only. Both optimal initial condition and optimal forcing are therefore first considered for a range of spanwise wavenumbers, seeking to find the spanwise scale of the most amplified disturbances. In the case of optimal initial conditions, we optimise over a range of final times, while time-periodic optimal forcing are computed for a range of frequencies. In addition, we compute for the first time optimal initial conditions localised in space. The evolution of the resulting wave-packet is analysed in terms of flow structures and propagation speed.

Whereas the computation of optimal initial condition is known in the global time-stepper context (see references above), the formulation of the optimal forcing problem in this framework is novel. This enables us to compute the pseudo-spectrum of the non-normal governing operator with a matrix-free method. The latter type of analysis can have direct implications for flow control as well: The optimisation procedure allows us to determine the location and frequency of the forcing to which the flow under consideration is most sensitive.

The paper is organised as follows. Section 2 is devoted to the description of the base flow and the governing linearised equations. Section 3 and 4 describe the Lagrange approach to solving the optimisation problems defined by the optimal initial conditions and optimal forcing, respectively. The main results are presented in section 5; the paper ends with a summary of the main conclusions.

2. Basic steady flow, governing equations and adjoint system

We investigate the stability of the classical spatially-evolving two-dimensional flat-plate boundary-layer flow subject to three-dimensional disturbances. The computational domain starts at a distance x from the leading edge defined by the Reynolds number $Re_x = U_{\infty}x/\nu = 3.38 \cdot 10^5$ or $Re_{\delta^*} = 1.72\sqrt{Re_x} = U_{\infty}\delta_0^*/\nu = 10^3$. Here U_{∞} is the uniform free stream velocity, δ^* is the local displacement thickness and ν is the kinematic viscosity. We denote

the displacement thickness at the inflow position δ_0^* . All variables are nondimensionalised by U_{∞} and δ_0^* . We solve the linearised Navier–Stokes equations using a spectral DNS code described in Chevalier et al. (2007) on a domain $\Omega = [0, L_x] \times [0, L_y] \times [0, L_z]$. The non-dimensional height of the computational box is $L_y = 30$ and the length is $L_x = 1000$, while the spanwise width is $L_z = 502.6$ for the case of localised initial conditions or defined in each simulation by the Fourier mode under investigation. In the wall-normal direction, y, a Chebyshev-tau technique with $n_y = 101$ polynomials is used along with homogeneous Dirichlet conditions at the wall and the free-stream boundary. In the streamwise and spanwise directions we assume periodic behaviour, hence allowing for a Fourier transformation of all variables. For the simulations presented here, the continuous variables are approximated by $n_x = 768$ and $n_z = 128$ Fourier modes in the streamwise and spanwise direction respectively, whereas we solve for each wave-number separately in the spanwise direction when considering spanwise periodic disturbances, a decoupling justified by the spanwise homogeneity of the base flow. Since the boundary layer flow is spatially evolving a fringe region technique is used to ensure that the flow is forced back to the laminar inflow profile at x=0 (Nordström et al. 1999). The fringe forcing quenches the incoming perturbations and is active at the downstream end of the computational domain, $x \in [800, 1000]$, so that x = 800 can be considered as the effective outflow location, corresponding to $Re_x = 1.138 \cdot 10^6$. The steady state used in the linearisation is obtained by marching the nonlinear Navier-Stokes equations in time until the norm of the time derivative of the solution is numerically zero. Thus the two-dimensional steady state with velocities $\mathbf{U} = (U(x,y), V(x,y), 0)^T$ and pressure $\Pi(x,y)$ differs slightly from the well-known Blasius similarity solution.

2.1. The linearised Navier-Stokes equations

We investigate the growth of small amplitude three-dimensional disturbances on a two-dimensional base flow. The stability characteristics of the base flow **U** to small perturbations $\mathbf{u} = (u(\mathbf{x},t),v(\mathbf{x},t),w(\mathbf{x},t))^T$ are determined by the linearized Navier–Stokes equations

$$\partial_t \mathbf{u} + (\mathbf{U} \cdot \nabla) \mathbf{u} + (\mathbf{u} \cdot \nabla) \mathbf{U} = -\nabla \pi + Re^{-1} \Delta \mathbf{u} + \mathbf{g},$$
 (1)

$$\nabla \cdot \mathbf{u} = 0, \tag{2}$$

subject to initial condition $\mathbf{u}(\mathbf{x}, t = 0) = \mathbf{u}_0(\mathbf{x})$. Note that we have included a divergence-free forcing term $\mathbf{g} = \mathbf{g}(\mathbf{x}, t)$ to enable us to also study the response to forcing as well as to initial condition. In the expression above, the fringe forcing term is omitted for simplicity (see Bagheri *et al.* 2009*b*).

When performing systematic analysis of the linearized Navier–Stokes equations we are interested in the initial condition $\mathbf{u}(0)$ and in the features of the flow states $\mathbf{u}(t)$ at times t>0. We will also consider the spatial structure of the time-periodic forcing \mathbf{g} that creates the largest response at large times, that is when all transients effects have died out. Our analysis will therefore

consider flow states induced by forcing or initial conditions, where a flow state is defined by the three-dimensional velocity vector field throughout the computational domain Ω at time t. To this end, it is preferable to re-write the equations in a more compact form. In order to do so we define the velocities as our state variable, *i.e.* $\mathbf{u} = (u, v, w)^T$. Following Kreiss *et al.* (1994) the pressure can be formally written in terms of the velocity field $\pi = \mathcal{K}\mathbf{u}$ solution of equation 3

$$\Delta \pi = -\nabla \cdot ((\mathbf{U} \cdot \nabla)\mathbf{u} + (\mathbf{u} \cdot \nabla)\mathbf{U}). \tag{3}$$

The resulting state space formulation of equation (1) reads

$$(\partial_t - \mathcal{A})\mathbf{u} - \mathbf{g} = 0, \quad \mathbf{u}(0) = \mathbf{u}_0, \tag{4}$$

Alternatively \mathcal{A} may also be defined using semi-group theory, where it is referred to as the infinitesimal generator of the evolution operator $\mathcal{T}(t)$. \mathcal{T} defined as the operator that maps a solution at time t_0 to time $t_0 + t$.

$$\mathbf{u}(t+t_0) = \mathcal{T}(t)\mathbf{u}(t_0). \tag{5}$$

For further explanation we refer to Trefethen & Embree (2005). In what follows we use the evolution operator \mathcal{T} to study both the response to initial condition and the regime response to forcing, *i.e.* we look at the long term periodic response. Indeed for practical numerical calculations the variables are often discretised, so that the governing operator becomes a matrix of size $n \times n$, with $n = 3n_x n_y n_z$ for general three-dimensional disturbances. When considering spanwise periodic disturbances we can focus on one wave number at a time and the dimension of the system matrix is reduced to $n = 3n_x n_y$. However, even in this case the evaluation of the discretised evolution operator $\mathcal{T} = \exp(\mathcal{A}t)$ is computationally not feasible. The complete stability analysis, including the optimisation, can be efficiently performed by marching in time the linearised Navier–Stokes equations using a numerical code. This so called time stepper technique has indeed become increasingly popular in stability analysis (Tuckerman & Barkley 2000).

2.2. Choice of norm and the adjoint equations

In order to measure the departure from the base flow we use the kinetic energy of the perturbations

$$\|\mathbf{u}(t)\|^2 = (\mathbf{u}(t), \mathbf{u}(t)) = \int_{\Omega} \mathbf{u}^H \mathbf{u} \, d\Omega.$$
 (6)

Since transition in shear flows is initiated by secondary instabilities induced by local gradients in the flow, one could alternatively use an infinity norm or maximise directly the shear or vorticity. Using the above inner product we may define the action of the adjoint evolution operator as

$$(\mathbf{v}, \exp(\mathcal{A}t)\mathbf{u}) = (\exp(\mathcal{A}^{\dagger}t)\mathbf{v}, \mathbf{u}), \tag{7}$$

where \mathcal{A}^{\dagger} is defined by the initial value problem

$$-\partial_t \mathbf{v} = \mathcal{A}^{\dagger} \mathbf{v} = (\mathbf{U} \cdot \nabla) \mathbf{v} - (\nabla \mathbf{U})^T \mathbf{v} + Re^{-1} \Delta \mathbf{v} + \nabla \mathcal{Z} \mathbf{v}, \quad \mathbf{v}(T) = \mathbf{v}_T.$$
(8)

The adjoint system (8) is derived using the inner product in time space domain $\Sigma = [0, T] \times \Omega$. The operator \mathcal{Z} is the counterpart of the operator \mathcal{K} for the adjoint pressure: $\sigma = \mathcal{Z}\mathbf{v}$. This initial value problem has stable integration direction backwards in time so we may define the adjoint solution at time T - t for the forward running time t as

$$\mathbf{v}(T-t) = \exp(\mathcal{A}^{\dagger}t)\mathbf{v}_{T}, \quad t \in [0, T]. \tag{9}$$

It is important to note that the addition of the forcing term \mathbf{g} in (1) has no effect on the derivation of the adjoint equations. In particular, the fringe forcing term is self-adjoint since proportional to the velocity \mathbf{u} .

3. Optimal initial conditions

In this section, we derive the system whose solution yields initial conditions which optimally excite flow disturbances. When seeking the optimal initial condition we assume that the forcing term \mathbf{g} in (4) is zero. We wish to determine the unit norm initial condition $\mathbf{u}(0)$ yielding the maximum possible energy $(\mathbf{u}(T), \mathbf{u}(T))$ at a prescribed time T. A common way of obtaining the optimal initial condition is to recognise that the condition

$$G(t) = \max_{\|\mathbf{u}(0)\| \neq 0} \frac{\|\mathbf{u}(T)\|^2}{\|\mathbf{u}(0)\|^2} = \max_{\|\mathbf{u}(0)\| \neq 0} \frac{(\mathbf{u}(0), \exp(\mathcal{A}^{\dagger}T) \exp(\mathcal{A}T)\mathbf{u}(0))}{(\mathbf{u}(0), \mathbf{u}(0))}$$
(10)

defines the Rayleigh quotient of the composite operator $\exp(A^{\dagger}T)\exp(AT)$. The optimisation problem to be solved is hence the eigenvalue problem

$$\gamma \mathbf{u}(0) = \exp(\mathcal{A}^{\dagger} T) \exp(\mathcal{A} T) \mathbf{u}(0). \tag{11}$$

In the case of a large system matrix, as in fluid-flow systems, this eigenvalue problem can be efficiently solved by matrix-free methods using a time-stepper (DNS) and performing power-iterations or the more advanced Arnoldi method (c.f. Nayar & Ortega 1993; Lehoucq *et al.* 1997); both methods only need a random initial guess for $\mathbf{u}(0)$ and a numerical solver to determine the action of $\exp(\mathcal{A}T)$ and $\exp(\mathcal{A}^{\dagger}T)$ (Barkley *et al.* 2008).

One alternative approach relies on the Lagrange multiplier technique which we believe allows for more flexibility in defining different objective functions as well as in enforcing additional constrains. Here, we show how this approach is used to compute the unit norm initial condition $\mathbf{u}(0)$ non-zero only within a fixed region in space, $\Lambda \subset \Omega$, i.e. the localised optimal initial condition. The objective is still maximising the kinetic energy at final time T

$$\mathcal{J} = (\mathbf{u}(T), \mathbf{u}(T)). \tag{12}$$

The following constraints need to be enforced: the flow needs to satisfy the governing linearized Navier–Stokes equations (4) (without forcing) and the initial condition must have unit norm and exist only inside Λ . Additionally the optimal perturbation must be divergence-free condition. Hence the Lagrange

function reads

$$\mathcal{L}(\mathbf{u}, \mathbf{v}, \gamma) = (\mathbf{u}(T), \mathbf{u}(T)) - \int_0^T (\mathbf{v}, (\partial_t - \mathcal{A}) \mathbf{u}) d\tau$$
$$-\gamma ((\mathbf{u}(0), \mathbf{u}(0))_{\Lambda} - 1) - (\psi, \nabla \cdot \mathbf{u}(0))_{\Lambda}$$
(13)

where \mathbf{v}, γ and ψ are the Lagrange multipliers. The inner product defined by $(\cdot, \cdot)_{\Lambda}$ corresponds to an integral in Λ . Note that the normalisation condition selects a unique solution of the eigenvalue problem and thus enable the numerical procedure to converge. We need to determine $\mathbf{u}, \mathbf{u}(0), \mathbf{u}(T), \mathbf{v}$ and γ such that \mathcal{L} is stationary, necessary condition for first order optimality. This can be achieved by requiring that the variation of \mathcal{L} is zero,

$$\delta \mathcal{L} = \left(\frac{\partial \mathcal{L}}{\partial \mathbf{u}}, \delta \mathbf{u}\right) + \left(\frac{\partial \mathcal{L}}{\partial \mathbf{v}}, \delta \mathbf{v}\right) + \left(\frac{\partial \mathcal{L}}{\partial \gamma}\right) \delta \gamma + \left(\frac{\partial \mathcal{L}}{\partial \psi}\right) \delta \psi = 0.$$
 (14)

This is only fulfilled when all terms are zero simultaneously. The variation with respect to the costate variable (or adjoint state variable) yields directly the state equation

$$(\partial_t - \mathcal{A})\mathbf{u} = 0, \tag{15}$$

and similarly the variation with respect to multiplier γ yields a normalisation criterion

$$\left(\frac{\partial \mathcal{L}}{\partial \gamma}, \delta \gamma\right) \Rightarrow (\mathbf{u}(0), \mathbf{u}(0))_{\Lambda} = 1. \tag{16}$$

In order to take the variations with respect to the other variables we perform integration by parts on the second term of \mathcal{L} in (13) to obtain

$$\mathcal{L} = (\mathbf{u}(T), \mathbf{u}(T)) - \int_0^T (\mathbf{u}, (-\partial_t - \mathcal{A}^{\dagger}) \mathbf{v}) d\tau - (\mathbf{v}(T), \mathbf{u}(T)) + (\mathbf{v}(0), \mathbf{u}(0)) - \gamma ((\mathbf{u}(0), \mathbf{u}(0))_{\Lambda} - 1) - (\psi, \nabla \cdot \mathbf{u}(0))_{\Lambda}.$$
(17)

The variation of this expression with respect to the state variable \mathbf{u} yields an equation for the adjoint variable as well as two optimality conditions

$$\left(\frac{\partial \mathcal{L}}{\partial \mathbf{u}}, \delta \mathbf{u}\right) \Rightarrow -\int_{0}^{T} (\delta \mathbf{u}, (-\partial_{t} - \mathcal{A}^{\dagger}) \mathbf{v}) + (\delta \mathbf{u}, \mathbf{v} - \gamma \mathbf{u})|_{t=0} + (\delta \mathbf{u}, \mathbf{u} - \mathbf{v})|_{t=T} = 0.$$
(18)

The simplest choice to satisfy this condition is each of this terms being separately zero so finally we get

$$(-\partial_t - \mathcal{A}^{\dagger})\mathbf{v} = 0, \qquad (19)$$

and

$$\mathbf{u}(0) = \gamma^{-1}\mathbf{v}(0),$$

$$\mathbf{v}(T) = \mathbf{u}(T).$$
 (20)

Variations with respect to the initial velocity field give the following condition

$$(\delta \mathbf{u}(0), \mathbf{v}(0)) - \gamma (\delta \mathbf{u}(0), \mathbf{u}(0))_{\Lambda} - (\delta \mathbf{u}(0), \nabla \psi)_{\Lambda} = 0.$$
 (21)

The expression above can be re-written in integral form

$$\int_{\Omega - \Lambda} (\delta \mathbf{u}(0)^T \mathbf{v}(0)) + \int_{\Lambda} \delta \mathbf{u}(0)^T (\mathbf{v}(0) - \gamma \mathbf{u}(0) - \nabla \psi) = 0.$$
 (22)

The first integral is zero for $\delta \mathbf{u}(0) = 0$, which implies that the initial condition is not updated outside Λ . Therefore the new guess for the localised initial condition $\mathbf{u}(0)$ is

$$\mathbf{u}(0) = \gamma^{-1}(\mathbf{v}(0) - \nabla \psi)|_{\Lambda}. \tag{23}$$

In the above, the scalar field ψ is obtained by combining (23) with

$$\frac{\partial \mathcal{L}}{\partial \psi} = \nabla \cdot \mathbf{u}(0) = 0. \tag{24}$$

This gives a projection to a divergence free space where the pressure-like scalar field is solution of a Poisson equation. It can be proven that this is a unique projection. In our numerical implementation the projection is actually performed by transforming in the velocity-vorticity formulation adopted for the computations (Chevalier et al. 2007).

The procedure described above solves an eigenvalue problem similar to (11) with the addition of an operator \mathcal{PC} that localises in space and projects to divergence-free space

$$\gamma \mathbf{u}(0) = \mathcal{PC} \exp(\mathcal{A}^{\dagger} T) \exp(\mathcal{A} T) \mathbf{u}(0). \tag{25}$$

The optimality system to be solved is hence composed of equations (15),(16),(19) and (20) along with the projection to divergence-free space (23). From (16) and the first relation in (20), it can readily be seen that $\gamma = (\mathbf{v}(0), \mathbf{v}(0))$. The remaining equations are solved iteratively as follows. Starting with an initial guess $\mathbf{u}(0)^n$:

- (i) we integrate (15) forward in time and obtain $\mathbf{u}(T)$;
- (ii) $\mathbf{v}(T) = \mathbf{u}(T)$ is used as an initial condition at t = T for the adjoint system
- (19), which integrated backward in time gives $\mathbf{v}(0)$;
- (iii) we determine a new initial guess by localising $\mathbf{v}(0)$, casting it to divergencefree space and normalising it to unit norm, $\mathbf{u}(0) = \gamma^{-1}(\mathbf{v}(0) - \nabla \psi)|_{\Lambda}$;
- (iv) if $|\mathbf{u}(0)^{n+1} \mathbf{u}(0)^n|$ is larger than a given tolerance, the procedure is repeated.

Before convergence is obtained $\mathbf{u}(0)$ and $\mathbf{v}(0)$ are not aligned. At convergence, $\mathbf{u}(0)$ is an eigenfunction of (25). The iteration scheme above can be seen as a power iteration scheme finding the largest eigenvalue of the problem (25). Since the composite operator is symmetric its eigenvalues are real and its eigenvectors form an orthogonal basis. The eigenvalues of the system rank the set of optimal initial conditions according to the output energy at time T. If several optimals are sought, e.g. to build a reduced order model of the flow, the sequence of $\mathbf{u}(0)^n$ produced in the iteration can be used to build a Krylov subspace suitable for the Arnoldi method.

4. Optimal forcing

This section will focus on the regime response of the system to time-periodic forcing. Thus we assume zero initial conditions, $\mathbf{u}(0) = 0$, and periodic behaviour of the forcing function, *i.e.*

$$\mathbf{g} = \Re \left(\mathbf{f}(\mathbf{x}) \exp(i\omega t) \right), \quad \mathbf{f} \in \mathbb{C}, \quad \omega \in \mathbb{R},$$
 (26)

where ${\bf f}$ defines the spatial structure of the forcing, ω is its circular frequency and \Re denotes the real part. With these assumptions, the governing equations become

$$(\partial_t - \mathcal{A})\mathbf{u} - \Re\left(\mathbf{f}\exp(i\omega t)\right) = 0, \quad \mathbf{u}(0) = 0. \tag{27}$$

In this case, we wish to determine the spatial structure and relative strength of the components of the forcing \mathbf{f} that maximise the response of the flow at the frequency ω in the limit of large times, *i.e.* the regime response of the flow. The measure of the optimum is also here based on the energy norm. Note that for this method to converge and for the regime response to be observed, the operator \mathcal{A} must be globally stable. In the spatial framework this requirement is always satisfied.

In order to formulate the optimisation problem it is convenient to work in the frequency domain, thereby removing the time dependence. By assuming time periodic behaviour, \mathbf{u} is replaced by the complex field $\tilde{\mathbf{u}}$ so that

$$\mathbf{u} = \Re\left(\tilde{\mathbf{u}}\exp(i\omega t)\right). \tag{28}$$

The resulting governing equations can then be written

$$(i\omega \mathcal{I} - \mathcal{A})\tilde{\mathbf{u}} - \mathbf{f} = 0. \tag{29}$$

Note that the operator \mathcal{A} , containing only spatial derivatives, remains unchanged. The Lagrange function for the present optimisation problem is similar in structure to that used to determine the optimal initial condition and is formulated as follows

$$\mathcal{L}(\tilde{\mathbf{u}}, \tilde{\mathbf{v}}, \gamma, \mathbf{f}) = (\tilde{\mathbf{u}}, \tilde{\mathbf{u}}) - (\tilde{\mathbf{v}}, (i\omega\mathcal{I} - \mathcal{A})\tilde{\mathbf{u}} - \mathbf{f}) - \gamma((\mathbf{f}, \mathbf{f}) - 1). \tag{30}$$

The objective function is the disturbance kinetic energy of the regime response, $(\tilde{\mathbf{u}}, \tilde{\mathbf{u}})$ where the complex variable $\tilde{\mathbf{u}}$ requires the use of the Hermitian transpose. The additional constrains require the flow to be solution of the linearised forced Navier–Stokes equations and introduce a normalisation condition for the forcing amplitude. Since the state variable $\tilde{\mathbf{u}}$ is a solution of the time independent system (29), the inner product used in the definition of the adjoint involves only spatial integrals. The time behaviour of the costate or adjoint variable is indeed assumed to be also periodic $\mathbf{v} = \Re(\tilde{\mathbf{v}} \exp(i\omega t))$. Thus in the derivation of the adjoint the time derivative is replaced by the term $i\omega \tilde{\mathbf{u}}$, with adjoint $-i\omega \tilde{\mathbf{v}}$. As for the computation of the optimal initial condition, we take variations with respect to $\tilde{\mathbf{u}}$, $\tilde{\mathbf{v}}$, $\tilde{\mathbf{f}}$ and γ

$$\delta \mathcal{L} = \left(\frac{\partial \mathcal{L}}{\partial \tilde{\mathbf{u}}}, \delta \tilde{\mathbf{u}}\right) + \left(\frac{\partial \mathcal{L}}{\partial \tilde{\mathbf{v}}}, \delta \tilde{\mathbf{v}}\right) + \left(\frac{\partial \mathcal{L}}{\partial \mathbf{f}}, \delta \mathbf{f}\right) + \left(\frac{\partial \mathcal{L}}{\partial \gamma}\right) \delta \gamma. \tag{31}$$

The first order optimality condition requires all of the terms to be simultaneously zero. By taking variations with respect to the costate variable (or adjoint variable) we again obtain the state equation (29). Similarly the variation with respect to the multiplier γ yields the normalisation criterion $(\mathbf{f}, \mathbf{f}) - 1 = 0$. In order to take the variations with respect to the other variables we perform integration by parts on the second term of \mathcal{L} in (30) to obtain

$$\mathcal{L}(\tilde{\mathbf{u}}, \tilde{\mathbf{v}}, \gamma, \mathbf{f}) = (\tilde{\mathbf{u}}, \tilde{\mathbf{u}}) - (\tilde{\mathbf{u}}, (-i\omega\mathcal{I} - \mathcal{A}^{\dagger})\tilde{\mathbf{v}}) + (\mathbf{f}, \tilde{\mathbf{v}}) - \gamma((\mathbf{f}, \mathbf{f}) - 1). \tag{32}$$

No initial-final condition terms appear during this integration by parts since here the inner product is only in space (in contrast to the optimal initial condition). Variations with respect to the state variable $\tilde{\mathbf{u}}$ and to the forcing function f yield

$$\left(\frac{\partial \mathcal{L}}{\partial \tilde{\mathbf{u}}}\right) \Rightarrow \tilde{\mathbf{u}} - (-i\omega \mathcal{I} - \mathcal{A}^{\dagger})\tilde{\mathbf{v}} = 0,$$

$$\left(\frac{\partial \mathcal{L}}{\partial \mathbf{f}}\right) \Rightarrow \mathbf{f} = \gamma^{-1}\tilde{\mathbf{v}}.$$
(33)

$$\left(\frac{\partial \mathcal{L}}{\partial \mathbf{f}}\right) \Rightarrow \mathbf{f} = \gamma^{-1}\tilde{\mathbf{v}}.\tag{34}$$

Equations (29) and (33) are the two equations we have to solve with the timestepper. The normalisation condition $(\mathbf{f}, \mathbf{f}) = 1$ and equation (34) provide the optimality condition that is used to calculate the new forcing field after each iteration of the optimisation loop. A similar approach is used to compute the localised optimal forcing. The corresponding results are presented in section 5.2.2.

Next, we show the equivalence between the Lagrange multiplier technique and the corresponding standard matrix method when the resolvent norm is considered. The formal solution of equation (27) can be written as

$$\tilde{\mathbf{u}} = (i\omega I - \mathcal{A})^{-1}\mathbf{f}. \tag{35}$$

The corresponding solution for the adjoint system

$$\tilde{\mathbf{v}} = (-i\omega I - \mathcal{A}^{\dagger})^{-1}\tilde{\mathbf{u}}. \tag{36}$$

Combining the two equations above and using (34)

$$\mathbf{f} = \frac{1}{\gamma} (-i\omega I - \mathcal{A}^{\dagger})^{-1} (i\omega I - \mathcal{A})^{-1} \mathbf{f}.$$
 (37)

This is a new eigenvalue problem defining the spatial structure of the optimal forcing at frequency ω that is solved iteratively; the largest eigenvalue corresponds to the square of the resolvent norm

$$\gamma = \|(i\omega I - A)^{-1}\|^2.$$
 (38)

Note that the actual implementation uses a slightly different formulation, since the available time-stepper does not solve directly (29) and (33). In practice, the governing equations are integrated in time long enough that the transient behaviour related to the system operator A has died out. The regime response for the direct and adjoint system is extracted by performing a Fourier transform of the velocity field during one period of the forcing.

The steps of the optimisation algorithm therefore are:

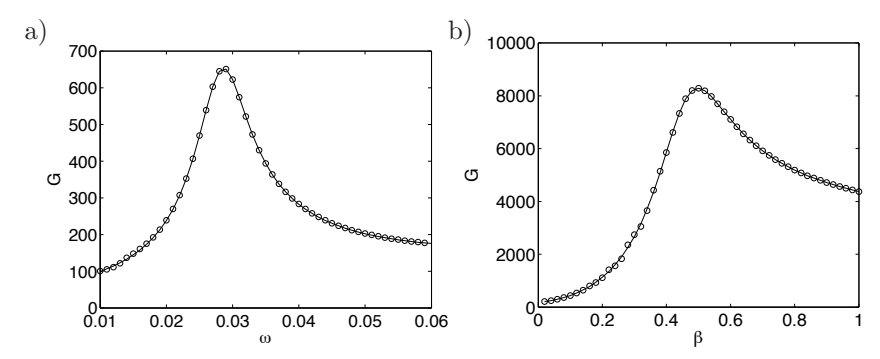


FIGURE 1. Comparison of results from the adjoint iteration scheme (shown as circles) and direct solution in terms of SVD of the OSS resolvent (shown as solid lines) for optimal forcing to the parallel Blasius flow at Re=1000. a) Zero spanwise wave-number β for different frequencies ω and for streamwise wave-number $\alpha=0.1$. b) Streamwise wave-number $\alpha=0.1$ for different spanwise wave-numbers β subject to forcing with frequency $\omega=0.05$. Both plots show excellent agreement between the two methods. Note that in order to obtain a regime response in the parallel case the wave-numbers are chosen so that the system operator is stable.

- (i) Integrate (27) forward in time and obtain the Fourier transform response $\tilde{\mathbf{u}}$ at the frequency of the forcing.
- (ii) $\tilde{\mathbf{u}}$ is used as a forcing for the adjoint system which in time domain is written

$$(-\partial_t - \mathcal{A}^{\dagger})\mathbf{v} - \Re\left(\tilde{\mathbf{u}}\exp(i\omega t)\right) = 0.$$
(39)

- (iii) A new forcing function is determined by normalising $\mathbf{f}^{n+1} = \tilde{\mathbf{v}}/\gamma$.
- (iv) If $|\mathbf{f}^{n+1} \mathbf{f}^n|$ is larger than a given tolerance, the procedure is repeated. Additionally, we study the case of localised optimal forcing. The relevant formulation is similar to that presented for spatially localised perturbations in section 3.

A validation of the method is presented in figure 1, where the results from the present adjoint-based iteration procedure are compared to those obtained by the standard method of performing a singular value decomposition (SVD) of the resolvent of the Orr–Sommerfeld and Squire equations for the parallel Blasius flow (c.f. Schmid & Henningson 2001). In figure 1a) the response to forcing with spanwise wave-number $\beta=0$ is shown for different frequencies, whereas the response to steady forcing with streamwise wave-number α is shown in figure 1b). In the latter case, variations of the spanwise wave-numbers are considered. In both cases, excellent agreement between the two methods is observed.

5. Results

The flat plate boundary layer flow is globally stable, *i.e.* there are no eigenvalues of \mathcal{A} located in the unstable half plane. Hence we do not expect to observe the evolution of single eigenmodes. In Åkervik et al. (2008) the non-modal stability of this flow subject to two-dimensional disturbances was studied by considering optimal superposition of eigenmodes. These authors found that the optimal initial condition exploits the well known Orr mechanism to efficiently trigger the propagating Tollmien-Schlichting wave packet. In Bagheri et al. (2009a), the stability of the same flow was studied using forward and adjoint iteration scheme together with the Arnoldi method to reproduce the same mechanism. By allowing for three-dimensional disturbances, it is expected that in addition to the instability mechanisms mentioned above (convective Tollmien-Schlichting instability and the Reynolds stress mechanism of Orr) the lift-up mechanism will be relevant in the system.

This has been well understood both using the Orr–Sommerfeld/Squire equations (Butler & Farrell 1992; Reddy & Henningson 1993) in the parallel temporal framework and using the Parabolized Stability Equations in the spatial non-parallel framework (Andersson et al. 1999; Luchini 2000; Levin & Henningson 2003). In the former formulation, the base flow is assumed to be parallel. At the Reynolds number Re=1000, the inflow Reynolds number of the present investigation, it is found that for spanwise wave-numbers β larger than ≈ 0.3 there is no exponential instability of TS/oblique waves. The largest non-modal growth due to the lift-up mechanism is observed at the wave-number pair $(\alpha,\beta)=(0,0.7)$. In the present work we do not restrict ourselves to zero streamwise wave-number $\alpha=0$, but instead we take into account the developing base flow. Indeed the spatially developing base flow allows for transfer of energy between different wave-numbers through the convective terms.

5.1. Optimal initial condition

5.1.1. Spanwise periodic flows

We investigate the potential for growth of initial conditions with different spanwise wave-numbers β by solving the eigenvalue problem (11) for a range of instances of time T. This amounts to performing a series of direct and adjoint numerical simulations until convergence towards the largest eigenvalues of (11) at time T is obtained. If only the largest eigenvalue of (11) is desired it suffices to use a power iteration scheme, whereas if several of the leading eigenvalues are needed, one has to resort to a Krylov/Arnoldi procedure (c.f. Nayar & Ortega 1993; Lehoucq et al. 1997). Both of these approaches are matrix-free and rely on the repeated action of $\exp(\mathcal{A}^{\dagger}T)\exp(\mathcal{A}T)$ on an initial velocity field $\mathbf{u}(0)$. In other words, it is not necessary to store matrices in order to obtain the eigenvalues but to time-integrate the governing equations.

Figure 2a) shows the energy evolution when optimising for different times and for spanwise wave-number $\beta=0.55$. It is at this wave number that the

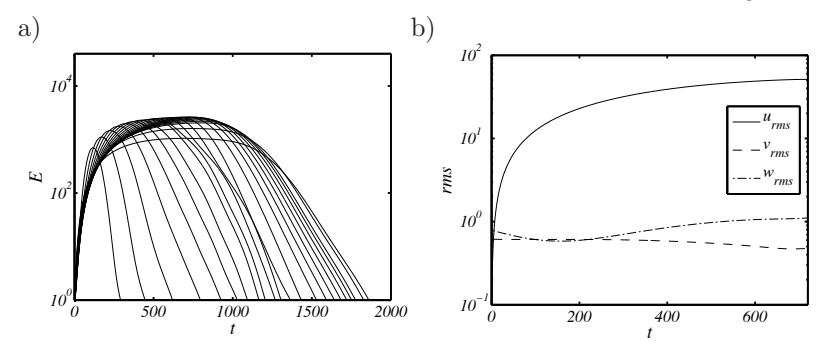


FIGURE 2. a) Energy evolution of the optimal initial conditions for different times T at the wave-number $\beta=0.55$, where the optimal streak growth is obtained. The largest growth is obtained at time T=720. The maximum at each time in this figure defines the envelope growth. b) Component-wise rms-values when optimising for time T=720. A transfer of energy from the wall-normal and spanwise component to the streamwise velocity is observed during the time evolution, clearly showing that the lift-up mechanism is active.

maximum growth due to the lift-up mechanism is found for the configuration under consideration. From figure 2b) it is evident that the disturbance leading to the maximum streak growth at time T=720 exploits the component-wise transfer between velocity components, inherent to the lift-up mechanism. The initial condition is in fact characterised by strong wall-normal v and spanwise w perturbation velocity while the flow at later times is perturbed in its streamwise velocity component.

An important feature of this high Reynolds number flat-plate boundarylayer flow with length $L_x = 800$ is that the combined Orr/Tollmien-Schlichting mechanism is very strong with a growth potential of $\gamma_1 = 2.35 \cdot 10^4$ (see also Bagheri et al. 2009a) for time T = 1800. If, however, the streaks induced by the lift-up mechanism have reached sufficiently large amplitudes to trigger significant non-linear effects, the TS wave transition scenario will be by-passed. In figure 3 a contour map of the maximum growth versus optimisation time and spanwise wave-numbers β is shown. Note that local maxima are obtained in two regions; (I) a low spanwise wave-number regime dominated by the TS/oblique waves where the growth is the largest but slow. (II) For high spanwise wavenumber it is the fast lift-up mechanism that is dominating. The TS/oblique mechanism can be seen to yield one order of magnitude larger growth than the lift-up instability. The global maximum growth is obtained at the wavenumber $\beta = 0.05$ and not for $\beta = 0$. This somewhat surprising result can be explained by the larger initial transient growth of spanwise-dependent perturbations which initiates the TS-waves. The growth rate of the latter is almost

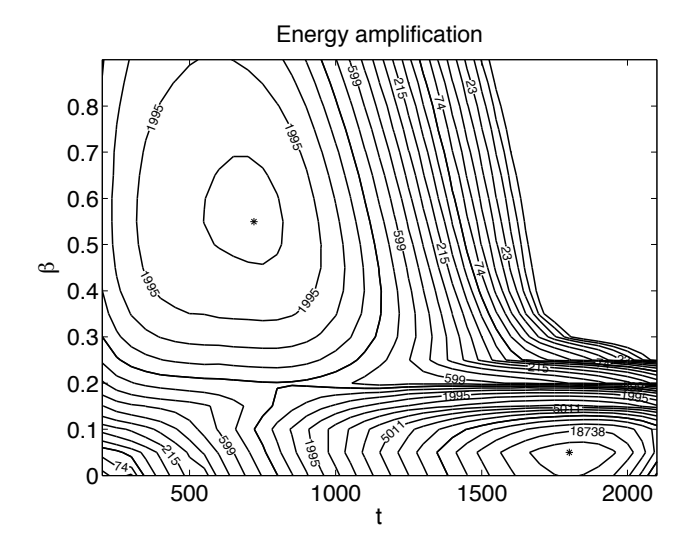


FIGURE 3. Contour map of optimal growth due to initial condition in the time spanwise wave-number domain. The contour levels span three orders of magnitude and thus we use a logarithmic scale. The value on the contours indicate the energy growth corresponding to that line. The maximum streak growth is obtained for $\beta=0.55$ at time T=720 and the amplification factor is $G=2.63\cdot 10^3$. The global maximum is obtained for $\beta=0.05$ at time T=1820, with the streamwise exponential amplification of oblique waves combined with the Orr-mechanism. The amplification factor is $G=2.71\cdot 10^4$.

independent of β for the low values under consideration (see e.g. figure 3.10 in Schmid & Henningson 2001).

The competition between the exponential and algebraic growth was also studied using local theory by Corbett & Bottaro (2000). These authors have shown that as the Reynolds number increases, the growth due to modal instability becomes more pronounced. The results presented in that work for $Re_{\theta}=386$ (equivalent to $Re_{\delta^*}=1000$ in our scaling) indicate that TS instability becomes dominant for final times T>2000. Our results show that in a spatially evolving boundary layer with local Reynolds number Re_{δ^*} ranging between 1000 and 1800 the exponential growth dominates at times larger than about 1250. In the following we study in more detail the disturbances corresponding to the two local maxima mentioned above.

The evolution of the most dangerous initial condition is shown in figure 4. The streamwise velocity component of the optimal initial condition leading to the maximum growth at time T=1820 is depicted together with the flow response at various times. The initial disturbance is as in the two-dimensional

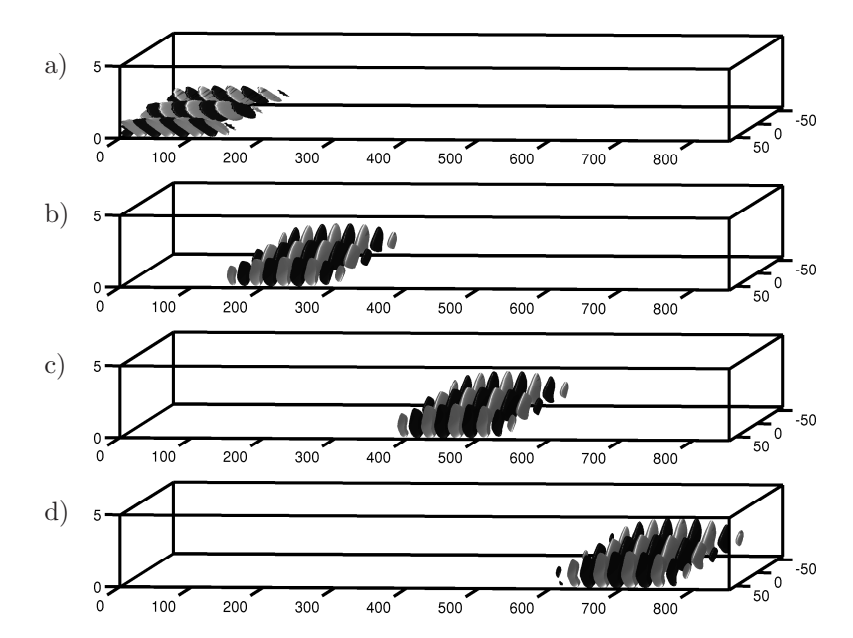


FIGURE 4. Isosurfaces of streamwise component of disturbances at the spanwise wave-number $\beta=0.05$. Red/blue colour signifies isosurfaces corresponding to positive/negative velocities at 10 percent of the maximum. a) Streamwise component of optimal initial condition leading to the global optimal growth at time T=1820. b), c) and d) Corresponding flow responses at times T=400,1000 and 1600

case leaning against the shear of the base flow (see figure 4a). The resulting instability exploits the Orr-mechanism to efficiently initialise the wave packet propagation, eventually giving the disturbance shown in figures 4 b), c) and d).

Figure 5 shows the space-time diagram for the evolution of the three velocity components of the disturbance. Isocontours of the integrated, in spanwise and wall-normal direction, rms-values associated to each component are plotted versus the streamwise direction and time. Since this is a global view of local modal instability there is no significant component-wise transfer of energy and thus the different components of the disturbance evolve (grow) in a similar manner. Weak interactions between the components can be due to non-parallel effects. Additionally, the propagation velocity of the disturbance is estimated from the space-time diagrams by tracking the edges of the disturbance. These edges are defined as the point where the rms-values have amplitude 1%. All the propagation velocities presented will be measured in this way. The leading edge of the wave-packet travels at $c_{le} = 0.51$ while the trailing edge has a

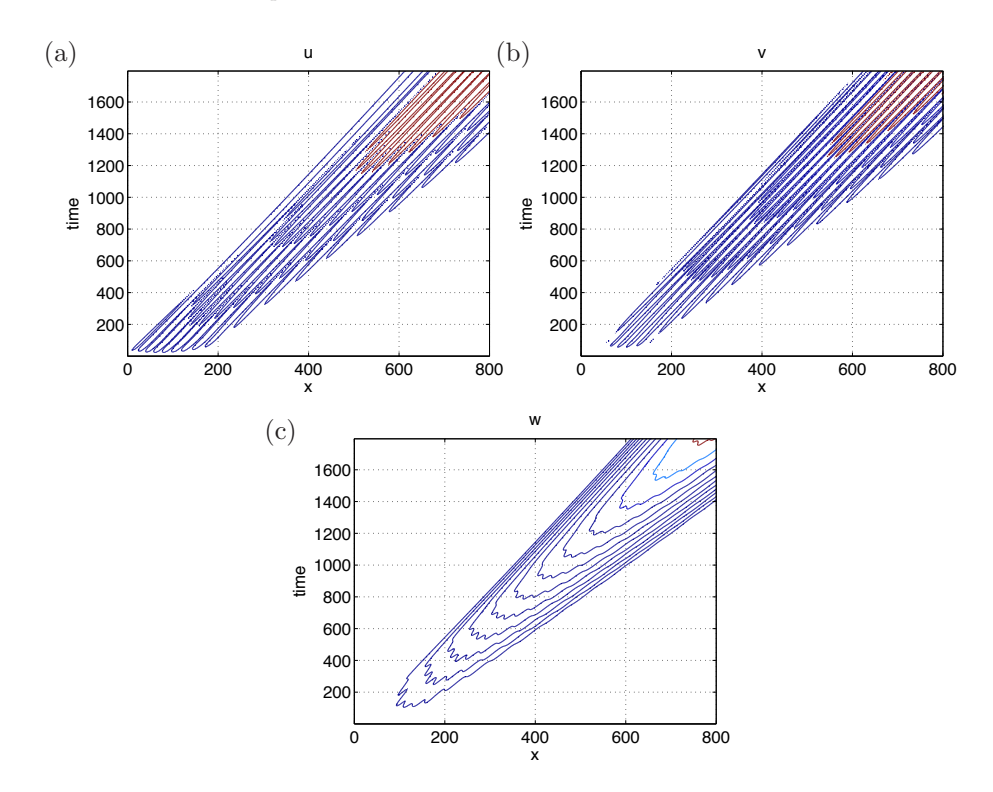


FIGURE 5. Spatio-temporal diagram of the three velocity components of the perturbation for the TS-wave case optimisation time is T=720) ((a) streamwise, (b) wall-normal and (c) spanwise). The propagation velocity of the leading edge of the disturbance is $c_{le}=0.51$ while of the trailing edge is $c_{te}=0.33$.

velocity $c_{te} = 0.33$. These values shows remarkable agreement with the classic results on the propagation of wave-packets by Gaster (1975) and Gaster & Grant (1975).

The optimal initial condition leading to the maximum growth at time T=720 for spanwise wave-number $\beta=0.55$ and the corresponding flow response at various times are shown in figure 6. The initial disturbance is an elongated perturbation with most of its energy (99.94%) in the wall-normal and spanwise velocity components (figure 6a). The resulting instability exploits the lift-up eventually giving the disturbance shown in figures 6 b), c), d) and e). This is a result of local non-modal instability characterised by the strong transfer of energy from the wall-normal and spanwise towards the streamwise velocity component. The wall-normal velocity component is shown in figure 6 b) to suggest that the Orr mechanism is active here as well; it delays the final decay of the streamwise vortices so that they can induce streaks more effectively. Already at time t=100 more than 99% of the kinetic energy of the perturbation

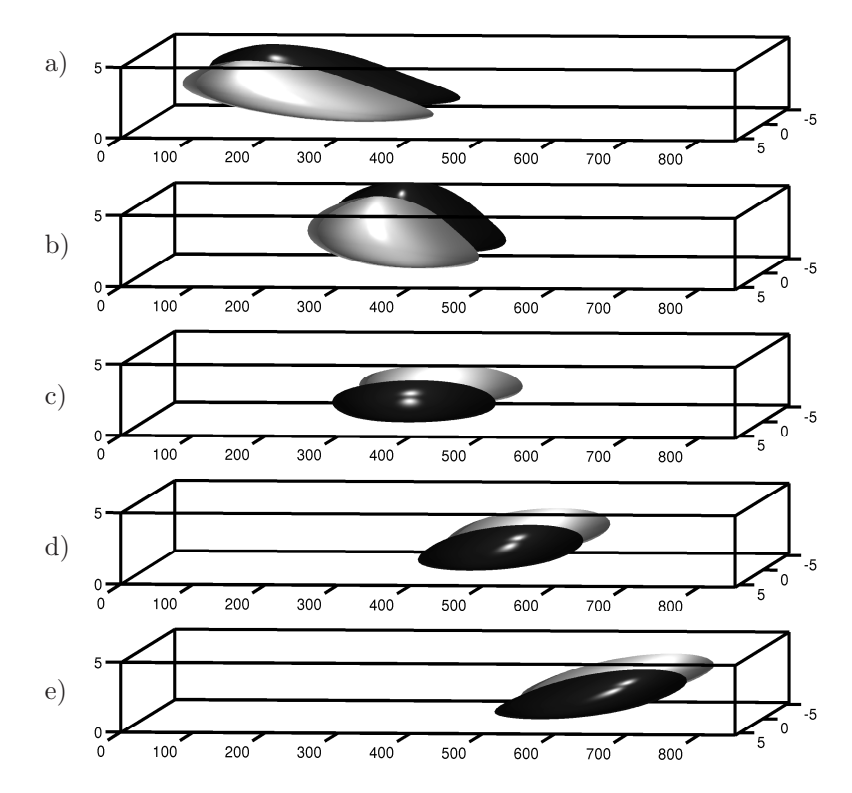


FIGURE 6. Evolution of streamwise velocity when initialising the system with the optimal initial condition at $\beta=0.55$. a) The wall-normal velocity of the optimal initial condition. b) The wall-normal velocity at t=200 with surface levels at ten percent of its maximum value, c) The streamwise velocity at t=200, d) at time t=400 and e) at time t=600. The optimisation time is T=720.

is in the streamwise component. As can be seen, the disturbance evolves into alternating slow and fast moving streaks that are tilted so that the leading edge is higher than the trailing edge as observed in the experimental investigation by Lundell & Alfredsson (2004).

It is also interesting to note that, while the optimal initial condition is streamwise independent for parallel flows, it is localised in the streamwise direction for a spatially growing boundary layer. This indicates that it is most efficient to extract energy from the mean flow further upstream where non parallel effects are stronger. For optimisation times longer than that of the peak value, still with $\beta=0.55$, the initial perturbation is located further upstream and is shorter. This is to compensate for the downstream propagation of perturbations out of the control domain. Conversely, for optimisation times lower than T=720, the initial conditions assumes more and more the form of a

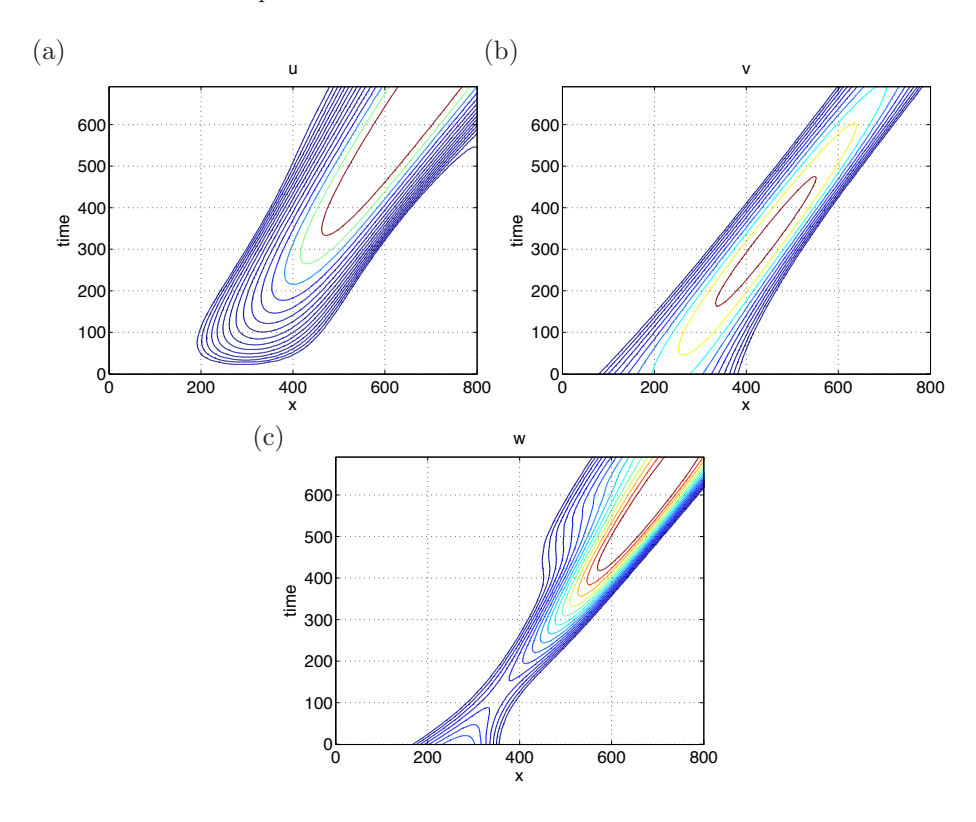


FIGURE 7. Spatio-temporal diagram of the three velocity components of the perturbation for the streak case (optimisation time is T=720) ((a) streamwise, (b) wall-normal and (c) spanwise). The propagation velocity of the leading edge of the disturbance is $c_{le}=0.87$ while of the trailing edge is $c_{te}=0.44$. The two speeds are measured in the second half of the time domain after the initial transient phase.

packet of vortices aligned in the streamwise direction and tilted upstream. The growth is then due to a combined Orr and lift-up mechanism.

The space-time diagram for each velocity component of the streaky optimal perturbation is presented in figure 7. The non-modal nature of the instability and the component wise transfer of energy are seen in the plots. The streamwise component is for large times several orders of magnitude larger that the other two. The propagation velocity of the disturbance is calculated: the leading edge velocity of the "streak-packet" is $c_{le} = 0.87$ while the trailing edge travels at velocity $c_{te} = 0.44$. Note that these values are based on the streamwise velocity component. The propagation velocities of the non-modal streaks are larger than those of modal disturbances. This can be explained by the fact that the disturbances are located in the upper part of the boundary layer, especially the

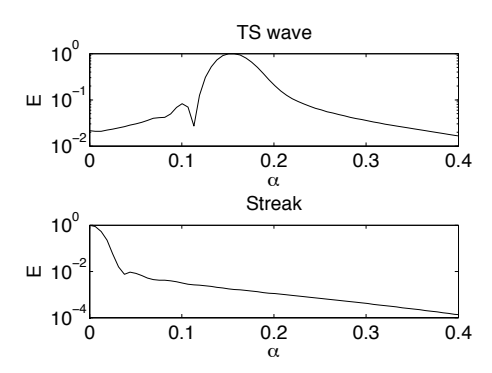


FIGURE 8. Energy spectra along the streamwise direction for the optimal initial condition at for that case $T=1820, \beta=0.05$ (TS-wave) and $T=720, \beta=0.55$ (Streak).

downstream part of it, as deduced also from the three-dimensional visualisation in figure 6. Note finally in the plot for the spanwise velocity component a kink around t=400 and x=400. In this region, the main contribution to the trailing edge of the disturbance changes from streamwise vortices to streamwise streaks. The propagation velocity of the former is thus larger than that of the streaks as confirmed by the reduced slope of the peak contours in figures 7(a) and (b).

To further interpret the present results, we perform a Fourier transform along the streamwise direction of the two disturbances investigated above and compute the energy distribution in the various streamwise wave-numbers α (the energy density is first integrated in wall-normal and spanwise direction). The result shown in figure 8 demonstrates that the TS-wave disturbance has a peak at a relatively higher $\alpha \approx 0.17$, a value in agreement with predictions from local parallel stability calculations. The streak mode, conversely, has most of its energy at the lowest wave-numbers.

Four different optimal initial conditions for $\beta=0.55$ and T=720 are shown in figure 9. The wall-normal velocity component of the eigenvector leading to the maximum growth is reported in 9a). Since the base flow is uniform in the spanwise direction, the second eigenvector has the exact same shape as the first, only shifted half a wavelength in z as shown in figure 9b). These eigenvectors correspond to the same eigenvalue $\gamma_{1,2}=2.6\cdot 10^3$, and they may be combined linearly to obtain a disturbance located at any spanwise position. In figure 9c)-d) the third eigenvector associated with $\gamma_3=2.2\cdot 10^3$ and the fifth associated with $\gamma_5=1.6\cdot 10^3$ are shown respectively. These eigenvectors also come in pairs with matching eigenvalues. It is thus possible with the Arnoldi method to obtain several optimals for a single parameter combination. This has not been done previously for the Blasius flow, while Blackburn $et\ al.\ (2008)$ computed several optimals for the flow past a backward-facing step.

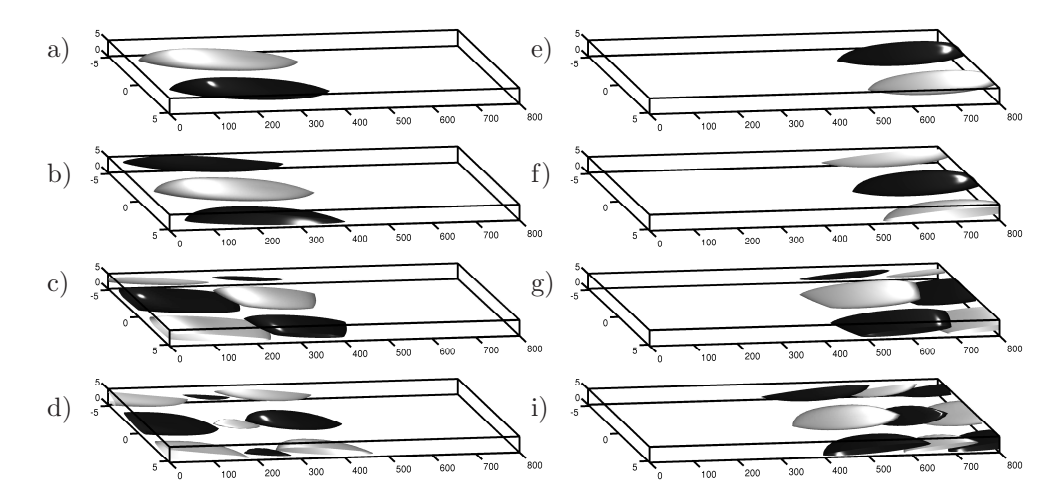


FIGURE 9. Wall-normal component of the leading four eigenvectors for the optimisation problem at $\beta=0.55,\,t=720$ and the corresponding responses. The structures are plotted over one wavelength in the spanwise direction. Red/blue colour indicate isosurfaces corresponding to positive/negative velocities at 10 percent of the maximum. a) The initial condition with largest growth. b) Flow structures corresponding to the second eigenvalue. This is a spanwise shifted version of the first eigenvector. c) Third eigenvector associated to the same eigenvalue as the fourth eigenvector (not shown). d) Fifth eigenvector. In e), f), g) and i) the corresponding responses are shown, in particular the streamwise component. Note that the axes are not at the actual aspect ratio: the structures are far more elongated.

The responses to each of these initial conditions are shown in figures (9ei). One can see that the sub-optimal initial conditions reproduce structures
of shorter extension and with low- and high-speed streaks alternating in the
streamwise direction. Figure (10) shows the energy evolution versus time for
each of the sub-optimals. The energy growth is similar in the beginning, however later on, faster decay is observed with decreasing order of optimality.
Optimal perturbations form an orthogonal basis; this fact may be exploited to
project incoming disturbances and predict their evolution.

5.1.2. Localised optimal initial condition

In this section, we look into the general case of three-dimensional initial disturbances. Using the method described in section 3, along with the necessary modifications explained in section 3, spatially localised optimal initial conditions are sought. A large domain is chosen to allow for a fully three-dimensional

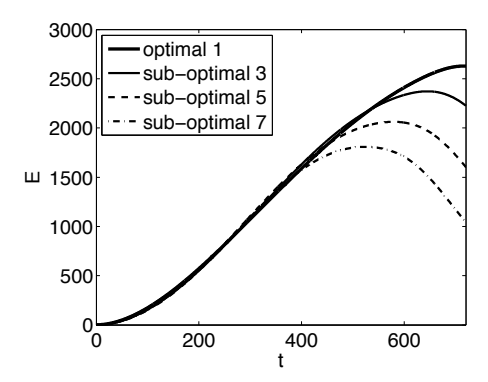


FIGURE 10. The evolution of the energy of the perturbation in time for each of the initial conditions in figure 9. The suboptimals denoted by even number give the same evolution as the corresponding perturbation with odd number.

disturbance to propagate and expand in all directions without interacting with the boundaries. The spanwise width is chosen to be Lz=502.6 (corresponding to the fundamental wave-number $\beta=0.0125$) for the cases with longest optimisation time and Lz=251.3 ($\beta=0.025$) for the shorter optimisation times. Furthermore $n_z=128$ Fourier modes were used in the spanwise direction, instead of 4 for the spanwise periodic cases. This increases the total number of degrees of freedom in our optimisation problem from approximately 1 to 30 millions.

The initial condition is placed near the inflow of the computational domain and power iterations are used to compute the optimal shape of the disturbance inside a fixed region. The area to which the initial condition is limited is $30\delta_0^*$ long and $40\delta_0^*$ wide and it is centred around the location $x=25\delta_0^*$ and z=0. Along the wall-normal direction the optimisation process restricts the perturbation near the wall, inside the boundary layer, hence no additional localisation is adopted. The cases presented here correspond to the two physical mechanisms found to be relevant in the previous section, the Orr/TS-wave scenario and the lift-up process. To excite the two separately, the corresponding optimisation times are chosen to be T=1820 and T=720. In addition, one intermediate case, T=900, where both these two mechanisms are active, is presented.

For the longest optimisation time considered, see figure 11, the TS-wave scenario completely dominates the dynamics. The characteristic upstream tilted structures are present in the initial condition and all the velocity components achieve a significant growth. The wave-packet grows while travelling downstream and it consists of structures almost aligned in the spanwise direction, forming symmetric arches. The three-dimensional nature of this wave-packet is noticeable in the spanwise velocity component of the response, accounting for

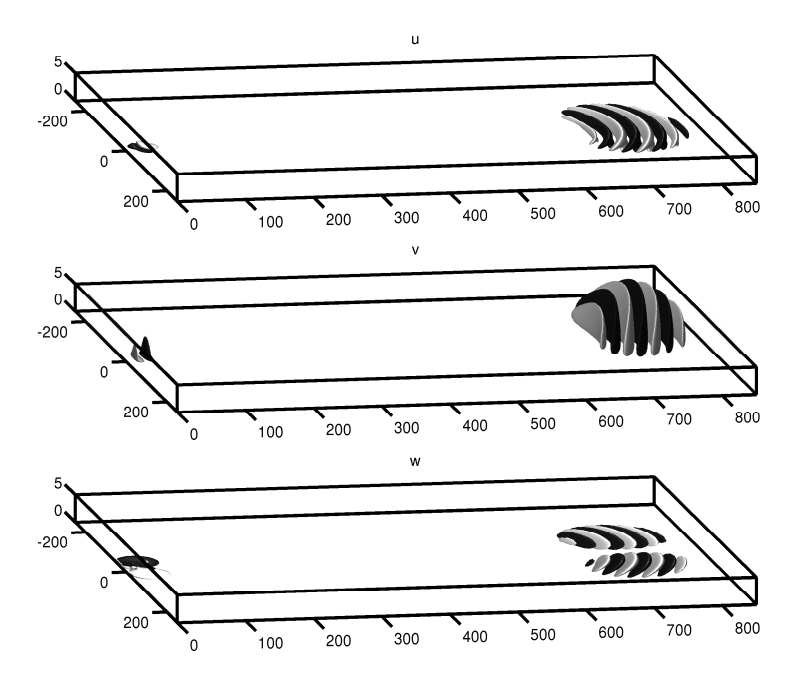


FIGURE 11. Optimal localised initial condition and corresponding response at time T=1820, the optimal TS wavepacket. The amplitudes of each velocity component are reported in table 1.

Time	Comp.	Initial condition	Response	Total growth
	u	0.00398	275.42913	
720	v	0.36452	0.02334	275.76202
	w	0.63149	0.30954	
	u	0.74441	1012.39550	
1820	v	0.00314	278.58122	1763.75695
	w	0.25244	472.78022	

Table 1. Energy of each component of the tree-dimensional optimal initial condition and the corresponding response. The total energy amplification is reported in the last column. All the values are normalised with the total energy of the initial condition.

the spreading of the disturbance normal to the propagation direction and to the presence of unstable oblique waves. As in the case of the spanwise periodic disturbances, the total energy growth due to the streamwise normality (TS-waves for T=1820) is about of one order magnitude larger than the amplification triggered by the lift-up effect at T=720 (component-wise non-normality). Table 1 compiles the energy amplifications for the cases under investigation

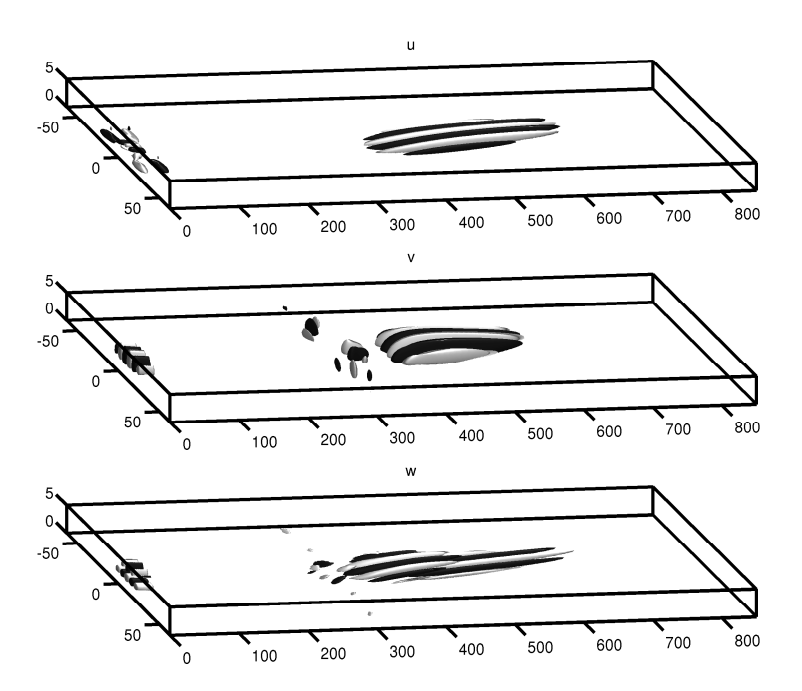


FIGURE 12. Optimal localised initial condition and corresponding response at time T=720, the optimal streaky wavepacket. The amplitudes of each velocity component are reported in table 1.

and reports the value of the energy content in each velocity component for the initial and final conditions.

The flow structures shown in figure 12, with corresponding amplitudes in table 1, document the optimal initial conditions for T=720. The lift-up effect with the formation of streamwise elongated streaks is evident in this case. The initial condition is characterised by strong streamwise vorticity, wall-normal and spanwise velocity components, while the response is predominantly in the streamwise velocity component. Interestingly, we note weak TS-waves propagating behind the streaks (visible in the wall-normal and spanwise velocity components). Since the optimisation time is short, TS-waves will not have the opportunity to grow and their contribution to the initial condition is therefore limited. However, this cannot be zero for a localised initial perturbation. Note further that the spanwise component is found to be weak and hence the spreading of the disturbance in this direction is limited.

The characteristics of the optimal wave-packets are analysed by the spacetime diagrams in figure 13 and 14. Here, the propagation of the disturbance in the streamwise direction is determined by considering the integral of the energy associated with each velocity component in the wall-normal and spanwise

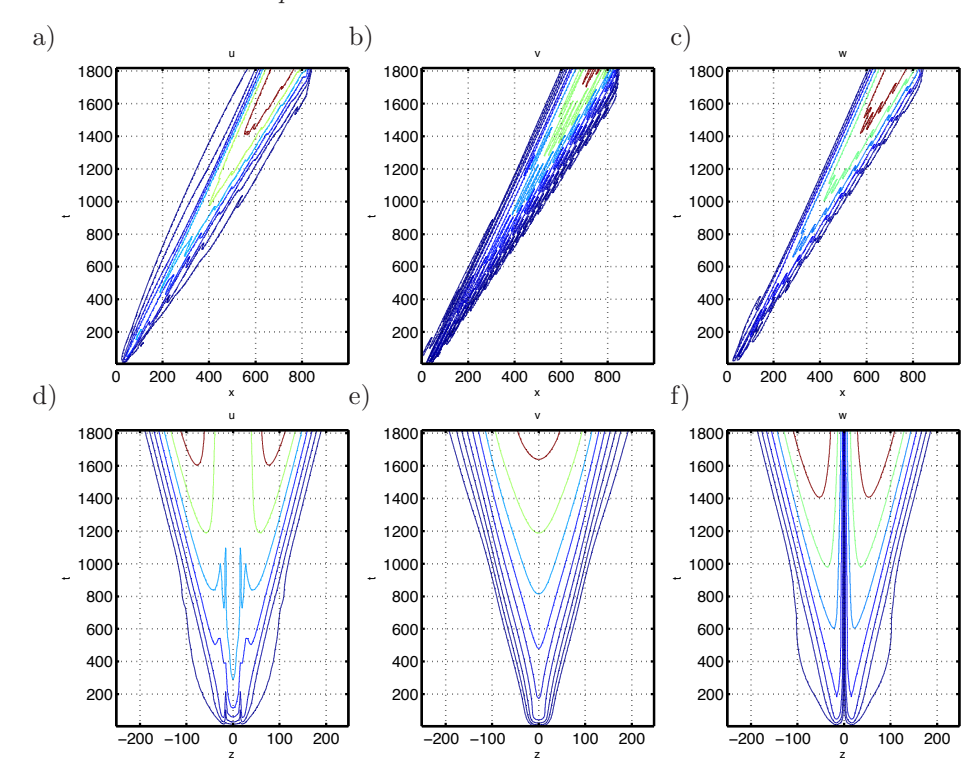


FIGURE 13. Spatio-temporal diagram of the integrated in the wall-normal direction of the rms-values of three velocity components of the perturbation for the optimal TS wave-packet (optimisation time T=1820). Top line shows the spreading of the disturbance in the streamwise direction where the disturbance velocity is integrated in the spanwise and wall-normal direction: (a) streamwise, (b) wall-normal and (c) spanwise velocity component, respectively. (d), (e) and (f) show the evolution in the spanwise direction of the perturbations integrated in the streamwise and wall-normal direction. The propagation velocity of the leading edge of the disturbance is $c_{le}=0.47$ while the trailing edge travels at $c_{te}=0.32$. The spanwise spreading speed at sufficiently large times is $c_z=0.084$.

direction. Similarly, the lateral spreading is computed by integrating the perturbation velocities in the streamwise and wall-normal direction. Comparing the two cases we see that the TS wave-packet expands faster in the spanwise direction while travelling downstream more slowly than the optimal streaky

wave-packet. The propagation velocity of the leading edge of the TS-like disturbance is $c_{le} = 0.47$ while the trailing edge travels at $c_{te} = 0.32$. The spanwise spreading speed is $c_z = 0.084$, corresponding to an angle of $\theta = 11.46^{\circ}$. These values can be compared to those observed experimentally by Gaster (1975); Gaster & Grant (1975) and to the theoretical analysis in Koch (2002). The latter author determined the propagation speed of the leading edge of a localised wave-packet to be 0.5 and the trailing edge velocity to be 0.36 by computing the group velocity of three-dimensional neutral waves. The largest spanwise group velocity was found to be approximately 0.085, a value very close to those reported here. The agreement is remarkable even though the results in Koch (2002) are obtained at a lower Reynolds number, i.e. Re = 580.

The difference between leading and trailing edge of the optimal streaky wave-packet, $c_{le}=0.90$ and $c_{te}=0.36$, explains the larger extension of the latter; while the front travels at the speeds typical of the upper part of the boundary layer where the streaks are located, the trailing edge velocity is that of the unstable waves seen on the rear. The spanwise spreading speed is $c_z=0.0098$, corresponding to an angle of $\theta=0.89^{\circ}$. It should be mentioned that this spreading rate is that of the energetically dominant velocity component, i.e. the streamwise component. The slow lateral diffusion is most likely only due to the effect of viscosity; the growing streaky structures are therefore characterised by zero spanwise propagation velocity.

Figure 14b) and c) clearly demonstrates the short and slower packet of waves following the main streaky structures. As mentioned above, the spanwise propagation of the streamwise vortices and streaks is limited; conversely, the sequence of waves on the rear part of the wave-packet has a spanwise spreading rate comparable to that of the TS wave packet, in particular the value $c_z = 0.073$ is obtained by considering the energy of the spanwise velocity component.

Finally, we computed optimal disturbances for intermediate optimisation times and the amplifications were generally lower than in the two previous cases. However it was interesting to notice that for times around 800 to 900 perturbations containing both streaky and wavy structures emerge. The spectrum of the initial conditions contains a broad range of disturbances. Interestingly, the flow response is again characterised by short-wavelength instability waves following elongated streaks, apparent only in the streamwise velocity component. The TS wave-packet becomes more and more relevant as the optimisation time increases.

5.2. Optimal forcing

5.2.1. Global forcing

Since boundary layers are convectively unstable, thereby acting as noise amplifiers, a prominent role is played by the response to forcing, rather than by the detailed time-evolution of the initial condition; The optimal forcing is therefore a relevant measure of the maximum possible growth that may be observed in the computational domain. Analysis of the frequency response can also have

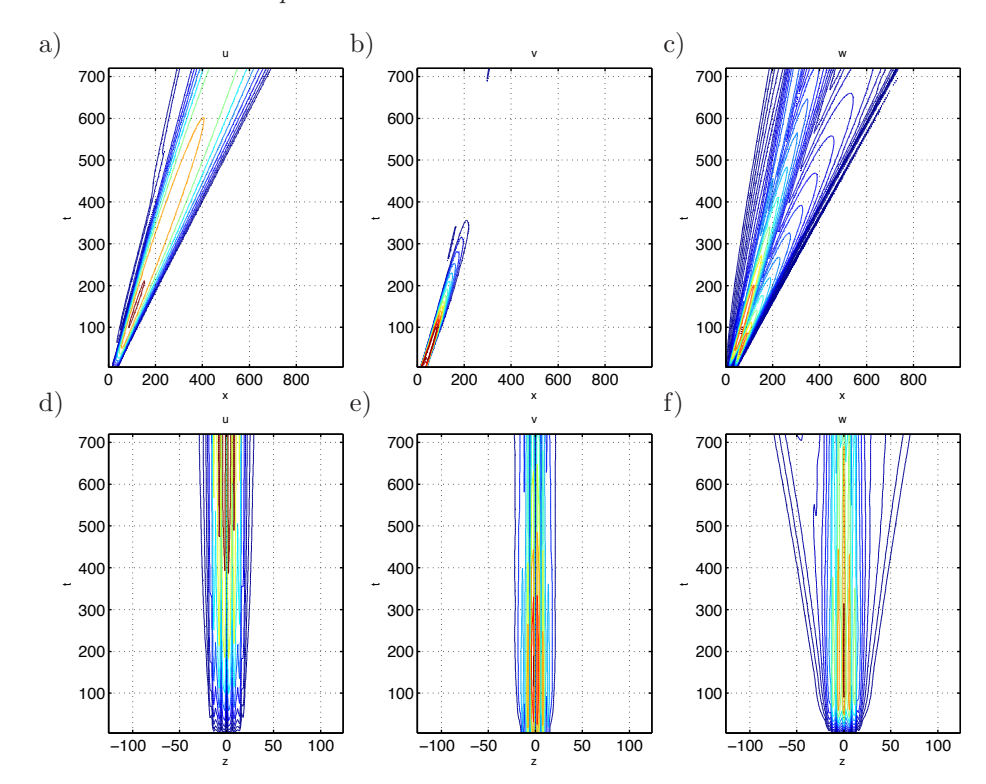


FIGURE 14. Spatio-temporal diagram of the integrated in the wall-normal direction of the rms-values of three velocity components of the perturbation for the optimal streaky wave-packet (optimisation time T=720). Top line shows the propagation of the disturbance in the streamwise direction where the disturbance velocity is integrated in the spanwise and wall-normal direction: (a) streamwise, (b) wall-normal and (c) spanwise velocity component, respectively. (d), (e) and (f) show the evolution in the spanwise direction of the perturbations integrated in the streamwise and wall-normal direction. The propagation velocity of the leading edge of the disturbance is $c_{le}=0.90$ while the trailing edge travels at $c_{te}=0.36$. The spanwise spreading speed is $c_z=0.0098$ (based on the u-component).

implications for control revealing the forcing location and frequencies to which the flow is most sensitive. While the evolution of the optimal initial condition consists of the propagation and amplification of a wave packet, eventually leaving the computational box (or measurement section), the response of the flow to periodic forcing will consist of structures with a fixed amplitude at

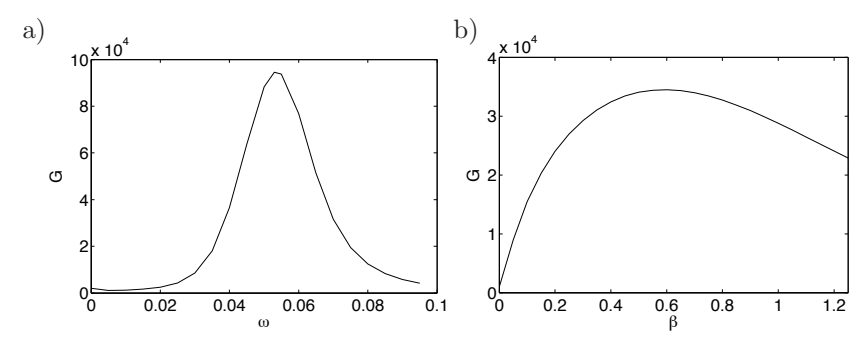


FIGURE 15. a) Frequency response for zero spanwise wavenumber *i.e.* two-dimensional disturbances. The optimal response is obtained for the frequency $\omega=0.055$. b) Response to zero frequency forcing $\omega=0$ for different spanwise wavenumbers. The maximum response is obtained at $\beta=0.6$

each streamwise station, oscillating around the mean flow. We investigate the structure of the optimal forcing and the corresponding response for a range of spanwise wave-numbers and frequencies. Thus, for each wave number we examine a number of temporal frequencies. Ideally we would like to solve the linearized Navier-Stokes equations for very large times, ensuring that we are only considering the regime (long-time) response at the specific frequency under investigation. In practice however we are restricted to a finite final time by the computational cost of solving the direct and adjoint equations involved in the iteration scheme. Using power iterations to find the largest eigenpair typically requires from approximately 15 iterations to about 100 for the most stable frequencies; in other words we need to integrate the governing equations at least 30 times. As can be deduced from the results in the previous section, transiently growing perturbations of small spanwise scale leave our domain at time $t \approx 2000$, while locally unstable TS-waves propagates at a speed of about $0.3~U_{\infty}$. This observation, along with several convergence tests using different integration intervals to extract the flow regime response lead to the conclusion that integration to T = 5000 is long enough to observe the pure frequency

Figure 15 shows the square of the resolvent norm, i.e. the response to forcing for the two limiting cases $\beta=0$ and $\omega=0$. In figure 15a) the response to two-dimensional forcing, inducing perturbations with $\beta=0$, is displayed. The maximum response is observed for the frequency $\omega=0.055$. This maximum is obtained at the frequency where the least stable TS eigenvalue is located (see Bagheri et al. 2009a). Indeed it is known that by projecting the dynamics of the flow onto the basis of eigenmodes, the response to forcing is given by the combination of resonant effects (distance in the complex plane from forcing frequency to eigenvalue) and non-modal effects, i.e. the cooperating non-orthogonal eigenvectors (Schmid & Henningson 2001). In Åkervik et al.

(2008) it was shown for a similar flow that non-normal eigenvectors could induce a response about twenty times larger than that induced only by resonant effects.

The response to zero temporal frequency for different spanwise wavenumbers β is shown in figure 15b), where according to local theory the maximum response is expected for spanwise periodic excitations. The maximum growth may be observed for the wave-number $\beta=0.6$, a slightly larger value than for the optimal initial condition case. Notice that in the case of optimal forcing there is a smaller difference in the maximum gain between the two different dominating mechanisms (TS-waves vs. streaks).

A full parameter study has been carried out in the frequency–spanwise wave-number (ω,β) plane. A contour map showing the regime response to optimal forcing is displayed in figure 16. As in the case of the optimal initial condition, the global maximum response to forcing is observed for $\beta=0.05$. It reaches this maximum for the frequency $\omega=0.055$. A second region of strong amplification is found for low frequencies and high spanwise wave-numbers. Here the most amplified structures consist of streamwise elongated streaks induced by cross-stream forcing. At the largest spanwise wave-numbers, we also observe that the decay of the amplification when increasing the forcing frequencies is rather slow. Conversely, the peak corresponding to excitation of the TS-waves is more pronounced.

A visualisation of the overall maximum amplification, found for the spanwise wave-number of $\beta=0.05$ and for the same frequency $\omega=0.55$ yielding the optimal two-dimensional forcing, is presented next. The optimal forcing in the streamwise momentum equation and the streamwise velocity component of the optimal response are shown in figure 17. The optimal forcing structures lean against the shear (see figure 17a) to optimally trigger the Orr mechanism; the regime long-time response of the flow, shown in figure 17b), reveals the appearance of amplified TS-waves at the downstream end of the computational domain.

The optimal forcing structure at $\beta=0.6$ and the zero frequency has almost all its energy in the spanwise and wall normal components, that is the flow is forced optimally in the wall-normal and spanwise direction as shown among others by Jovanovic & Bamieh (2005) for channel flows. The wall-normal and spanwise components of the forcing are displayed in figure 18a) and b). The rms values of the streamwise component of the forcing is only two percent of that of its spanwise and wall-normal counterparts. The lift-up effect transfers momentum into the streamwise component (shown in figure 18c), which contains 99.99 percent of the energy of the flow response. The streak amplitude increases in the streamwise direction until the fringe region is encountered.

The Fourier transform along the streamwise direction of the two disturbances investigated above is shown in figure 19. As in the case of the optimal initial conditions in figure 8, the energy density is first integrated in the wall-normal and spanwise direction. The results indicate that the TS-wave disturbance has

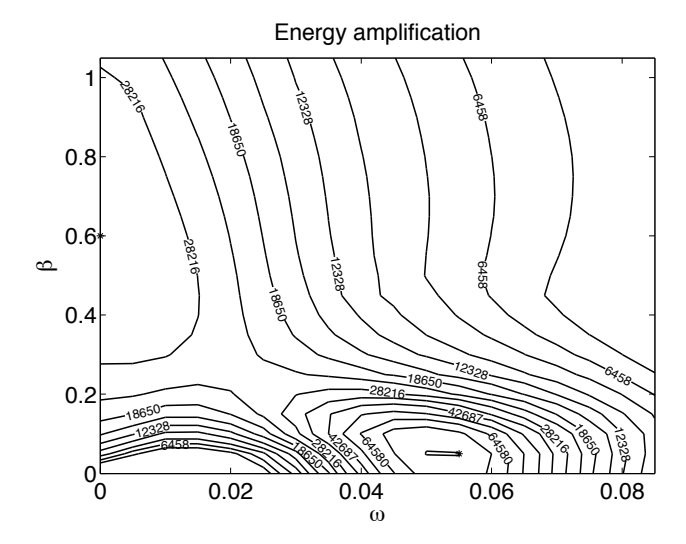


FIGURE 16. Contour map of response to forcing with frequency ω versus spanwise wave-number β . The contour levels span three orders of magnitude and thus we use a logarithmic scale. The value on the contours indicate the energy growth corresponding to that line. The maximum response to forcing is observed for $\beta=0.05$ and for the frequency $\omega=0.055$. The amplification factor is $G=1.01\cdot 10^5$. The maximum growth due to the streak mechanism is found for the spanwise wavenumber $\beta=0.6$ at $\omega=0$ where the amplification factor is $G=3.45\cdot 10^4$.

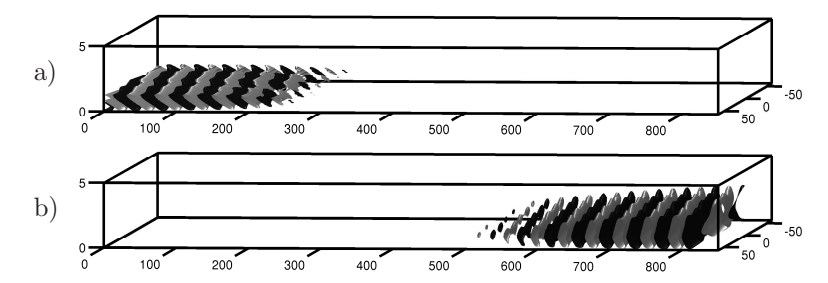


FIGURE 17. Isosurfaces of optimal forcing and response for the streamwise wave-number $\beta=0.05$ subject to forcing at the frequency $\omega=0.055$. Red/blue colour signifies isosurfaces corresponding to positive/negative velocities at 10 percent of the maximum. a) Streamwise component of optimal forcing structure. b) Streamwise velocity component of the response.

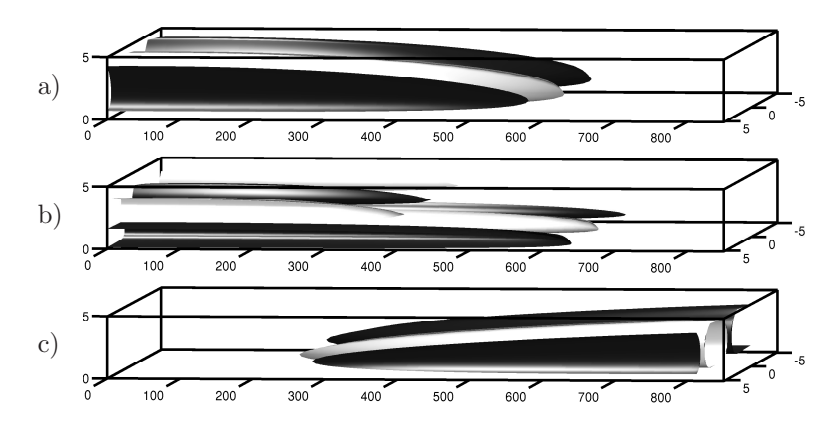


FIGURE 18. Isosurfaces of optimal forcing and response for the streamwise wave-number $\beta=0.6$ subject to steady forcing. Red/blue colour indicates isosurfaces corresponding to positive/negative velocities at 10 percent of the maximum. a) Wall-normal component of optimal forcing structure. b) Spanwise component of optimal forcing. c) Streamwise velocity component of the flow response. Both the forcing structures and the response are highly elongated in the streamwise direction.

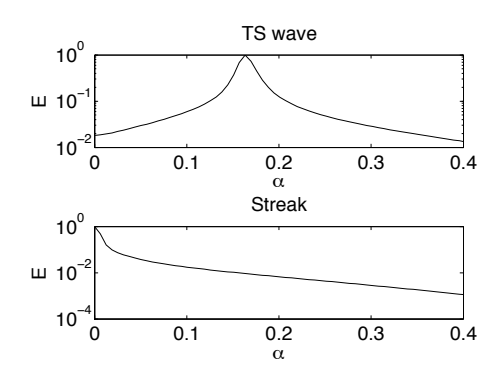


FIGURE 19. Energy spectra along the streamwise direction for the optimal forcing at for that case $\omega = 0.055$, $\beta = 0.05$ (TS-wave) and $\omega = 0$, $\beta = 0.6$ (Streak).

a peak at a relatively high $\alpha \approx 0.17$ while the zero-frequency forcing is concentrated at the lowest wave-numbers. The peak at the wave-number of the most unstable TS-waves is more evident in the case of forcing than in the case of the optimal initial condition (see figure 8).



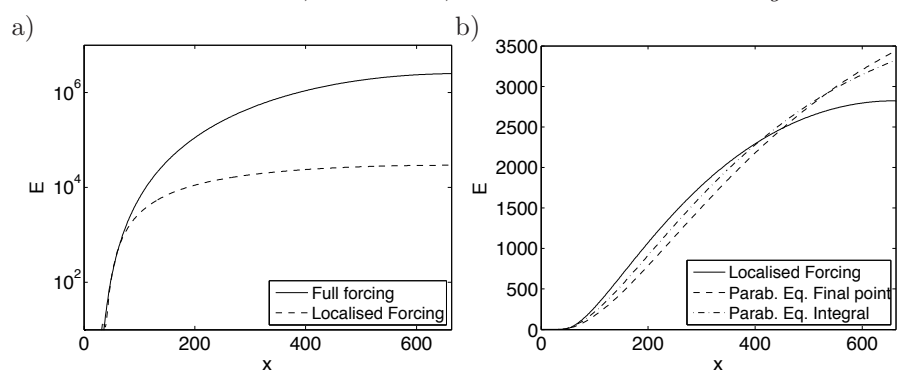


FIGURE 20. Downstream evolution of the kinetic energy of the flow integrated over cross-stream planes. In a) blue and green lines are used to indicate the response to steady forcing active everywhere in the domain ("Full forcing") and in a short region near the inflow ("Localised forcing") respectively. The data are scaled with the magnitude of the forcing computed as integral over the whole domain. In b) the blue line corresponds to the case of localised forcing in a) while green ("Parab. Eq. Final Point") indicates the evolution of the optimal initial condition yielding the largest possible kinetic energy at the downstream location $662\delta_0^*$ (Levin & Henningson 2003), and the red line ("Parab. Eq. Integral") the evolution of optimal initial condition yielding the largest integral over the streamwise domain. In order to make a physically relevant comparison we have scaled the data pertaining to the "Localised Forcing" with the value of the response just downstream of the forcing region. The centre of the forcing is at the location $x=32.3\delta_0^*$ corresponding to the optimal upstream location in Levin & Henningson (2003).

5.2.2. Localised forcing

In this section we present results obtained by restricting the forcing to a small region near the inflow of the computational domain. The formulation presented in section 4 is altered by multiplying the forcing \mathbf{f} with a function $\lambda(x)$ which is non zero only in a short streamwise region. The edges of this region are defined by two smooth step functions rising from zero to one over a distance of about $1\delta_0^*$. The centre of the forcing is chosen to be at $x=23\delta_0^*$ with width of $4\delta_0^*$ if not otherwise stated.

This problem is physically closer to the case when disturbances are generated upstream, closer to the leading edge, and their evolution is monitored as they are convected downstream. Initially a comparison with optimal upstream disturbances calculated by means of the Parabolized equations is thus presented (see results in Levin & Henningson 2003).

To this aim, we compute the optimal localised steady forcing for spanwise wave-number $\beta=0.53$ at $x=32.3\delta_0^*$. These were found to be the location and spanwise scale of the overall optimal in Levin & Henningson (2003); in their scalings they correspond to X=0.37 and $\beta=0.53$ for an initial perturbation downstream of the leading edge with Reynolds-number independent evolution, here assumed to be $Re_x=10^6$.

In figure 20 the streamwise growth of the energy of the perturbation obtained with four different approaches is shown. In figure 20a we compare the flow regime response to steady forcing active everywhere in the domain with the response to forcing localised upstream. Further, the latter is compared in figure 20b with the evolution of the optimal initial conditions yielding the largest possible kinetic energy at the downstream location $662\delta_0^*$ and with the evolution of the optimal upstream velocity profile yielding the largest integral of the perturbation energy over the whole streamwise domain (see also Cathalifaud & Luchini 2000). The two latter are computed with the parabolic stability equations (David Tempelmann, private communication); the case having as objective function the integral of the perturbation energy is indeed more relevant for comparison with the present results. It can be seen that the growth is faster when the forcing is active everywhere in our control domain since the component-wise transfer of energy is at work at every streamwise position. The two curves obtained with the parabolic equations (figure 20a) are similar: faster growth is observed when the control optimises over the whole domain, while a larger final level is reached when the objective is limited to the last downstream station. The comparison between the response to "localised forcing" and the "parabolic equations" cases reveals good agreement. The main differences between the two methods are the different set of equations and the way the disturbance is introduced. In Levin & Henningson (2003) and Cathalifaud & Luchini (2000) the linearised boundary-layer equations are used, whereas we use the Navier-Stokes equations. In addition, an optimal upstream boundary condition is computed in Levin & Henningson (2003), whereas an optimal forcing is sought here.

Figure 21a) displays the structure of the optimal forcing function for the case of localised excitation. The wall-normal profiles shown in the plot are obtained by integrating the forcing in the streamwise direction. Figure 21b) and c) depict instead the optimal initial condition obtained with the parabolic boundary-layer equations, i.e. a streamwise vortex pair. The structure of the disturbances are remarkably similar; in the case of the optimal forcing (figure 21a), the action is located closer to the wall with a relatively weaker wall-normal component. When comparing the cases in b) and c) one can note that the vortices leading to the largest possible energy downstream are located further up into the free-stream. Conversely, when the perturbations are required to grow over the whole domain, the disturbance needs to be located in the shear layer so that its effect can be readily felt (cf. figure 21a and c). The results in the figure indicate that forcing the momentum equation is less

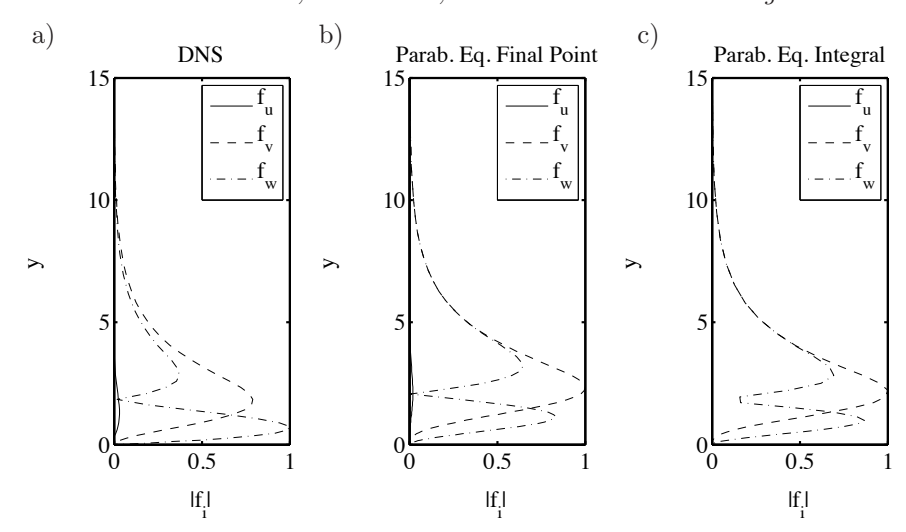


FIGURE 21. Wall-normal profiles of the streamwise, spanwise and wall-normal components of a) the optimal localised forcing (integrated in the streamwise direction), b) the initial condition yielding the largest possible kinetic energy at the downstream location $662\delta_0^*$; c) the initial condition yielding the largest integral of the disturbance energy over the streamwise domain.

effective in the free stream: optimal forcing thus induces streaks which grow for a shorter downstream distance.

A parameter study is conducted to examine the effect of frequency and spanwise scale of the localised forcing. First the results obtained when varying the spanwise wave-number are shown (figure 22). The downstream evolution originating from optimal localised disturbances of zero frequency are displayed for the spanwise wave-numbers investigated. A slower energy growth is observed for the lower wave-numbers owing to the lower forcing to the streaks (proportional to β); the wave-number giving the largest peak response for the present configuration is $\beta = 0.8$. Forcing of smaller scales induce streaks rapidly, but viscous dissipation causes earlier decay.

As shown by Andersson et al. (2001), among others, in the range of validity of the boundary layer equations there is a coupling between the streamwise and spanwise length scale of the disturbance. It is in fact possible to show that a streak family u(x,y,z), defined by the spanwise wave-number β_0 , is independent of the Reynolds number. This results in a scaling property that couples the streamwise and spanwise scales, implying that the same solution is valid for every combination of the streamwise location $x + x_0$ (distance from the leading edge) and of β such that their product stays constant. In other

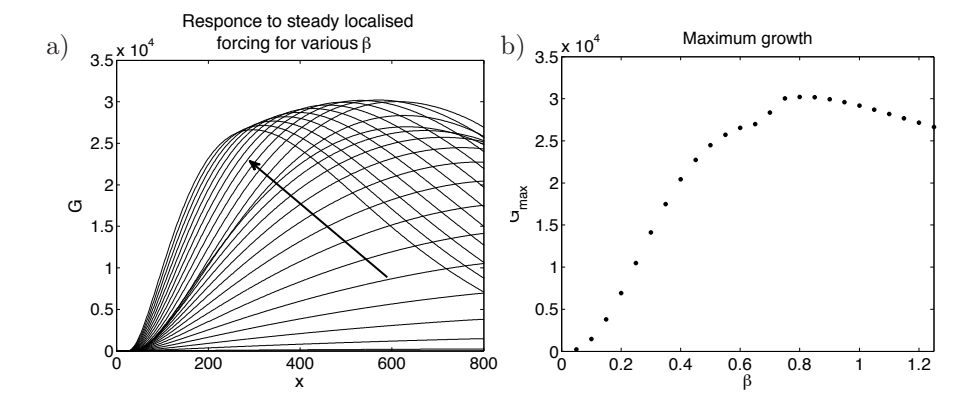


FIGURE 22. a) Streamwise evolution of the response to steady localised forcing for different spanwise wave-numbers β . The arrow indicates increasing β . b) Maximum response versus spanwise wave-numbers.

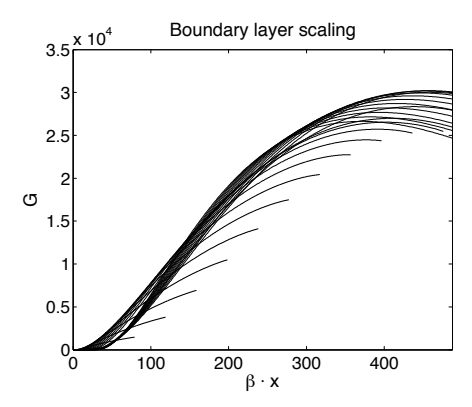


FIGURE 23. Streamwise evolution of the response to localised forcing for different spanwise wave-numbers β where the streamwise position x is scaled with β . The distance from the leading edge is considered to re-scale the data.

words, this amounts to moving along the plate and varying the spanwise wavenumber so that the local spanwise wave-number $\beta_0 \delta^* / \delta_0^*$ remains constant (see also Brandt *et al.* 2003). To further examine this scaling property, the streamwise coordinate in figure 22a) is multiplied by the spanwise wave-number of the disturbance and the result shown in figure 23. Despite the fact that the streamwise extent of each curve is different, the curves indicating the evolution of the streaky disturbance collapse notably, thus confirming the similarity of the boundary-layer streaks.

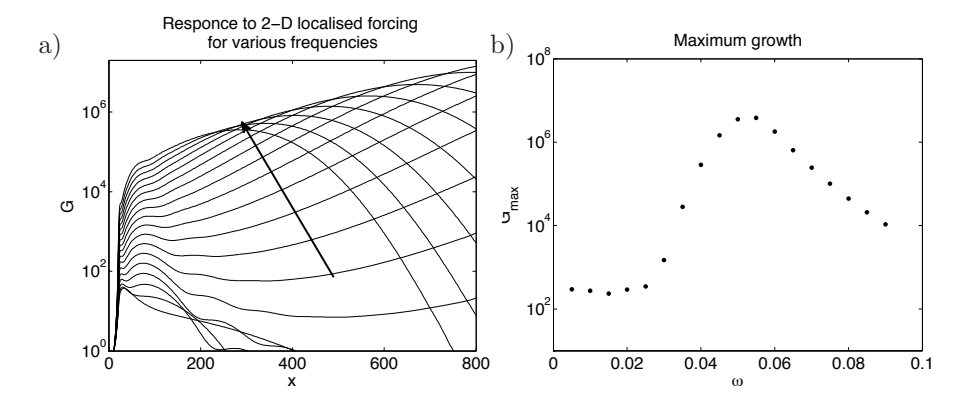


FIGURE 24. a) Streamwise evolution of the response to localised forcing for different temporal frequencies ω . The arrow indicates increasing ω . b) Maximum growth with respect to ω . The spanwise wavenumber is $\beta=0$.

Finally we investigate the case of zero spanwise number (pure two-dimensional disturbances) and vary the temporal frequency. The results are shown in figure 24. The growth observed here is due to the combined Orr and TS-wave mechanism and thus the value of the optimal frequency is close to that obtained when forcing over the whole domain, $\omega=0.055$. The structure of the optimal forcing for the frequency with largest amplification is displayed in figure 25. The excitation is localised closer to the wall, well inside the boundary layer, when compared to the forcing forming streamwise streaks, see figure 21. Forcing the streamwise momentum equation is significantly more efficient at triggering the Orr mechanism and the subsequent wave packet of two-dimensional TS waves.

6. Conclusions

We have used a Lagrange multiplier technique in conjunction with direct and adjoint linearized Navier—Stokes equations in order to quantify the growth potential in the spatially developing flat-plate boundary-layer flow at moderately high Reynolds. Spanwise periodic and fully three-dimensional disturbances are investigated. We consider both the initial conditions leading to the largest possible energy amplification at time T and the optimal spatial structure of time-periodic forcing. To the best of our knowledge, the pseudo-spectrum of the governing operator along real frequencies is computed here for the first time with matrix-free methods. The optimisation framework adopted does not restrict us to assume slow variation of the base flow in the streamwise direction, common to both the first order approximation of the OSS formulation and the more advanced PSE approximation. Specifically we do not, as in the PSE framework, need different equations to describe the lift-up instability and the wave packet propagation.

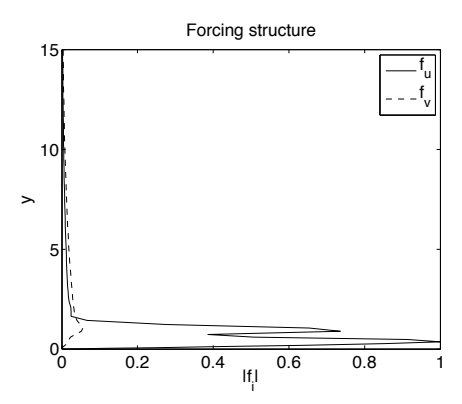


FIGURE 25. Localised forcing with frequency. We plot the streamwise and wall-normal components of the forcing function. The quantities are integrated in the streamwise direction. Note that this is a 2D structure thus the spanwise component is zero.

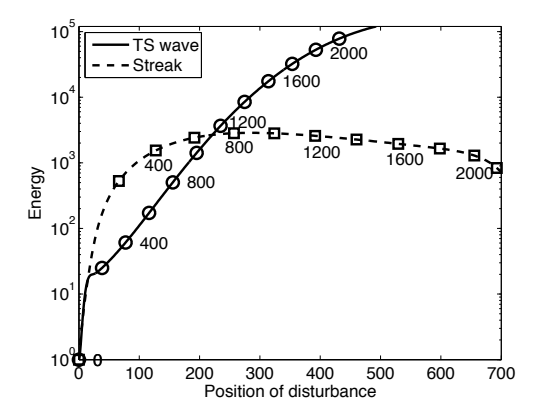


FIGURE 26. Evolution of the kinetic energy of the two optimal initial perturbations for t=720 (streaks) and t=1820 (TS-waves) versus the current spatial position. The position of the disturbance is computed by tracking its 'centre of mass' using the kinetic energy as density. The numbers beside the markers correspond to time instances.

For the optimal initial condition we find that the largest potential for growth is found at small spanwise wave-numbers and consists of upstream tilted structures, enabling the subsequent disturbances to exploit the Orr mechanism and the local convective instability of the oblique wave packet of Tollmien-Schlichting waves. The length and position of the initial disturbance is related to the final time of the optimisation: short time evolution requires the

wave-packet to be initiated further downstream in the region of largest local instability and vice-versa for longer optimisation times. The lift-up instability mechanism inherent to spanwise wavelengths of the order of the boundary layer thickness is faster than the Orr/oblique instability; for the present configuration the streaks reach their maximum energy earlier; conversely, the TS-wave instability needs more time to extract the same amount of energy, at the same time travelling a shorter distance. The evolution of the kinetic energy of these two perturbations in time and space is displayed in figure 26. The results indicate that streamwise vortices of finite length become optimal once a spatially-evolving boundary layer with inflow/outflow conditions is considered. As concerns the optimal response to periodic forcing, the difference in the two instabilities is less pronounced. In this case, the Orr/oblique wave instability only manages to gain a factor of two in energy more than the streak mechanism. The largest amplification of the local convective instability over the non-modal streak generation can be explained by the long computational box examined and the relatively high inflow Reynolds number. Starting closer to the leading edge, one can expect streaks to dominate the transition scenario.

Three-dimensional localised optimal initial conditions are also computed and the corresponding wave-packets examined. For short optimisation times, the optimal disturbances consist of streaky structures propagating and elongating downstream without any significant spreading in the lateral direction. For long optimisation times, conversely, the optimal disturbances are characterised by wave-packets of TS-waves. These travel at lower streamwise speed and with faster spreading in the spanwise direction. The latter can achieve the largest possible energy amplification. Intermediate optimisation times are also considered where both the TS- and streak-mechanism are relevant. The wave-packet has therefore features from both scenarios previously considered: It consists of elongated streaks in the streamwise velocity component, followed by short-wavelength instability waves, mainly evident in the cross-stream velocities.

Finally, we examine the effect of upstream disturbances on the boundary layer flow. Thus we introduce a localised forcing near the inflow of the computational box and compute the forcing structure that provides the largest response over our control domain. First, we compare with results based on the solution of the parabolized Navier-Stokes equations: good agreement is obtained, despite the differences between the two methods. Secondly, we investigate zero-frequency upstream forcing and show a maximum for perturbations with spanwise wave-number larger than that obtained when the forcing location is not constrained. Thirdly, analysis of time-periodic two-dimensional forcing is considered: the findings agree with those obtained with distributed forcing since the flow response corresponds in both cases to exponentially growing Tollmien-Schlichting waves at the forcing frequency.

Three different destabilising mechanisms are considered in this study, all at work in the boundary layer flow. Although these could be explained using the OSS equations, they are analysed without any simplifying assumptions. The present work is of a more general character. By choosing an objective function and using the full linearized Navier—Stokes equations as constraints we are not limiting ourselves to simple geometries. Whenever a DNS code is available to accurately describe a flow, all that is needed in order to investigate the stability characteristics is a linearised version of the code and the implementation of the corresponding adjoint equations along with a wrapper built around these two simulations ensuring the correct optimisation scheme. The method used here is therefore applicable to any geometrical configuration.

Acknowledgements

The authors wish to thank David Tempelmann for providing data from the parabolic stability equations and for many fruitful discussions. Inspiring comments on the manuscript from Carlo Cossu are acknowledged as well. Computer time provided by SNIC (Swedish National Infrastructure for Computing) is gratefully acknowledged. The present work is supported by the Swedish research council which is gratefully acknowledged.

References

- ÅKERVIK, E., EHRENSTEIN, U., GALLAIRE, F. & HENNINGSON, D. S. 2008 Global two-dimensional stability measures of the flat plate boundary-layer flow. *Eur. J. Mech. B/Fluids* **27**, 501–513.
- ÄKERVIK, E., HŒPFFNER, J., EHRENSTEIN, U. & HENNINGSON, D. S. 2007 Optimal growth, model reduction and control in a separated boundary-layer flow using global eigenmodes. *J. Fluid Mech.* **579**, 305–314.
- ALIZARD, F., CHERUBINI, S. & ROBINET, J-C. 2009 Sensitivity and optimal forcing response in separated boundary layer flows. *Phys. Fluids* **21** (064108).
- Andersson, P., Berggren, M. & Henningson, D. S. 1999 Optimal disturbances and bypass transition in boundary layers. *Phys. Fluids* 11, 134–150.
- Andersson, P., Brandt, L., Bottaro, A. & Henningson, D. S. 2001 On the breakdown of boundary layers streaks. *J. Fluid Mech.* **428**, 29–60.
- Bagheri, S., Åkervik, E., Brandt, L. & Henningson, D. S. 2009a Matrix-free methods for the stability and control of boundary layers. AIAA J. 47, 1057–1068.
- Bagheri, S., Brandt, L. & Henningson, D. S. 2009b Input-output analysis, model reduction and control of the flat-plate boundary layer. *J. Fluid Mech.* **620**, 263–298
- Barkley, D., Blackburn, H. M. & Sherwin, S. J. 2008 Direct optimal growth analysis for timesteppers. *Itn. J. Numer. Meth. Fluids* **57**, 1435–1458.
- Blackburn, H. M., Barkley, D. & Sherwin, S. J. 2008 Convective instability and transient growth in flow over a backward-facing step. *J. Fluid Mech.* **608**, 271–304.
- Brandt, L., Cossu, C., Chomaz, J.-M., Huerre, P. & Henningson, D. S. 2003 On the convectively unstable nature of optimal streaks in boundary layers. *J. Fluid Mech.* **485**, 221–242.
- Butler, K. M. & Farrell, B. F. 1992 Three-dimensional optimal perturbations in viscous shear flow. *Phys. Fluids A* 4, 1637–1650.
- Cathalifaud, P. & Luchini, Paolo 2000 Algebraic growth in boundary layers: Optimal control by blowing and suction at the wall. *Eur. J. Mech. B Fluids* 19, 469–490.
- Chevalier, M., Schlatter, P., Lundbladh, A. & S., Henningson D. 2007 A pseudo spectral solver for incompressible boundary layer flows. *Technical Report*, *Trita-Mek* 7.
- Chomaz, J. M. 2005 Global instabilities in spatially developing flows: non-normality and nonlinearity. *Annu. Rev. Fluid Mech.* **37**, 357–392.
- CORBETT, P. & BOTTARO, A. 2000 Optimal perturbations for boundary layers subject to stream-wise pressure gradient. *Phys. Fluids* **12** (1), 120–130.
- Cossu, C. & Chomaz, J.M. 1997 Global measures of local convective instability. *Phys. Rev. Lett.* **77**, 4387–90.
- EHRENSTEIN, U. & GALLAIRE, F. 2005 On two-dimensional temporal modes in spatially evolving open flows: the flat-plate boundary layer. *J. Fluid Mech.* **536**, 209–218.
- EHRENSTEIN, U. & GALLAIRE, F. 2008 Two-dimensional global low-frequency oscillations in a separating boundary-layer flow. J. Fluid Mech. 614, 315–327.

- ELLINGSEN, T. & PALM, E. 1975 Stability of linear flow. Phys. Fluids 18, 487-488.
- Gallaire, F., Marquillie, M. & Ehrenstein, U. 2007 Three-dimensional transverse instabilities in detached boundary layers. *J. Fluid Mech.* **571**, 221–233.
- Gaster, M. 1975 A theoretical model of a wave packet in a boundary layer over a flat plate. *Proc. R. Soc. London, Ser. A* **347**, 271–289.
- GASTER, M. & GRANT, I. 1975 An experimental investigation of the formation and development of a wave packet in a laminar boundary layer. Proc. R. Soc. London, Ser. A 347, 253–269.
- JOVANOVIC, M. R. & BAMIEH, B. 2005 Componentwise energy amplification in channel flows. J. Fluid Mech. 534, 145–183.
- KOCH, W. 2002 On the spatio-temporal stability of primary and secondary crossflow vortices in a three-dimensional boundary layer. J. Fluid Mech. 456, 85–111.
- Kreiss, G., Lundbladh, A. & Henningson, D. S. 1994 Bounds for treshold amplitudes in subcritical shear flows. *J. Fluid Mech.* **270**, 175–198.
- Landahl, M. T. 1980 A note on an algebraic instability of inviscid parallel shear flows. J. Fluid Mech. 98, 1–34.
- Lehoucq, R. B., Sorensen, D. & Yang, C. 1997 Arpack users' guide: Solution of large scale eigenvalue problems with implicitly restarted Arnoldi methods. Technical Report from http://www.caam.rice.edu/software/ARPACK/, Computational and Applied Mathematics, Rice University, October 1997.
- Levin, O. & Henningson, D. S. 2003 Exponential vs algebraic growth and transition prediction in boundary layer flow. *Flow, Turbulence and Combustion* **70**, 183–210.
- Luchini, P. 2000 Reynolds-number-independent instability of the boundary layer over a flat surface: Optimal perturbations. *J. Fluid Mech.* **404**, 289–309.
- Lundell, F. & Alfredsson, P. H. 2004 Streamwise scaling of streaks in laminar boundary layers subjected to free-stream turbulence. *Phys. of Fluids* **16** (5), 1814–1817.
- MAMUN, CHOWDHURY K. & TUCKERMAN, LAURETTE S. 1995 Asymmetry and hopf bifurcation in spherical couette flow. *Phys. Fluids* 7 (1), 80–91.
- MARCUS, P. S. & TUCKERMAN, L. S. 1987a Simulation of flow between concentric rotating spheres. part 1. stready states. *J. Fluid Mech.* 185, 1–30.
- MARCUS, P. S. & TUCKERMAN, L. S. 1987b Simulation of flow between concentric rotating spheres. part 2. transitions. J. Fluid Mech. 185, 31–65.
- MARQUET, O., LOMBARDI, M., CHOMAZ, J. M., SIPP, D. & JACQUIN, L. 2009 Direct and adjoint global modes of a recirculation bubble: lift-up and convective non-normalities. *J. Fluid Mech.* **622**, 1–21.
- MARQUET, O., SIPP, D., CHOMAZ, J. M. & JACQUIN, L. 2008 Amplifier and resonator dynamics of a low-reynolds-number recirculation bubble in a global framework. *J. Fluid Mech.* **605**, 429–443.
- NAYAR, M. & ORTEGA, U. 1993 Computation of selected eigenvalues of generalized eigenvalue problems. J. Comput. Phys. 108, 8–14.
- NORDSTRÖM, J., NORDIN, N. & HENNINGSON, D. S. 1999 The fringe region technique and the Fourier method used in the direct numerical simulation of spatially evolving viscous flows. SIAM J. Sci. Comp. 20, 1365–1393.
- ORR, W. M. F. 1907 The stability or instability of the steady motions of a perfect

- liquid and of a viscous liquid. Part I: A perfect liquid. Part II: A viscous liquid. *Proc. R. Irish Acad. A* **27**, 9–138.
- REDDY, S. C. & HENNINGSON, D. S. 1993 Energy growth in viscous channel flows. J. Fluid Mech. 252, 209–238.
- Schmid, P. J. & Henningson, D. S. 2001 Stability and transition in shear flows. Springer.
- TREFETHEN, L. N., TREFETHEN, A. E., REDDY, S. C. & DRISCOLL, T. A. 1993 Hydrodynamic stability without eigenvalues. *Science* **261**, 578–584.
- Trefethen, N. & Embree, M. 2005 Spectra and Pseudospectra; The Behaviour of nonnormal matrices and operators. Princeton University Press,.
- Tuckerman, L.S & Barkley, D. 2000 Bifurcation Analysis For Timesteppers, pp. 453–566. Numerical Methods for Bifurcation Problems and Large-Scale Dynamical Systems . Springer, New York.

2

Optimal disturbances above and upstream a flat plate with an elliptic leading edge

By Antonios Monokrousos, Luca Brandt , Catherine Mavriplis and Dan S. Henningson †

[†]Linné Flow Centre, SeRC, KTH Mechanics, Stockholm, Sweden *Department of Mechanical Engineering, University of Ottawa, Ottawa, Canada

Technical report, 2011

Adjoint-based iterative methods are employed in order to compute linear optimal disturbances in a spatially growing boundary layer around an elliptic leading edge. The Lagrangian approach is used where an objective function is chosen and constraints are assigned. The optimisation problem is solved using power iterations combined with a matrix-free formulation, where the state is marched forward in time with a standard DNS solver and backward with the adjoint solver until a chosen convergence criterion is fulfilled. We consider the global and the upstream localised optimal initial condition leading to the largest possible energy amplification at time T. We found that the twodimensional initial condition with the largest potential for growth is a Tolmien-Schlichting-like wave packet that includes the Orr mechanism and is located inside the boundary layer, downstream of the leading edge. Three-dimensional disturbances induce streaks by the lift-up mechanism. Localised optimal initial condition enables us to better study the effects of the leading edge; with this approach we propose a new method to study receptivity. Two-dimensional upstream disturbances, are inefficient at triggering an unstable eigenmode. The three-dimensional disturbances instead induce elongated streamwise streaks; both the global and upstream localised disturbances give significant growth. This advocates for high receptivity to three-dimensional disturbances.

1. Introduction

The flat plate boundary layer has been a test-bed for various approaches when studying hydrodynamic stability. Its relevance arises from the fact that, even if is a fairly simple flow, it contains features of many external flows; thus it is good model for them. In stability studies further simplified versions of the general case are often used with approximations like the locally-parallel assumption with a Fourier decomposition in the streamwise direction (Butler & Farrell 1992; Reddy & Henningson 1993) or slowly varying flow, with parabolized

¹luca@mech.kth.se

equations (Andersson et al. 1999; Luchini 2000; Levin & Henningson 2003; Tempelmann et al. 2010)). Two and three-dimensional disturbances have been studied using global modes, and offer an accurate representation of the stability of the growing boundary layer (Åkervik et al. 2008). However the effect of the leading edge has not been considered so far.

Recently, with the development of the time-stepper technique, it has become possible to tackle more complicated flow cases with two and three-dimensional disturbances. Essentially stability studies are possible for any type of flow case and/or geometry for which a direct numerical simulation is feasible. The only requirement is a numerical solver of the time-dependent linearised Navier-Stokes equations and the corresponding adjoint problem. This the approach first adopted by Tuckerman & Barkley (2000) and later by Barkley et al. (2008), Blackburn et al. (2008) and Theofilis (2011) to cite a few names.

This project is an extension to previous work by Monokrousos et al. (2010) where optimal disturbances were computed for the case of the flat plate boundary layer. Here we take a step further and include the leading edge of the plate while we still retain a fairly high Reynolds number where typically transitional or even turbulent flow is observed. In particular we focus on the effect of the leading edge, how it can change the optimal disturbances and how the boundary layer can be optimally excited by disturbances coming from the outside.

The flow case, for the chosen parameters is classified as noise amplifier, in contrast to an oscillator. It is characterised by convectively instabilities when studied with the local approach. From the global point of view the flow is asymptotically stable to linear disturbances. Hence it is more relevant to look at the transient growth problem or non-modal analysis.

2. Formulation

The equations to be solved are the linearised Navier-Stokes in the incompressible regime:

$$\partial_t \mathbf{u} + (\mathbf{U} \cdot \nabla) \mathbf{u} + (\mathbf{u} \cdot \nabla) \mathbf{U} = -\nabla p + Re^{-1} \Delta \mathbf{u} + \mathbf{g}, \qquad (1)$$
$$\nabla \cdot \mathbf{u} = 0.$$

The Lagrangian approach is used where an objective function is chosen and constraints are assigned. We are looking for stationary points of the Lagrange functional with respect to the different design variables where optimality is fulfilled. The method is equivalent to finding the leading eigenpair of composite direct and adjoint Navier-Stokes evolution operator. The quantity we choose to maximise, *i.e.* the objective function, is the disturbance kinetic energy at the final time

$$\mathcal{J}(\mathbf{u}) = (\mathbf{u}(T), \mathbf{u}(T)). \tag{2}$$

The chosen constrains are the demand for \mathbf{u} to satisfy the linearised Navies-Stokes and, since we work in the linear framework, we force our initial condition

to unit energy. Hence the Lagrangian functional is written as:

$$\mathcal{L}(\mathbf{u}, \mathbf{u}^*, \gamma) = \mathcal{J} - \int_0^T (\mathbf{u}^*, (\partial_t - \mathcal{A}) \mathbf{u}) dt - \gamma ((\mathbf{u}(0), \mathbf{u}(0)) - 1).$$
 (3)

To solve the optimisation problem a matrix-free method is employed, where the state is marched forward in time with a standard direct numerical solver and backward with the corresponding adjoint solver until a chosen convergence criterion is fulfilled.

The problem is initialised with a random field, usually noise. The governing equations are iterated until the action of the combined forward and backward time marching corresponds to pure stretching of the initial condition, i.e. $p_0 = \lambda q_0$, with q_0 being the initial perturbation, p_0 the final field from the adjoint solution and λ a scalar. At convergence q_0 is the optimal disturbance and also an eigenvector of the operator $\mathcal{H}^{\dagger}\mathcal{H}$ where \mathcal{H} corresponds to the direct operator and \mathcal{H}^{\dagger} to the adjoint: $\mathcal{H}^{\dagger}\mathcal{H}q_0 = \lambda q_0$. The action of \mathcal{H} therefore amounts to integrating the linearised Navier-Stokes equations to final time T, where T becomes a parameter of the optimisation.

A similar procedure is applied to find the optimal initial condition localised upstream of the leading edge that undergoes the largest possible amplification as it travels downstream, penetrating the boundary layer. With this approach, we propose a systematic and direct method to compute the receptivity of the boundary layer to external disturbances as the computed optimal modes can be used as a projection basis to quantify the ability of incoming free-stream disturbances to initiate perturbations in the boundary layer. The formulation for localised optimal disturbances was first developed by Monokrousos $et\ al.\ (2010)$. The optimisation problem is slightly different from the one described above. The new Lagrangian reads

$$\mathcal{L}(\mathbf{u}, \mathbf{u}^*, \gamma) = (\mathbf{u}(T), \mathbf{u}(T)) - \int_0^T (\mathbf{u}^*, (\partial_t - \mathcal{A}) \mathbf{u}) dt$$
$$-\gamma ((\mathbf{u}(0), \mathbf{u}(0))_{\Lambda} - 1) - (\psi, \nabla \cdot \mathbf{u}(0))_{\Lambda}$$
(4)

where the initial condition must exist only inside the sub-domain Λ . Additionally the optimal perturbation must be divergence-free. The inner product defined by $(\cdot, \cdot)_{\Lambda}$ corresponds to an integral in Λ . For the full derivation we refer to Monokrousos *et al.* (2010).

3. Numerical approach

3.1. Numerical code

The governing equations are solved with the spectral element code Nek5000, developed by Tufo & Fischer (2001). The equations are solved by a weighted residual spectral element method (Patera 1984), which allows multi-domain decomposition while preserving high order accuracy. Inside each sub-domain,

refereed to as spectral element, the fields are represented by a spectral decomposition to Legendre polynomials and the grid points follow the Gauss-Lobatto Legendre distribution. For further details see Fischer *et al.* (2008).

The optimisation problem for the optimal initial condition is validated against previous results from Monokrousos $et\ al.\ (2010).$

3.2. Flow case

We consider a flow around a flat plate with an elliptic leading edge. The leading edge is a modified super-ellipse:

$$\left(\frac{y}{b}\right)^2 = 1 - \left(\frac{a-x}{a}\right)^p \text{ where } p = 2 + \left(\frac{x}{a}\right)^2.$$
 (5)

that has zero curvature at the juncture with the flat section so that no disturbances are introduced by the plate itself. The ratio $\frac{a}{b}$ defines the bluntness and is chosen here $\frac{a}{b}=6$ which corresponds to a relatively blunt shape, Schrader et al. (2010). The Reynolds number of the flow is $Re=\frac{bU}{\nu}$ based on the half thickness of the plate (b), the free-stream velocity (U) and the kinematic viscosity of the fluid (ν) . Most of the results presented correspond to Reynolds number Re=3000. We also include few results for a case of lower Reynolds number, Re=1000. In some cases we also provide the Reynolds number based on the distance from the leading edge $Re_x=\frac{xU}{\nu}$ where x is the distance from the leading edge.

In figure 1a) and 1b) the two velocity components of the base flow are shown. Since the flow is globally stable, the base flow is computed marching in time the full non-linear Navier-Stokes equations until a steady state is obtained. The boundary conditions are computed by solving the Euler equations in a domain much larger than our computational domain. A strong deceleration of the flow is observed near the stagnation point, immediately downstream a strong vertical velocity component. Further downstream a thin boundary layer is developing. The computational box extends downstream up to 100-200 units (plate half-with b) depending on the case. For a validation of the base flow see Schrader $et\ al.\ (2010)$.

3.3. Resolution

Since we are using the spectral element method, we decompose our domain in several, relatively large elements. In particular, we used polynomial order 10, which implies 100 points per element for the 2D case and 1000 for the 3D. The total number of elements depends on the length of the box. We run the 2D cases in a longer box (in order to be able to observe an unstable wave packet) using 3040 elements, 19 in the direction normal to the plate and 160 along the plate. The total number of points is 304000. In the 3D cases the computational box was typically shorter and thus we used 124 elements in the streamwise direction. However we needed 3 elements in the spanwise direction to resolve the modulation of the Fourier modes and this gives a total number of

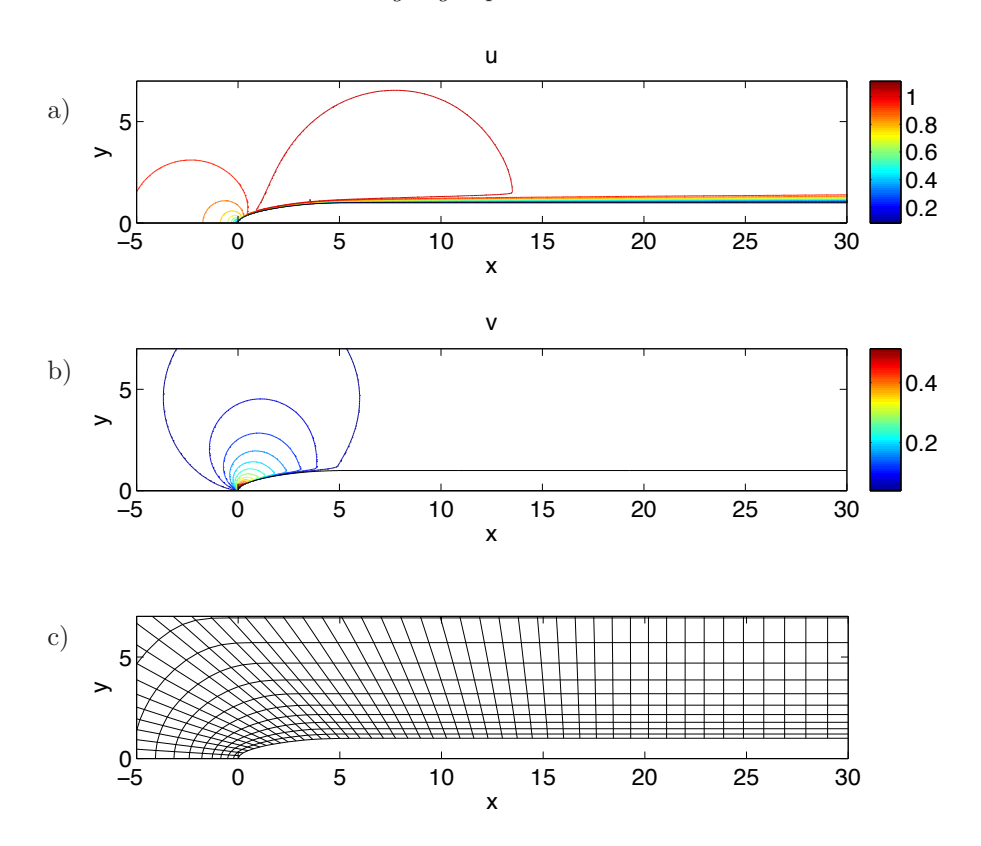


FIGURE 1. Contours of the streamwise (a) and wall-normal (b) velocity components of the base flow for Re=3000. The plot has equal scaling in the two directions. c) Element grid (without the Gauss-Lobatto Legendre points)

elements of 7068. For 3D elements the total number of points is thus 7068000. In both cases we cluster the elements both in the wall-normal direction near the wall and along the plate near the area of the leading edge. A section of the computational grid located around the leading edge is shown in figure 1c).

4. Results

We investigate the disturbances that give the largest transient energy growth. In order to determine the structure in question we loop over different optimisation times. Additionally since the base flow is homogeneous in the spanwise direction, disturbances of different spanwise periodicity are considered separately. Owing to the cost of each optimisation loop, relatively few cases are considered. However, we are confident that the optimal structures are captured and the essential physical mechanisms are included.

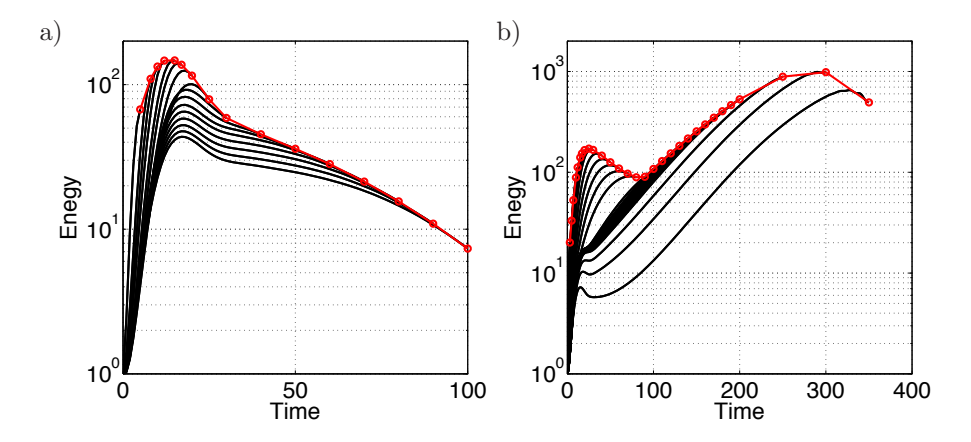


FIGURE 2. Disturbance energy vs optimisation times for Re = 1000 (a) and Re = 3000 (b) and 2D disturbances.

4.1. Optimal initial conditions

First we consider optimal initial condition where no assumptions are made about the location. Two and three dimensional cases are studied.

4.1.1. Two-dimensional optimal initial conditions

Two different cases are investigated for the two-dimensional disturbances, one that corresponding to high (Re = 3000) and low (Re = 1000) Reynolds number.

In figure 2 the disturbance energy growth is shown for the two cases for various optimisation times. The red line is the energy envelope. Figure 2a) shows results for low Reynolds number (Re = 1000) where the boundary layer is locally stable all the way down to the outflow. Here the Reynolds number based on the distance to the leading edge is $Re_x = 10^5$. Hence the only way to have energy growth is through the Orr-mechanism. Anything that acts on a longer time scale will only give energy decay.

Figure 2b) reports results for the higher Reynolds number (Re=3000). In this case we observe that locally unstable Tolmien-Schlichting (TS) wave packets are generated and amplify exponentially as they are convected downstream. The maximum time for energy growth is here governed by the downstream extension of the computational box; indeed a longer box would allow longer optimisation times and more space for the exponential instability to grow. Additionally, we note a local maximum for short optimisation times which corresponds again to a pure Orr-mechanism which is active on small time scales. The energy decay seen for large optimisation time is due to the fact that these disturbances gradually exit our computational domain and thus their measurable energy decay.

In figure 3 the spatial structures of the optimal disturbances are shown for the two Reynolds numbers where the optimal times are $T=12\ (Re=1000)$ and

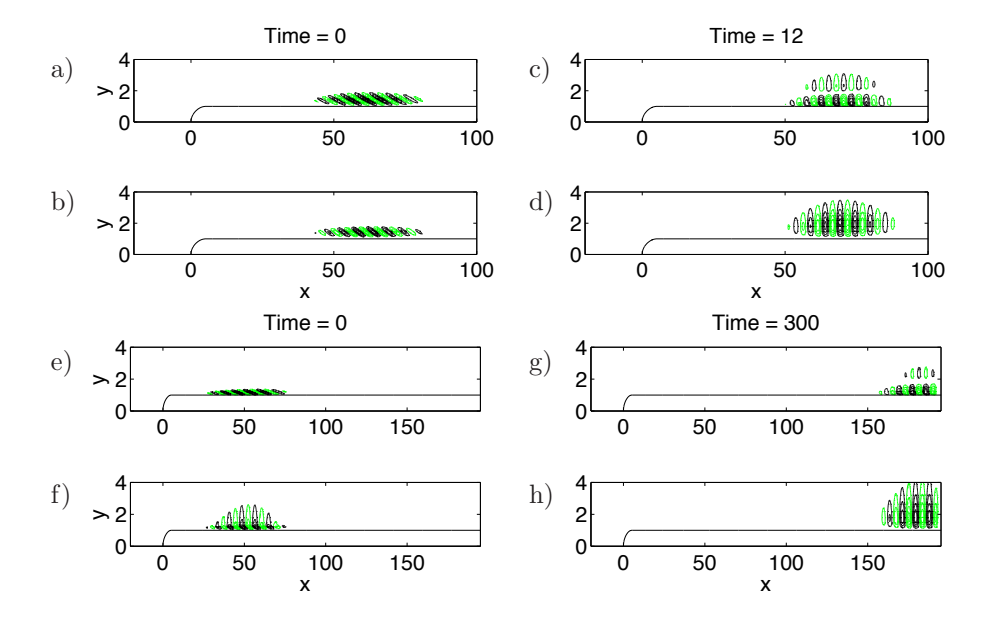


FIGURE 3. Spatial structures for optimal initial condition and the corresponding responses. Re=1000, initial condition: a) streamwise component, b) wall-normal component; response: c) streamwise component, d) wall-normal component. Re=3000, initial condition: e) streamwise component, f) wall-normal component; response: g) streamwise component, h) wall-normal component.

T=300~(Re=3000). The structures look rather similar, Orr-structures generating wave-packets, in both cases (also seen by Monokrousos et~al.~(2010) and Åkervik et~al.~(2008)). However, in the low-Reynolds number case, the energy of the wave-packet decays after the initial increase. Additionally the disturbance is initiated further downstream (relative to the high-Reynolds number case) close to the outflow, exploiting the higher Reynolds number.

4.1.2. Three-dimensional optimal initial conditions

Considering three dimensional disturbances, one additional parameter enters the problem, namely the spanwise wavenumber β . To determine the optimal β we need to loop over an additional parameter, as we do for the optimisation time. This leads to a two-dimensional parameter space we need to explore.

In figure (4) we plot iso-contours of energy growth for different optimisation times T and spanwise wavenumbers β . We see a clear peak at T=90 and $\beta=2.0$. To understand the physical mechanisms behind it we consider the spatial distribution of the disturbance velocities. The three components of the optimal initial condition are shown in figure 5a) and the corresponding response

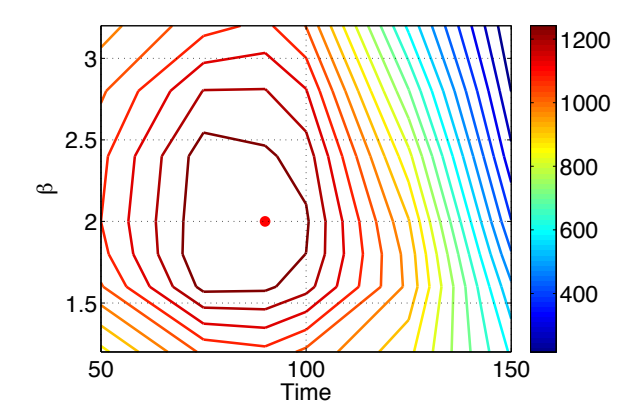


FIGURE 4. Contours of energy gain for different final times and spanwise wavenumbers. The Reynolds number is Re = 3000.

	Initial disturbance	Response
Streamwise	6.3 %	91.3%
Wall-normal	28.6%	1.8 %
Spanwise	65.1%	6.9%

Table 1. The table shows the component-wise energy content of each component for the initial and final condition. The energy growth was $G = 1.3 \cdot 10^3$

in 5b) while the component-wise energy content is shown in table 1. The time evolution of the three components of the disturbance energy of the perturbation is shown in figure 6.

In table 1 we can see the strong component-wise energy transfer which implies that the lift-up mechanism is active: streamwise vortices induce streamwise streaks inside the boundary layer. Similar results were obtained by Andersson $et\ al.\ (1999)$ using the boundary layer equations and by Monokrousos $et\ al.\ (2010)$ in the global framework without the leading edge. The flow structures are plotted in figure 5b). Additionally we can see that the Orr-mechanism with the characteristic upstream leaning structures contribute to some energy gain.

For longer optimisation times a rapid decay of the amplification is observed due to the limited box size, as seen in figure (4). As we increase the optimisation time, the disturbance is forced to move upstream in order to avoid leaving the domain within that time and at some point it goes upstream from the plate, towards the area of the flow where there is not shear. On the other hand for short times, the lift-up mechanism does not have enough time to fully exploit the shear of the boundary layer.

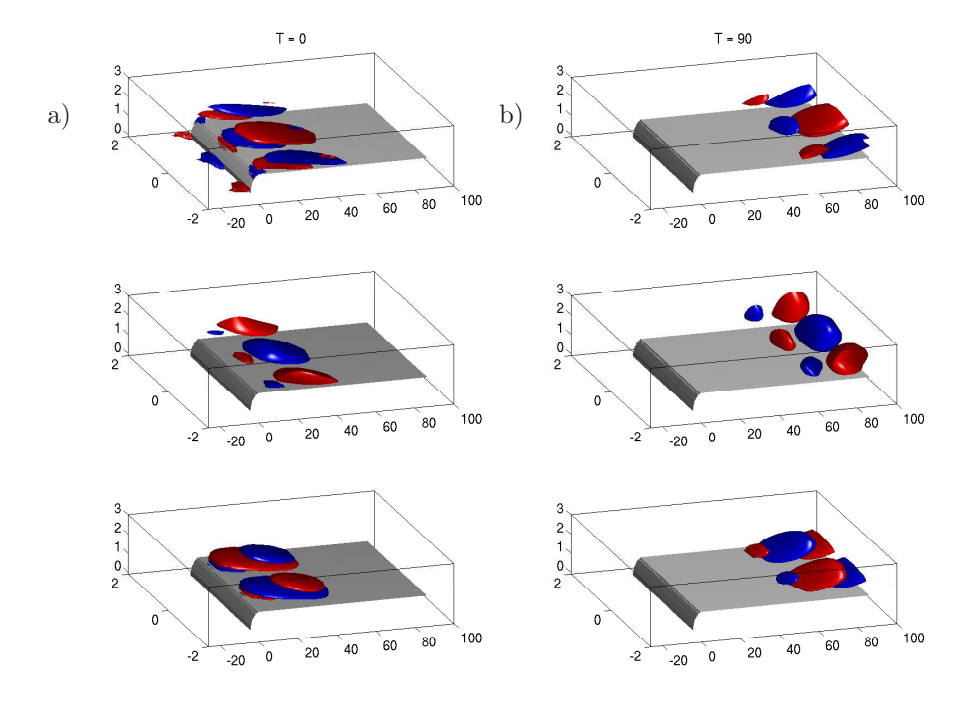


FIGURE 5. Optimal initial condition (a) and the corresponding flow response (b). Streamwise, wall-normal and spanwise velocities are shown from the top to bottom. The energy growth is $G=1.3\cdot 10^3$, the Reynolds number, Re=3000. The Reynolds number at the outflow based on the distance from the leading edge is $Re_x=300000$.

As mentioned above the reported Reynolds number is defined using the free-stream velocity, the half-width of the plate and the fluid viscosity. This implies that all lengths and wavenumbers are scaled with the half-width of the plate. In order to compare with the results from previous studies like Monokrousos et al. (2010), where the wavenumber is scaled with the displacement thickness, the length is multiplied with the ratio of the two Reynolds numbers since the free-stream velocity and the viscosity are equal in both cases. In those units the optimal wavenumber is $\beta^* = 0.67$ which is comparable to the value retrieved by Monokrousos et al. (2010) ($\beta^* = 0.55$). We should also mention that a variation is to be expected due to the inclusion of the leading edge in the computation.

4.2. Localised optimal initial conditions

We study optimal initial conditions that are forced to be localised in space. The used method is extensively described in Monokrousos $et\ al.\ (2010)$. These

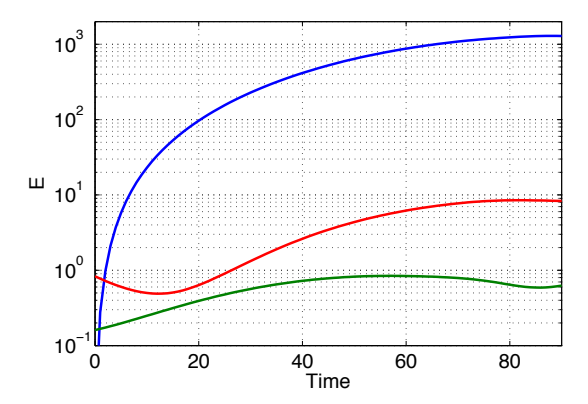


FIGURE 6. Disturbance energy versus time for the optimal initial condition. Three velocity components are shown, streamwise (blue), spanwise (red) and wall-normal (green). The Reynolds number is Re=3000. The Reynolds number as the outflow based on the distance from the leading edge is $Re_x=300000$.

type of optimals allow us to study how a disturbance optimally penetrates the boundary layer around the curved leading edge and subsequently generates a perturbation that can have a strong growth downstream inside the boundary layer.

4.2.1. Two-dimensional disturbances

First we study two-dimensional disturbances. We enforce the initial perturbations to exist in a sub-domain upstream from the leading edge, and thereafter the optimisation procedure gives the optimal spatial distribution inside the sub-domain. In this way we can specifically study the receptivity features. The results we obtained for this case were much in line with Schrader et al. (2010). The upstream-localised disturbances are proven to be rather inefficient in penetrating the boundary layer. They loose a lot of energy during the initial phase and furthermore, the disturbance generated inside the boundary layer consists of a wavepacket characterised by a relatively high streamwise wavenumber larger than that corresponding to the unstable TS-wave. Consequently the exponential instability is not efficiently initiated resulting a weak growth in the process.

It appears that the optimisation procedure favours a stable wave-packet over the unstable since it probably has better penetration properties (for this bluntness). In other words, waves of spatial scale of the unstable modes penetrate inefficiently the boundary layer.

To enhance the growth of the wave-packet we would need a much longer computational domain with sufficient space for it to grow exponentially but this would render this computation very expensive.

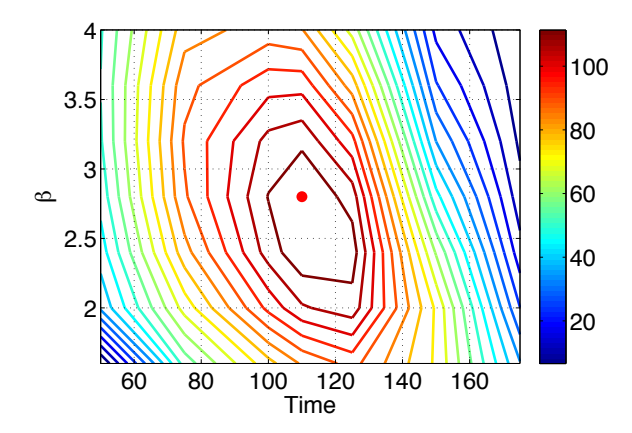


FIGURE 7. Contours of energy gain for different final times and spanwise wavenumbers (localised initial condition). The Reynolds number is Re = 3000.

4.2.2. Three-dimensional disturbances

As before, we perform a parametric study to find the optimal time and spanwise wavenumber β . In figure (4) iso-contours of energy growth for different optimisation times and spanwise wavenumbers are shown for the case of the upstream localised disturbance. The red dot corresponds to the maximum. The optimal disturbance occurs for T=125 and $\beta=2.8$. Comparing the values to the non-localised optimal we see two main differences. First the optimisation time is longer and also β is higher. The increased time was expected since the perturbation spends some time upstream from the leading edge and during the penetration phase.

We have seen already that the receptivity to purely two-dimensional disturbances is very weak. That can possibly explain why the optimal β is increased for the upstream localised case, it may become less optimal with respect to the lift-up mechanism but at the same time is less damped by the presence of the leading edge. The two trends seem to balance at $\beta = 2.8$ ($\beta^* = 0.93$).

The physical mechanisms pertaining the energy growth appear to be the same with the exception that the Orr-mechanism is not present. This is attributed to the fact that there is no shear where the perturbation is initiated hence no energy can be gained from an upstream leaning structure.

The spatial distribution of the upstream localised optimal initial condition is shown in figure 8a) and the corresponding response in 8b); in figure 9 we plot the full time evolution of the three components of the energy of the perturbation. We can see that most of the energy of the perturbation lays on the plane normal to the streamwise direction and also the streamwise structure is almost constant implying streamwise vortices that generate streaks inside the boundary layer.

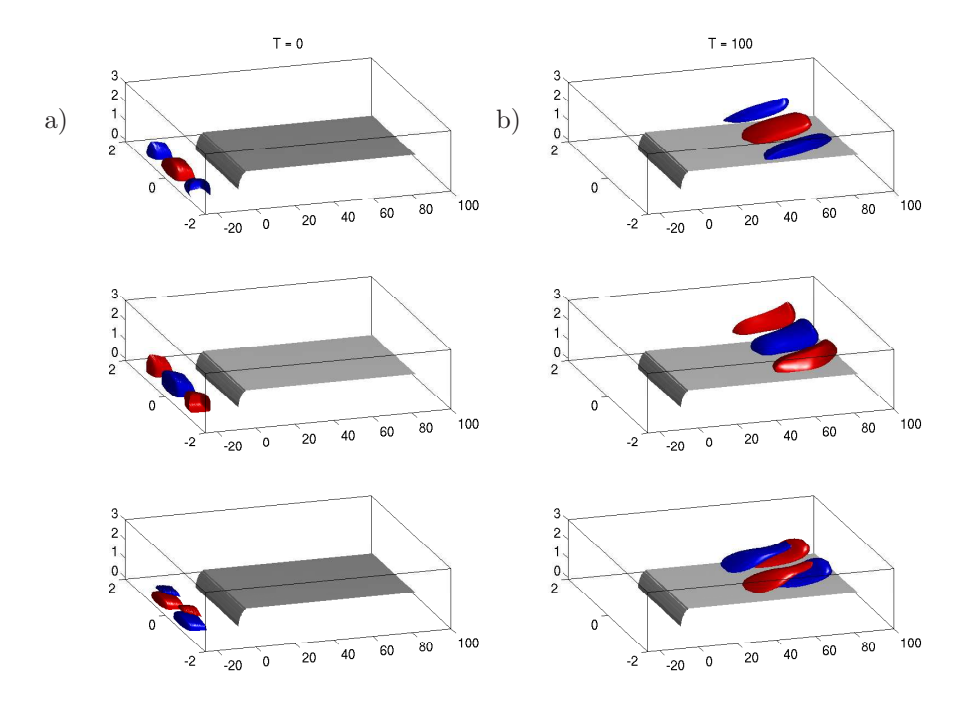


FIGURE 8. Localised optimal initial condition (a) and the corresponding flow response (b). The three components are shown in the vertical order streamwise, wall-normal and spanwise. The energy growth was $G = 1.2 \cdot 10^2$. The Reynolds number is Re = 3000. The Reynolds number as the outflow based on the distance from the leading edge is $Re_x = 300000$.

	Initial disturbance	Response
Streamwise	17.7 %	93.6%
Wall-normal	36.7%	1.8 %
Spanwise	45.6%	4.6%

Table 2. The table shows the component-wise energy content of each component for the initial and final condition. The energy growth was $G=1.2\cdot 10^2$

We note that as the vortices convect downstream in front of the leading edge slowly decay without much happening in the dynamics, similar to what is observed in decaying turbulence. However once they reach the area with strong shear, near the stagnation point $(T\approx 20)$, they quickly start to transform energy from the streamwise vortices to the streamwise streaks and through the lift-up effect to extract energy from the mean shear. It is thus important

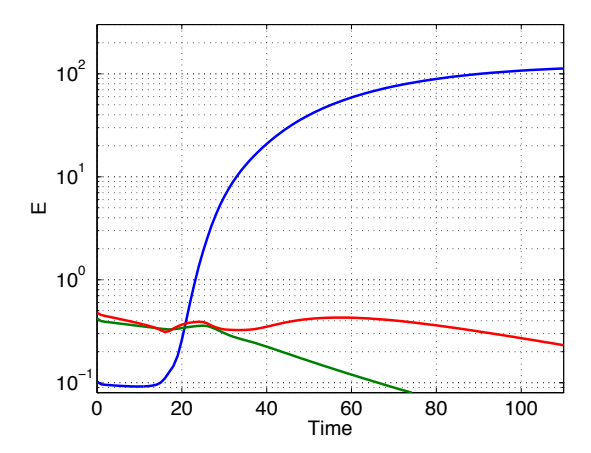


FIGURE 9. Disturbance energy versus time for the optimal localised initial condition. Three velocity components are shown, streamwise (blue), spanwise (red) and wall-normal (green). The Reynolds number is Re=3000. The Reynolds number as the outflow based on the distance from the leading edge is $Re_x=300000$.

to include the leading-edge effect in receptivity. The total energy growth is substantially weaker relative to the non-localised optimals. This can be attributed to a few reasons. In this case the Orr-mechanisms can not contribute and secondarily the lift-up effect is happening further upstream relative to the non-localised case which corresponds to lower Reynolds number and thus lower transient growth potential, see Andersson et al. (1999).

5. Conclusions

We have applied a Lagrange multiplier technique using the direct and adjoint linearised Navier-Stokes equations in order to quantify the disturbance growth potential in a flow around a flat plate with an elliptic leading edge at moderately high Reynolds. We consider the optimal initial condition leading to the largest possible energy amplification at time T. Additionally we compute the localised optimal disturbance upstream from the leading edge. This method can be used to create modal basis and project free-stream disturbances i.e. a direct method for computing receptivity coefficients for externally excited flows. The optimisation framework adopted does not restrict us to assume slow variation of the base flow in the streamwise direction, common to both the first order approximation of the Orr-Sommerfeld-Squire formulation and the more advanced Parabolized Stability Equations approximation; moreover, it allows us to include curved geometries and fully three dimensional configurations.

We found that the two-dimensional initial condition with the largest potential for growth is a TS-like wave packet that includes the Orr mechanism in

their initial phase and is located inside the boundary layer, downstream from the leading edge. Its growth is linked to the exponentially unstable eigenmodes of the Blasius boundary layer and it is limited by the streamwise extent of the computational box. The three dimensional case shows a peak in the energy much earlier in time (and space) for spanwise wavenumber $\beta=2.0$, relevant to the well understood lift-up mechanism. This number is in close agreement with earlier studies of similar nature.

The localised optimal initial conditions are more interesting since they allow for better understanding of the effects of the leading edge and its receptivity properties. Disturbances are placed upstream in the free-stream. We found that the two-dimensional upstream disturbances are rather inefficient at triggering an unstable wave-packet which can exploit the convective instability of the boundary layer. The flow around the leading edge has a strong effect on these type of disturbances, *i.e.* it has a strong damping effect and the later evolution of the disturbance is dominated by this effect. In particular a stable wave-packet is generated and its energy just decays as it propagates downstream inside the boundary layer. This indicates that an unstable wave-packet would be so strongly damped by the leading edge flow that is never favoured by the optimisation.

The three-dimensional disturbances though are exploiting the lift up mechanism very efficiently at a very early stage. The generated streaks are located further from the wall than the TS-wave and thus do not suffer from the loss of energy due to diffusion close to the wall. Additionally their streamwise wavenumber is very low and does not seem to be heavily affected by the low local Reynolds number in the area. This mechanism is proven to be very robust.

6. Acknowledgements

The authors wish to thank Dr. Lars-Uve Schrader for providing the mesh generator and for many fruitful discussions. Computer time provided by SNIC (Swedish National Infrastructure for Computing) is gratefully acknowledged. The present work is supported by the Swedish Research Council (VR) which is gratefully acknowledged.

References

- ÅKERVIK, E., EHRENSTEIN, U., GALLAIRE, F. & HENNINGSON, D. S. 2008 Global two-dimensional stability measures of the flat plate boundary-layer flow. *Eur. J. Mech. B/Fluids* **27**, 501–513.
- Andersson, P., Berggren, M. & Henningson, D. S. 1999 Optimal disturbances and bypass transition in boundary layers. *Phys. Fluids* 11, 134–150.
- Barkley, D., Blackburn, H. M. & Sherwin, S. J. 2008 Direct optimal growth analysis for timesteppers. *Itn. J. Numer. Meth. Fluids* **57**, 1435–1458.
- Blackburn, H. M., Barkley, D. & Sherwin, S. J. 2008 Convective instability and transient growth in flow over a backward-facing step. *J. Fluid Mech.* **608**, 271–304.
- Butler, K. M. & Farrell, B. F. 1992 Three-dimensional optimal perturbations in viscous shear flow. *Phys. Fluids A* 4, 1637–1650.
- FISCHER, P.F., LOTTES, J.W. & KERKEMEIER, S.G. 2008 nek5000 Web page. Http://nek5000.mcs.anl.gov.
- Levin, O. & Henningson, D. S. 2003 Exponential vs algebraic growth and transition prediction in boundary layer flow. *Flow, Turbulence and Combustion* **70**, 183–210.
- Luchini, P. 2000 Reynolds-number-independent instability of the boundary layer over a flat surface: Optimal perturbations. *J. Fluid Mech.* **404**, 289–309.
- Monokrousos, A., Åkervik, E. & Henningson, L. Brandt D.S. 2010 Global three-dimentional optimal disturbances in the blasius boundary-layer flow using time-steppers. *J. Fluid Mech.* **650**, 181–214.
- Patera, Anthony T 1984 A spectral element method for fluid dynamics: Laminar flow in a channel expansion. *Journal of Computational Physics* **54** (3), 468 488.
- Reddy, S. C. & Henningson, D. S. 1993 Energy growth in viscous channel flows. J. Fluid Mech. 252, 209–238.
- Schrader, L.-U., Brandt, L., Mavriplis, C. & Henningson, D. S. 2010 Receptivity to free-stream vorticity of flow past a flat plate with elliptic leading edge. *Journal of Fluid Mechanics* 653 (-1), 245–271.
- Tempelmann, D., Hanifi, A. & Henningson, D.S. 2010 Spatial optimal growth in three-dimensional boundary layers. *Journal of Fluid Mechanics* **646**, 5–37.
- Theofilis, V. 2011 Global linear instability. Annual Review of Fluid Mechanics 43 (1), 319–352.
- Tuckerman, L.S & Barkley, D. 2000 Bifurcation Analysis For Timesteppers, pp. 453–566. Numerical Methods for Bifurcation Problems and Large-Scale Dynamical Systems . Springer, New York.
- Tufo, H.M. & Fischer, P.F 2001 Fast parallel direct solvers for coarse grid problems. *Par. & Dist. Computing* **61(2)**, 151–177.

3

Non-equilibrium thermodynamics and the optimal path to turbulence in shear flows

By Antonios Monokrousos^{1*}, Alessandro Bottaro², Luca Brandt¹, Andrea Di Vita² and Dan S. Henningson¹

Physical Review Letters, 106, 134502, 2011

We determine the initial condition on the laminar/turbulent boundary closest to the laminar state using nonlinear optimization for plane Couette flow. Resorting to the general evolution criterion of non-equilibrium systems we optimize the route to the statistically steady turbulent state, i.e. the state characterized by the largest entropy production. This is the first time information from the fully turbulent state is included in the optimization procedure. We demonstrate that the optimal initial condition is localized in space for realistic flow domains.

The transition from laminar to turbulent flow is still a challenging problem despite the fact that our understanding has increased significantly in the last years Hof et al. (2004); Eckhardt (2007); Mullin (2011). In canonical shear flows (pipe, channel and Couette flows) transition is typically subcritical and initial perturbations of finite amplitudes are necessary.

This paper is about the computation and nature of the smallest disturbances that most quickly trigger turbulence in linearly stable shear flows. This is relevant both for our understanding of the flow physics as well as to design effective control strategies Kawahara (2005). To do this, we optimize the trajectory of the system with respect to the *General Evolution Criterion* Glansdorff & Prigogine (1964) of non-equilibrium thermodynamics. The criterion has been used successfully in a wide range of applications, shock-waves Rebhan (1990), biology Juretic & Zupanovic (2003), climate research Paltridge (1979); Ozawa et al. (2003) and nuclear fusion DiVita & Brusati (1995), although never, thus far, in the search for optimal turbulence-triggering disturbances.

Recent progress in the understanding of subcritical transition to turbulence in shear flows was made using the nonlinear concept of *edge state*, originating from dynamical systems' theory. Edge state refers to the flow regime reached asymptotically by phase-space trajectories visiting neither the turbulent nor the laminar state. It is an unstable flow state, yet embedded exact coherent states have been identified numerically: steady states, traveling waves and periodic

¹ Linné Flow Centre, SeRC, KTH Mechanics, SE-100 44 Stockholm, Sweden
² DICAT, Università di Genova, Via Montallegro 1, 16145 Genova, Italy

orbits (see Hof et al. (2004); Eckhardt (2007); Mullin (2011) and references therein).

Here, we wish to determine the most dangerous perturbation leading to the turbulent state. Two concepts are key to our analysis: i) optimal initial condition and ii) the target final state of the flow. Optimally growing perturbations (in energy norm) have been considered extensively within the linear framework Schmid & Henningson (2001). This non-modal approach has been able to explain the physical mechanisms responsible for energy growth in shear flows and, together with weakly nonlinear models such as secondary instability analysis, contributed to drawing a plausible picture of the early stages of the transition process. However, the later stages are inherently non-linear and linear theory fails. Nonlinear optimization in reduced-order subspaces has been presented before Reddy & Henningson (1993); Viswanath & Cvitanovic (2009); Duguet et al. (2010), while only very recently researchers considered fully nonlinear optimization, without targeting the turbulent state Pringle & Kerswell (2010); Cherubini et al. (2010). In the former study Pringle & Kerswell (2010), the authors use the full Navier-Stokes equations to show how nonlinearity can change the optimal which emerges from a linear transient growth analysis in pipe flow at subcritical condition. The optimal initial condition obtained is three-dimensional and shows signs of localization. As reported in Pringle & Kerswell (2010), a more extensive optimization adopting larger flow domains would provide confirmation and formidable extension of the results in that work. Here, we take this step further and confirm the prediction that the optimal is fully localized in extended flow domains. Furthermore we include the fully turbulent state into the optimization procedure and manage to bridge the gap between the optimization initial amplitude and the actual transition threshold Pringle & Kerswell (2010).

To take this step, it is crucial to select a metric for the definition of the final flow state. Here we resort to thermodynamics considerations to select the objective of our optimization, unlike previous studies where the disturbance kinetic energy has been used. The theory is tested on the simple case of plane Couette flow, a flow stable for all values of the Reynolds $Re = \frac{Uh}{\nu}$, where $\pm U$ and h are the velocity at each wall and the channel half-width, with ν the kinematic viscosity. Time is therefore reported in units of h/U.

All shear flows by definition are not in equilibrium with their environment since there is continuous energy exchange through the walls. However, the Navier-Stokes equations can be viewed as a special case of the Boltzmann equation for systems for which the local thermodynamic equilibrium assumption is valid Di Vita (2010). Glansdorff and Prigogine Glansdorff & Prigogine (1964) demonstrated that for time invariant boundary conditions the system eventually reaches a $statistically\ steady\ state$. When dissipation is dominant (low Reynolds number) the system goes back to the laminar state, while when inertia dominates (high values of Re) the turbulent state ensues. A fully developed flow, from the stand point of thermodynamics, is a statistically steady

state. A chaotic turbulent flow is indeed characterized by steady values of time-averaged quantities, like fluctuations and dissipation. The approach of the fluid system to a statistically steady state is central to the theory presented here Malkus (1956).

The general evolution criterion implies that certain quantities obtain extreme values once the statistically steady state is reached. It has been recently demonstrated Di Vita (2010) that this leads to Malkus heuristic principle Malkus (1956): a viscous, turbulent, incompressible Couette flow in statistically steady state with assigned mean velocity maximizes the total rate of viscous dissipation. To determine the optimal initial condition leading to turbulent flow, we employ Lagrangian optimization where the functional \mathcal{L} to maximize consist of an objective function and two constraints (the Navier-Stokes equations and the energy level of the initial disturbance), i.e.

$$\mathcal{L} = \mathcal{J} - \int_0^T \left[(\mathbf{u}^*, NS(\mathbf{u}))_E + (p^*, \nabla \cdot \mathbf{u})_E \right] dt$$
$$-\lambda(\|\mathbf{u}(0) - \mathbf{U}\|_E^2 - \epsilon_0), \tag{1}$$

with the subscript E denoting the energy inner product, i.e. the integral over the whole domain. In the above, \mathbf{u}^* , p^* and λ are the Lagrange multipliers, i.e. the adjoint variables, NS the nonlinear Navier-Stokes equations, and ϵ_0 the kinetic energy of the perturbation at t=0; **u** is the velocity vector and **U** the Couette base flow. Since the system under consideration is chaotic we will maximize the average value of the functional, integrating over a sufficiently long time interval. As introduced above, the objective function is the time-averaged dissipation

$$\mathcal{J} = \frac{1}{T} \int_0^T \frac{1}{Re} \left(\nabla \mathbf{u} : \nabla \mathbf{u} \right) dt \tag{2}$$

with T the final observation time. Maximizing the time integral of the entropy production implies that we also obtain the fastest route to turbulence for any given value of the initial energy ϵ_0 . Variations of the Lagrangian provide the gradient of the objective function with respect to variation of the initial condition \mathbf{u}_0 . The gradient $\nabla_{\mathbf{u}(0)}\mathcal{L} = \mathbf{u}^*(0)$ is obtained by forward time integration of the Navier-Stokes equations and backward integration of the adjoint system, the latter containing $-1/(TRe)\nabla^2\mathbf{u}$ a source term stemming from the definition of \mathcal{J} .

This forcing term is stochastic when the flow has become turbulent. It can change significantly for very small variations of the initial conditions, as it occurs typically in chaotic flows. As a consequence, the update of the initial condition can be significant even in the proximity of an optimal. Therefore to improve convergence we include a relaxation term for each update of the initial guess

$$\mathbf{u}(0)^{n+1} = (1 - \sigma)\mathbf{u}^*(0)^n + \sigma\mathbf{u}(0)^n.$$
(3)

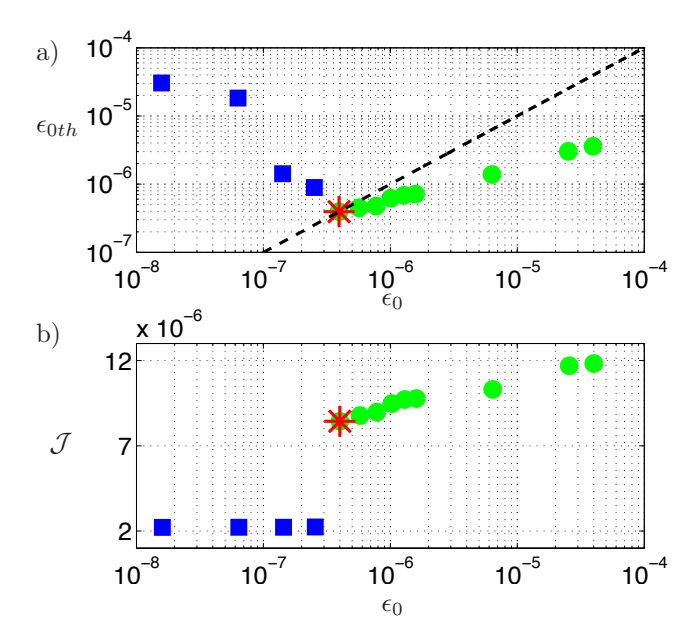


FIGURE 1. (a) Energy threshold (ϵ_{0th}) to reach a turbulent state and (b) viscous dissipation rate (objective function \mathcal{J}) versus the energy amplitude ϵ_0 used to determine the shape of the optimal initial condition. The energy for transition is computed by applying bisection to each optimal initial condition to scale its amplitude. The square blue symbols pertain to initial conditions determined with laminar flow at final time T=300. Data for Couette flow at Re=1500, domain size $4\pi \times 2 \times 2\pi$ with resolution $128 \times 73 \times 64$ grid points in the streamwise, wall-normal and spanwise direction, respectively.

Close to convergence, the relaxation term gives an ensemble average of the different initial conditions, since the values of the objective function (i.e. the statistics of the turbulent state) are basically constant. A fully converged initial condition can be obtained more easily for the smaller values of ϵ_0 considered, when the flow never becomes turbulent and just above the minimum value ϵ_{0T} of the initial energy for which a turbulence state can be established. Larger initial amplitudes yield a very noisy optimization. Indeed we first optimize for large values of the initial energy and gradually reduce the value of ϵ_0 to be sure to target the final turbulent state. Typically we perform between 50 and 100 iterations for each level of initial energy.

In figure 1 the energy threshold necessary to reach a turbulent state is displayed for each initial condition found by the optimization procedure in the largest domain considered. Each of these initial conditions is defined by the energy level ϵ_0 used in the Lagrangian \mathcal{L} (see eq.1). The threshold level is

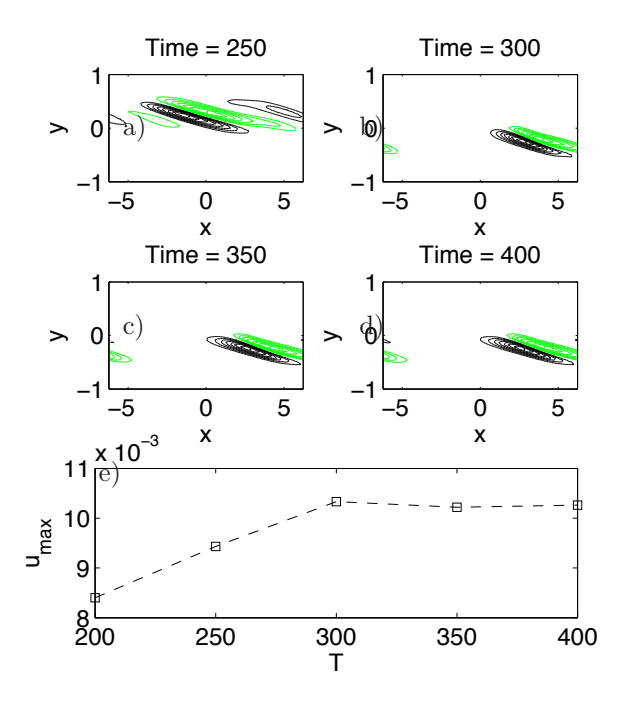


FIGURE 2. Optimal initial condition at the minimum threshold level ϵ_{0T} for different values of the final optimization time: a) T = 250, b) T = 300, c) T = 350, d) T = 400. The plot displays the streamwise velocity component in the wall-normal (x,y) plane at $z=\pi/2$. The subplot e) shows the maximum of the velocity amplitude in the whole domain versus the final optimization time T. The data pertains the largest box size considered, Re = 1500.

determined by a classic bisection procedure with an accuracy of five digits. The straight line is a guide to the eye and indicates equal values of the energy on the axis. For the largest ϵ_0 considered, one can reduce the amplitude of the initial condition and still reach the turbulent state. When decreasing the constraint on the initial energy, we reach a value, ϵ_{0T} , below which the flow remains laminar for any t < T. This is indeed the nonlinear optimal initial condition of smallest amplitude leading to a statistically steady turbulent flow.

For values of the initial energy lower than ϵ_{0T} , where turbulent flow is not reached during the optimization procedure, the initial condition must be scaled up by a factor of about 4 or 5 to trigger transition, similarly to what was obtained in Pringle & Kerswell (2010). Previous optimizations Pringle & Kerswell (2010); Cherubini et al. (2010) in fact considered highly distorted yet laminar flows (in the latter work owing to the relatively short optimization

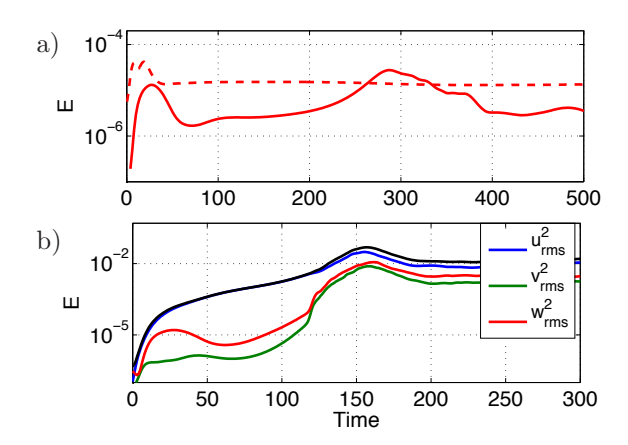


FIGURE 3. (a): The solid line shows the edge trajectory for minimum energy threshold ϵ_{0T} at Re=1500 and domain size $4\pi\times2\times2\pi$. The dashed line indicates the edge trajectory at Re=500 with domain size $2\pi\times2\times\pi$. The energy of the wall-normal velocity perturbation is displayed. (b): Evolution of the energy in time for the nonlinear optimal discussed in figure 1 for $\epsilon_0=\epsilon_{0T}$.

interval). The threshold for transition is then computed with a bisection procedure to find the laminar/turbulent boundary. The initial condition of critical energy ϵ_{0T} obtained with the present procedure is just above the boundary and its energy is lower than that obtained from nonlinear optimization of a laminar flow. In addition, having a turbulent state as final target gives a lower threshold for transition with optimals computed above ϵ_{0T} than below ϵ_{0T} . For $\epsilon_0 \to 0$ we would retrieve the linear optimals which cannot induce turbulence alone. Therefore a fully nonlinear optimization, including information from the fully turbulent state, is indeed indispensable if the target is the complete transition process. Note that we have also performed a series of simulations using the time integral of the disturbance kinetic energy as objective function. Although the results are qualitatively the same, dissipation provides a lower threshold amplitude for transition, about 5% smaller. More importantly, we obtain better convergence with dissipation as objective function; for the lowest Reynolds numbers considered we could not obtain converged results when using the disturbance kinetic energy. Note also that previous studies used the kinetic energy at final time rather than the time integral: this can explain improved convergence with our approach.

We performed optimization for a combination of 4 different values of the Reynolds numbers, Re = [500, 750, 1000, 1500], three difference box sizes, $[2\pi \times 2 \times \pi]$, $[4\pi \times 2 \times \pi]$, $[4\pi \times 2 \times 2\pi]$ and final optimization time $T \in [200, 400]$. It turned out to be more difficult to obtain converged solutions for the lowest

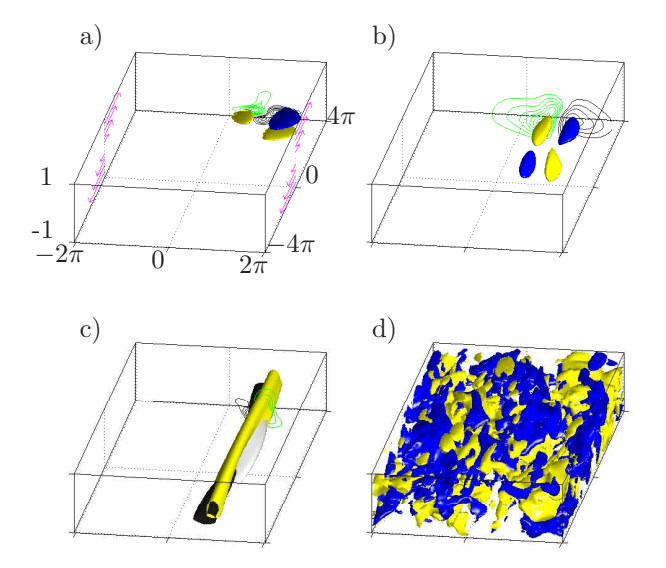


FIGURE 4. Optimal initial condition at the threshold level ϵ_{0T} , visualized through isosurfaces of positive and negative streamwise velocity perturbation, shown with pale (yellow) and dark (blue) color. Contour lines show positive and negative spanwise velocity at $x = 1.5\pi$. The base flow is indicated by the arrows along the sides in (a). Re = 1500, domain size $4\pi \times 2 \times 2\pi$. The isosurface level is 65% of the maximum value of each component: (a) $u_{max}^2=2.89\times 10^{-5}$, (b) $u_{max}^2=2.89\times 10^{-5}$, (c) $u_{max}^2=2.09\times 10^{-3}$, (d) $u_{max}^2=2.07\times 10^{-1}$.

Reynolds number considered. This is because the method relies on the concept of statistically steady state which implies a well developed turbulent field. This is not the case at lower values of the Reynolds number where turbulence has a transient nature. Furthermore, sufficient time is needed to reach a final turbulent flow. The optimal initial condition obtained with different optimization times T is displayed in figure 2. The variations are marginal for the cases considered here for final times beyond T = 300, as quantified by the maximum of the velocity amplitude in the whole domain in figure 2e). The results are therefore independent of T, the objective function has reached an asymptotic value and we have indeed optimized the route to the turbulent state.

For smaller domains and lower Reynolds number the edge trajectories visit some steady solution before the final breakdown to turbulence. This is not the case for the largest domain and higher Re considered, where a chaotic behavior is observed near the edge trajectory. Evidence for this is provided in figure 3(a) where the evolution of the rms values of the wall-normal velocity perturbation is displayed for two cases.

The optimal trajectory to the turbulent state is visualized in physical space in figure 4. The perturbation at t=0 is strongest in the cross-stream velocity components and, most interestingly, it appears localized in all three spatial directions. Nonlinearity is active where the amplitude is locally large and this is not always reflected by the total energy, which is a global measure. The initial evolution of the disturbance is reported in figures 4(b) and 4(c) while the behavior of the integral energy is shown in figure 3(b). The initial disturbance is inclined against the mean shear to extract more energy from the base flow via the Orr-mechanism At time t=10 the disturbance is up-right and still localized.

Transition is initiated by a pair of streamwise vortices that generate a single bent streak Cossu *et al.* (2010), see figure 4(c). The slow growth of the streak is associated to a decay of the cross-stream velocity components (see fig. 3b). However, once the streak reaches a sufficient amplitude at $t \approx 70$, secondary instability sets in as spanwise oscillations induced by a staggered pattern of vorticity. Rapid breakdown to turbulence is then observed to occur at $t \approx 130$.

To determine the initial condition of minimum energy leading to laminar/turbulent transition in plane Couette flow we have resorted to thermodynamics considerations. Using the general evolution criterion we have optimized the route to the statistically steady state the system wants to reach: this is the state of maximum entropy production and coincides with the turbulent state for large enough values of the Reynolds number and of the initial perturbation energy. Nonlinear optimization is needed to determine this optimal initial condition and the energy threshold below which turbulence cannot ensue. For realistic domain sizes the optimal initial condition is localized in the three spatial directions. The transition path is characterized by the occurrence of a single bent velocity streak whose oscillations increase rapidly at breakdown. Although computationally expensive, the approach proposed is not limited to simple flows, and the next step is to extend the present results to flows that are inhomogeneous in the streamwise direction.

The authors acknowledge Carlo Cossu for fruitful discussions. Computer time provided by SNIC (Swedish National Infrastructure Centre) is gratefully acknowledged.

References

- Cherubini, S., De Palma, P., Robinet, J.-Ch. & Bottaro, A. 2010 Rapid path to transition via nonlinear localized optimal perturbations in a boundary-layer flow. *Phys. Rev. E* 82 (6), 066302.
- Cossu, Carlo, Chevalier, Mattias & Henningson, Dan S. 2010 Secondary optimal growth and subcritical transition in the plane poiseuille flow. In *Seventh IUTAM Symposium on Laminar-Turbulent Transition*, , vol. 18, pp. 129–134. Springer, Stockholm.
- DI VITA, A. 2010 Maximum or minimum entropy production? how to select a necessary criterion of stability for a dissipative fluid or plasma. *Phys. Rev. E* **81** (4), 041137.
- DIVITA, A & BRUSATI, M 1995 Minimum entropy production principle due to ohmic dissipation in tokamaks and determination of non-inductive current density profiles on jet. *Plasma Physics and Controlled Fusion* **37** (10), 1075.
- Duguet, Y., Brandt, L. & Larsson, B. R. J. 2010 Phys. Rev. E 82, 026316.
- ECKHARDT, B. 2007 Annu. Rev. Fluid Mech. 39, 447.
- GLANSDORFF, P. & PRIGOGINE, I. 1964 On a general evolution criterion in macroscopic physics. *Physica* **30** (2), 351 374.
- Hof, Bjorn, van Doorne, Casimir W. H., Westerweel, Jerry, Nieuwstadt, Frans T. M., Faisst, Holger, Eckhardt, Bruno, Wedin, Hakan, Kerswell, Richard R. & Waleffe, Fabian 2004 Experimental Observation of Nonlinear Traveling Waves in Turbulent Pipe Flow. *Science* **305** (5690), 1594–1598.
- Juretic, Davor & Zupanovic, Pasko 2003 Photosynthetic models with maximum entropy production in irreversible charge transfer steps. *Computational Biology and Chemistry* 27 (6), 541 553.
- KAWAHARA, GENTA 2005 Laminarization of minimal plane couette flow: Going beyond the basin of attraction of turbulence. *Physics of Fluids* **17** (4), 041702.
- Malkus, W. V. R. 1956 Outline of a theory of turbulent shear flow. Journal of Fluid Mechanics 1 (05), 521–539.
- Mullin, T. 2011 Annu. Rev. Fluid Mech. 43, 1.
- Ozawa, Hisashi, Ohmura, Atsumu, Lorenz, Ralph D. & Pujol, Toni 2003 The second law of thermodynamics and the global climate system: A review of the maximum entropy production principle. *Rev. Geophys.* 41 (4), 1 24.
- Paltridge, Garth W. 1979 Climate and thermodynamic systems of maximum dissipation. *Nature* **279** (6), 630 631.
- Pringle, C. C. T. & Kerswell, R. 2010 Phys. Rev. Lett. 105, 154502.
- Rebhan, E. 1990 Maximum entropy production far from equilibrium: The example of strong shock waves. *Phys. Rev. A* 42 (2), 781–788.
- REDDY, S. C. & HENNINGSON, D. S. 1993 J. Fluid Mech. 252, 209-238.
- Schmid, P. J. & Henningson, D. S. 2001 Stability and transition in shear flows. Springer, New York.
- VISWANATH, D. & CVITANOVIC, P. 2009 J. Fluid Mech. 627, 215.

Paper 4

4

DNS and LES of estimation and control of transition in boundary layers subject to free-stream turbulence

By Antonios Monokrousos, Luca Brandt, Philipp Schlatter & Dan S. Henningson

Linné Flow Centre, Department of Mechanics Royal Institute of Technology, SE-100 44 Stockholm, Sweden

International journal of heat and fluid flow, 29, Issue 3 841-855, 2008

Transition to turbulence occurring in a flat-plate boundary-layer flow subjected to high levels of free-stream turbulence is considered. This scenario, denoted bypass transition, is characterised by the non-modal growth of streamwise elongated disturbances. These so-called streaks are regions of positive and negative streamwise velocity alternating in the spanwise direction inside the boundary layer. When they reach large enough amplitudes, breakdown into turbulent spots occurs via their secondary instability. In this work the bypass-transition process is simulated using direct numerical simulations (DNS) and large-eddy simulations (LES). The ADM-RT subgrid-scale model turned out to be particularly suited for transitional flows after a thorough validation.

Linear feedback control is applied in order to reduce the perturbation energy and consequently delay transition. This case represents therefore an extension of the linear approach (Chevalier $et\ al.\ 2007a$) to flows characterised by strong nonlinearities. Control is applied by blowing and suction at the wall and it is both based on the full knowledge of the instantaneous velocity field (i.e. full information control) and on the velocity field estimated from wall measurements.

The results show that the control is able to delay the growth of the streaks in the region where it is active, which implies a delay of the whole transition process. The flow field can be estimated from wall measurements alone: The structures occurring in the "real" flow are reproduced correctly in the region where the measurements are taken. Downstream of this region the estimated field gradually diverges from the "real" flow, revealing the importance of the continuous excitation of the boundary layer by the external free-stream turbulence. Control based on estimation, termed compensator, is therefore less effective than full information control.

1. Introduction

The aim of this study is to perform numerical simulations to apply linear feed-back control to transitional boundary-layer flows in the presence of free-stream turbulence where bypass transition occurs. An efficient pseudo-spectral numerical discretization is used and tools from modern control theory are incorporated into the controller design. Both large-eddy and direct numerical simulations are performed for evaluating the control efficiency in a highly nonlinear configuration.

1.1. Flow Control

Control of wall-bounded transitional and turbulent flows is the object of the present investigation owing to the high potential benefits. Any reduction of the skin friction, for example, implies relevant savings of the operational cost of commercial aircrafts and cargo ships. In particular the bypass transition scenario considered here is relevant in turbomachinery where high levels of free-stream turbulence are present.

Direct numerical simulations (DNS) have provided physical insight into the phenomena of transitional and turbulent flows, despite the fact that they are limited to simple and moderate Reynolds-number flows (Moin & Mahesh 1998). The same tools are now adopted to investigate the feasibility and performance of feedback control algorithms on a complex transitional flow case.

A linear model-based feedback control approach, that minimises an objective function which measures the perturbation energy, is formulated where the Orr-Sommerfeld and Squire equations model the flow dynamics. The latter equations describe the linear evolution of perturbations evolving in a parallel base flow. The requirement implicit in this formulation is the need of complete state information. However, the control problem can be combined with a state estimator to relax this requirement. The information problem is a limiting factor in the success of a control scheme, since, as a first step, it affects the whole procedure. The so-called Kalman and extended Kalman filter have been implemented in order to reconstruct the flow in an optimal manner by only considering wall measurements (Kailath & Hassibi 2000).

Flow control has been the object of comprehensive investigation the past years and recently, much effort has been put in the combination of computational fluid dynamics and control theory. While early attempts of flow control were based on physical intuition or on a trial-and-error basis, more systematic approaches are now followed. General reviews on flow control can be found in Moin & Bewley (1994), Joslin *et al.* (1996), Bewley (2001) and Kim & Bewley (2007) to mention a few.

Different control strategies have been attempted over the years for transitional flows, for example, wave cancellation where Tollmien-Schlichting waves are damped by applying anti-phase signals. Early reviews on the subject can be found in Thomas (1990) and Metcalfe (1994). Wave-cancellation methods for control were applied already in the 80es both experimentally (Thomas 1983)

and numerically, see e.g. Laurien & Kleiser (1989). A more 'drastic' control strategy, also known as laminar flow control, consists in stabilising the flow by applying strong suction on the boundary layer thus modifying the mean flow profile. A review on this method can be found in Joslin (1998). Nonlinear control methods have been studied as well and an overview of these methods is given by Joslin et al. (1997). In many cases nonlinear control is applicable only within the conditions and parameter range that it is designed for. An example of a robust controller that addresses that problem is described by Bewley et al. (2000). Other examples of application of nonlinear controllers are Berggren (1998), Bewley et al. (2001) and Collis et al. (2000).

The use of linear feedback controllers has been investigated more recently. This was motivated by the understanding on how the energy growth of fluctuations in a turbulent flow is related to linear mechanisms. In particular, Farrell & Ioannou (1996), Henningson (1996) and Kim & Lim (2000) showed that linear mechanisms are important to sustain turbulence and thus linear controllers can be applied for turbulence control. One early work on linear feedback control schemes is Joshi et al. (1995). Results from the application of linear optimal control theory also confirm the importance of linear mechanisms in the nonlinear flows under consideration (Högberg & Henningson 2002). Relaminarisation of turbulent channel flow was achieved by Högberg et al. (2003a) with this method and the controller and estimator were combined by Högberg et al. (2003b). The combined control and estimation problem is also known as a "compensator".

Recent studies from our group on the application of model-based linear feedback control have shown the importance of physically relevant stochastic models for the estimation problem which turns out to be crucial for fast convergence (Hoepffner et al. 2005; Chevalier et al. 2006). Such stochastic noise needs to describe accurately enough the unmodelled dynamics, like uncertainties and nonlinearities. Based on these models the estimator is shown to work for both infinitesimal as well as finite amplitude perturbations in numerical simulations. The compensator has been applied to spatially developing boundary layers and shown to reduce the perturbation energy of both modal and non-modal disturbances (Chevalier et al. 2007a).

1.2. Bypass transition

Laminar-turbulent transition in a zero-pressure-gradient boundary layer subject to high levels of free-stream turbulence is considered. Such a scenario is usually referred to as bypass since the transition occurs bypassing the exponential growth of the Tollmien-Schlichting waves. It has indeed been shown both experimentally and theoretically that the asymptotic solutions given by the classical stability analysis are not always adequate to predict transition in wall-bounded shear flows. In some cases significant energy growth can be observed even when the flow is stable (Schmid & Henningson 2001). This can be explained by the non-normality of the the linearised operator describing the

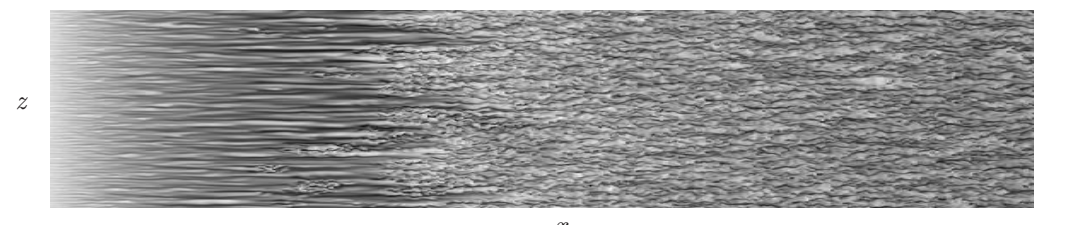


FIGURE 1. Visualisation of the streamwise disturbance velocity component (dark colour is low velocity, light high velocity) in a plane close to the wall showing the flow development under the influence of free-stream turbulence. Streamwise extent $Re_x = [32000,\ 570000]$, true aspect ratio. The streamwise extent corresponds to almost the full length of a typical turbine blade.

flow dynamics and the associated non-orthogonal set of eigenmodes (Reddy & Henningson 1993). If the state of the system has a strong projection on some of these highly non-orthogonal eigenmodes the energy of the flow can experience a significant transient growth. In the case of boundary layers, the upstream perturbations which undergo the largest possible growth consist of streamwise counter-rotating vortex pairs, see Andersson et al. (1999). These vortices lift low-momentum fluid from the wall and push high-momentum fluid from the outer parts towards the plate, thus creating elongated regions of alternating accelerated and decelerated fluid, called streaks. This process of vortex tilting is also known as lift-up effect (Landahl 1980).

After the primary energy growth due to the lift-up effect, the flow is in a more complicated laminar state where strong nonlinear interactions can come into play, leading to transition to turbulence. As the streaks grow in strength, they become susceptible to high-frequency secondary instabilities due to the presence of both wall-normal and spanwise inflectional velocity profiles (Brandt & Henningson 2002; Brandt 2007). These secondary instabilities manifest themselves in symmetric and antisymmetric streak oscillations, which are precursors to the formation of localised regions of chaotic swirly motion, the socalled turbulent spots (Brandt et al. 2004; Mans et al. 2007). The leading edge of a spot travels at about the free-stream velocity U_{∞} while the trailing edge at half this speed. The spots become therefore more elongated and eventually merge: a fully-developed turbulent boundary layer is observed. A visualisation of the transition under free-stream turbulence from the simulations presented here is provided in figure 1. Streamwise streaks can be seen to form close to the computational inlet, followed by streaks oscillations and turbulent spots. The flow is turbulent in the second half of the domain.

The bypass transition scenario is observed when the boundary layer is subject to free-stream turbulence levels higher than 0.5-1% (Matsubara & Alfredsson 2001). As described above, the flow reproduces, though on a larger

scale, the near-wall dynamics of wall-bounded turbulence, see e.g. Robinson (1991), and it is therefore and ideal test configuration in view of possible control of turbulent flows. This work represents therefore a natural extensions of the flow control studies mentioned above (Hoepffner $et\ al.\ 2005$; Chevalier $et\ al.\ 2007a$) to flows characterised by strong nonlinear interactions. An experimental demonstration of reactive control of the same scenario was recently presented by Lundell (2007). In this study, an ad-hoc threshold-and-delay control algorithm is evaluated and shown to inhibit the growth of the streamwise velocity fluctuations for a distance downstream of the actuator position.

The paper is organised as follows. In section 2 the control approach is presented while the numerical method, the large-eddy simulation and the free-stream turbulence generation are introduced in section 3. The results are presented in section 4. First, the focus will be on the validation of the LES while in the second part of section 4, linear feedback control applied to bypass transition is considered. The paper ends with a summary of the main conclusions.

2. Feedback control

Linear analysis is commonly used to understand the energy growth mechanisms of perturbations in shear flows (Schmid & Henningson 2001). However, it can also be used as a tool to design controllers that actively reduce the perturbation level and prevent or delay transition. The procedure adopted here is linear feedback control based on noisy measurements within the Linear Quadratic Gaussian (LQG) framework where a Linear Quadratic Regulator (LQR) is combined with a Kalman filter (Friedland 1986).

Within this framework a set of linear equations is used as a model for the physical process to be controlled along with a quadratic objective function. The system is assumed to be subject to Gaussian random excitations which represent unmodelled dynamics, e.g. nonlinearities. The control requires knowledge of the full state of the system. Therefore a state estimator, also called Kalman filter, is used to reconstruct the flow field from noisy measurements taken at the wall. To model uncertainties in the measurements, noise is assumed to contaminate the output signals. The control and estimation problem can be considered and solved separately and when combined it can be proven that this is the optimal solution (Skogestad & Postlethwaite 2005). This is known as the separation principle. Control can be applied both in the real and in the estimated flow. The combination of an estimator and a full information controller is called compensator.

The design of a controller aims at finding the optimal mapping between the various inputs and outputs of the system in such a way that a certain objective is obtained. In this case the system is the boundary layer flow, inputs are the external disturbances from the free stream (unknown) and the blowing/suction at the wall (known) while output is the wall measurements (known). The objective here is to reduce the kinetic energy of the perturbations in the flow.

2.1. Control

In this section the design process of the full information controller is presented. Therefore it is assumed that the exact state of the system is known.

To model the flow, the linearised Navier-Stokes equations are employed

$$\frac{\partial \mathbf{u}}{\partial t} + \mathbf{U}\nabla \mathbf{u} + \mathbf{u}\nabla \mathbf{U} = -\nabla \pi + Re^{-1}\nabla^2 \mathbf{u}$$
 (1a)

$$\nabla \mathbf{u} = 0, \tag{1b}$$

where $\mathbf{u} = [u \ v \ w]^T$. The streamwise, wall-normal and spanwise directions are denoted x, y and z respectively, with the corresponding velocity components u, v and w and wavenumbers k_x , k_y and k_z .

In equations 1 we consider small perturbations around the base flow $\mathbf{U} = [U\ V\ W]^T$. To reduce the order of the system a parallel base flow is assumed $\mathbf{U} = [U(y)\ 0\ 0]^T$ and under this assumption Fourier transform can be applied along the wall-parallel directions. Thus we can treat each wavenumber pair individually and instead of solving one problem with a large number of degrees of freedom, we solve many smaller systems. For the channel flow this assumption is exact, whereas for boundary layers, it is a good approximation due to their slow viscous growth.

To eliminate the pressure the wall-normal velocity v and wall-normal vorticity η formulation is adopted where the state is $(v \ \eta)^T$. The equations that describe the dynamics are the Orr-Sommerfeld/Squire (OSS) system (see Schmid & Henningson (2001))

$$\frac{\partial}{\partial t} \begin{pmatrix} v \\ \eta \end{pmatrix} = \begin{pmatrix} \mathcal{L}_{OS} & 0 \\ \mathcal{L}_{C} & \mathcal{L}_{SQ} \end{pmatrix} \begin{pmatrix} v \\ \eta \end{pmatrix}$$
 (2)

where

$$\mathcal{L}_{OS} = [\Delta]^{-1} [-ik_x U \Delta + ik_x D^2 U + \frac{1}{Re} \Delta]$$

$$\mathcal{L}_{C} = -ik_z D U$$

$$\mathcal{L}_{SQ} = -ik_x U + \frac{1}{Re} \Delta.$$
(3)

U is the mean-flow profile, the similarity Blasius solution, Δ is the Laplacian operator $\Delta = D^2 - k^2$ with $k^2 = k_x^2 + k_z^2$ and D the wall-normal derivative. The Reynolds number Re is defined using the free-stream velocity U_{∞} and the local boundary-layer displacement thickness δ^* ,

$$Re = \frac{U_{\infty}\delta^*}{\nu} \,. \tag{4}$$

The control is applied through non-homogeneous boundary conditions as a model for localised blowing and suction at the wall. To adopt the same formulation as in classical control theory, the control signal is expressed in the equations as a volume forcing by a lifting procedure (Högberg & Henningson 2002). To account for non-modelled dynamics, such as non-parallel effects and nonlinearities, external excitation is added such that two extra forcing terms

appear in the equations

$$\frac{\partial \mathbf{q}}{\partial t} = \mathcal{A}\mathbf{q} + \mathcal{B}_1 \mathbf{w}_1 + \mathcal{B}_2 \psi \,, \tag{5}$$

where $\mathbf{q} = [v \ \eta \ \chi]^T$, $\mathscr{B}_1 \mathbf{w}_1$ is the forcing due to external excitations \mathbf{w}_1 of stochastic nature and $\mathscr{B}_2 \psi$ is the forcing from the control signal ψ and χ is the velocity at the wall. We thus have $\partial \chi/\partial t = \psi$. The operator \mathscr{A} governs the dynamics of the augmented system (Chevalier *et al.* 2007*a*). Note that the control signal is the time derivative of the blowing and suction at the wall. In the case of full state-feedback control the signal is calculated directly from the state \mathbf{q} so $\mathscr{B}_2 \psi = \mathscr{B}_2 \mathscr{K} \mathbf{q}$ where \mathscr{K} is the control gain.

The aim is to calculate the control gain \mathcal{K} so that the kinetic energy of the mean-flow disturbances is minimised while at the same time the control effort is kept at low levels. To this end the following objective function is defined,

$$\mathscr{F} = \int_0^T (\mathsf{q}^* \mathscr{Q} \mathsf{q} + \psi^* \mathscr{R} \psi) \, \mathsf{d}t \,. \tag{6}$$

where $(\cdot)^*$ denotes the complex conjugate. The term $q^*\mathcal{Q}q$ corresponds to the kinetic energy of the perturbations for the specific wavenumber pair under consideration where \mathcal{Q} is the energy norm operator. The second term in equation 6 represents the control effort, $\mathcal{R} = l^2$ where l is the actuation penalty.

As a next step we discretise the problem so that it can be solved numerically. The control problem is now redefined as a set of one-dimensional partial differential equations, one for each wavenumber pair. Along the wall-normal direction y, Chebyshev polynomials are used. In the case of unbounded domains the corresponding wall-parallel wavenumbers are a continuous set but in a bounded domain this set becomes discrete and the corresponding Fourier representation transforms from integrals into series. The series will be truncated to a wavenumber that corresponds to the resolution of the numerical simulation.

If q is the discrete state vector the energy norm operator Q is defined in such a way that the quantity q^HQq approaches the kinetic energy of the system as the resolution increases. q^H is the Hermitian transpose of q.

The discretised system has a similar form as the continuous one

$$\frac{\partial q}{\partial t} = Aq + B_1 w_1 + B_2 \phi \,, \tag{7}$$

where the quantities q, A, B_1 , w_1 , B_2 and ϕ are the equivalent discrete counterparts of q, \mathscr{A} , \mathscr{B}_1 , w_1 , \mathscr{B}_2 and ψ .

We use the Lagrange multipliers to find the optimal solution to our problem. We define the Lagrangian

$$\mathcal{L} = \int_0^T \left[\frac{1}{2} \left(q^H Q q + \phi^H R \phi \right) - p \left(\frac{\partial q}{\partial t} - A q - B_2 \phi \right) \right] dt, \qquad (8)$$

where p is the Lagrange multiplier and R is the discrete versions of \mathcal{R} . Here we have dropped the stochastic term B_1w_1 since we will use the deterministic approach in deriving the full information control. The variation of the Lagrangian functional can be written as

$$\delta \mathcal{L} = \left(\frac{\partial \mathcal{L}}{\partial q}\right) \delta q + \left(\frac{\partial \mathcal{L}}{\partial p}\right) \delta p + \left(\frac{\partial \mathcal{L}}{\partial \phi}\right) \delta \phi. \tag{9}$$

Combining equations 8 and 9 and assuming $\delta \mathcal{L} = 0$ leads to the set of equations

$$\frac{\partial \mathcal{L}}{\partial q} = \frac{\partial p}{\partial t} + A^H p + Qq = 0 \tag{10a}$$

$$\frac{\partial \mathcal{L}}{\partial p} = -\frac{\partial q}{\partial t} + Aq + B_2 \phi = 0 \tag{10b}$$

$$\frac{\partial \mathcal{L}}{\partial \phi} = R\phi + B_2^H p = 0. \tag{10c}$$

A linear time dependent relation is assumed between the forward solution q and the Lagrange multiplier p = Xq. Inserting this assumption into equation 10a and adding equations 10a and 10c we arrive at the differential Riccati equation

$$\frac{\partial X}{\partial t} + A^H X + XA - XB_2 R^{-1} B_2^H X + Q = 0.$$
 (11)

The optimal K is then given through the non-negative Hermitian solution X of equation 11. A full derivation of the above equation is given by Lewis & Syrmos (1995). A simplified version arises if an infinite time horizon is assumed, yielding the steady-state Riccati equation

$$A^{H}X + XA - XB_{2}R^{-1}B_{2}^{H}X + Q = 0. {12}$$

with the control gain computed from

$$K = -R^{-1}B^H QX. (13)$$

The Riccati equation is solved for each streamwise and spanwise wavenumber pair (k_x, k_z) separately and an inverse Fourier transform can be applied to visualise the control gains in physical space. It is shown by Högberg & Henningson (2002) that the control gains, relating the velocity perturbations to the control signal, are spatially localised: The control is thus dependent only on the perturbations in a limited region located upstream of the actuator.

2.2. Estimation

The duty of the estimator is to approximate the full three-dimensional velocity field from wall measurements in real time. Measurements are taken from the wall and the sensors responsible for the measurements include noise. The estimator can be seen as a filter operator where the equations governing the flow are used for the filtering process. Input is the measurements from the real flow and output the estimated flow. This is often called Kalman filter.

In the estimation problem two flow fields are considered: The 'real' flow and the estimated flow (see figure 2). All the quantities that correspond to the estimated flow are marked with a hat $(\hat{\cdot})$.

The estimated field is assumed to fulfill the following equation

$$\frac{\partial \hat{q}}{\partial t} = A\hat{q} - L(r - \hat{r}) + B_2\phi, \qquad (14)$$

where L is the measurement gain and r indicates the measurements. The latter are extracted through the measurement operator C and since the measurements process introduces noise, we write r = Cq + g and $\hat{r} = C\hat{q}$, where g is the measurement noise. The governing equation for the estimation error can be written as

$$\frac{\partial \tilde{q}}{\partial t} = (A + LC)\tilde{q} + B_1 w_1 + Lg = A_e \tilde{q} + B_1 w_1 + Lg.$$
 (15)

The aim of the estimation problem is to minimise the difference between the real and the estimated flow, namely the estimation error $\tilde{q}=q-\hat{q}$. From the equations above the mathematical similarity between the feedback control and the estimation problem is evident. We are looking for the optimal L for which the objective function $\mathcal{F}=\tilde{r}^H\tilde{r}$ is minimised. However in this case we have to use the stochastic approach instead of the deterministic, since the equation is forced by stochastic inputs.

We assume that the external disturbances w_1 and g are zero-mean stationary white noise Gaussian processes (Chevalier *et al.* 2007*a*). Since the system is forced by these stochastic processes, expected values of the relevant flow quantities are examined. In particular for the estimation problem the covariance of the estimation error P is considered and, as for the full information control, a steady state is assumed. The covariance of the error satisfies the algebraic Lyapunov equation

$$A_e P + P A_e^H + B_1 W B_1^H + L G L^H = 0, (16)$$

where W and G are the covariances of w_1 and g respectively. This along with the objective function \mathcal{F} form a new Lagrangian \mathcal{M} where the traces of the covariance matrices are involved. The trace of covariance matrices correspond to rms (root-mean-square) values of the quantity under consideration (Hoepffner et al. 2005).

$$\mathcal{M} = trace(PQ) + trace[\Lambda(A_eP + PA_e^H + LGL^H + B_1WB_1^H)] \tag{17}$$

where Λ is the Lagrange multiplier. The first term in equation 17 is the objective function to be minimised and the second is the constraint coming from the Lyapunov equation satisfied by the covariance error. At the stationary point of \mathcal{M}

$$\frac{\partial \mathcal{M}}{\partial P} = Q + (A + LC)^H \Lambda + \Lambda^H (A + LC) = 0$$
 (18a)

$$\frac{\partial \mathcal{M}}{\partial \Lambda} = (A + LC)P + P(A + LC)^H + B_1 W B_1^H + LG L^H = 0 \tag{18b}$$

$$\frac{\partial \mathcal{M}}{\partial L} = 2\Lambda (PC^H + LG) = 0. \tag{18c}$$

The solution to this optimisation problem is given by the numerical solution P of a Riccati equation similar to that arising in the feedback control problem

$$AP + PA^{H} - PC^{H}G^{-1}CP + B_{1}WB_{1}^{H} = 0, (19)$$

with the estimation feedback gain given by $L = -PC^HG^{-1}$. For a similar derivation see also Bagheri *et al.* (2007).

In the computations presented, three quantities are measured at the wall, namely the streamwise and spanwise skin friction and the pressure

$$\tau_x = \tau_{xy}|_{wall} = \frac{1}{Re} \frac{\partial u}{\partial y}\Big|_{wall}$$
(20a)

$$\tau_z = \tau_{zy}|_{wall} = \frac{1}{Re} \frac{\partial w}{\partial y}\Big|_{wall}$$
(20b)

$$p_{wall} = \Delta_{xz}^{-1} \left(\frac{1}{Re} \frac{\partial^3 v}{\partial y^3} \right) \bigg|_{vall}$$
 (20c)

where Δ_{xz}^{-1} denotes the formal inverse of the wall-parallel Laplacian.

The Kalman filter presented here is the optimal estimation in a linear setting. To apply the above theory in a highly nonlinear case, one may use the full (nonlinear) equations when solving the estimation problem 14 while the gains used are computed with the linear theory. This is the extended Kalman filter and it is expected to be more accurate than the standard Kalman filter.

2.3. Compensator

The compensator is the combination of full information control and state estimation. The measurements taken from the real flow are communicated to the estimator where they are used to compute the forcing needed to reproduce the perturbations present in the real flow. The actuation signal is computed from the estimated flow and it is applied to both the estimated and the real flow. Although computed for linear systems, the control and estimation are applied to the full nonlinear Navier-Stokes equations (Högberg et al. 2003c).

The compensator problem as it was stated here accounts only for parallel flows as there is no explicit streamwise dependence in the OSS operator. Further, it assumes that measurements are taken and actuation is applied continuously over the whole domain. This theory is applied to a spatial boundary layer and both measurements and actuation are available only on a part of the domain (see figure 2). Two regions need to be specified, one for the control and one for the estimator. For both regions, the local laminar velocity profile is used as a base flow in the OSS operator. The flow is assumed to be locally parallel around these locations in order to solve the control and estimation problems. Once the control and estimation gains are calculated, the actuation forcing is limited to the actuation region by a smooth transfer function in physical space

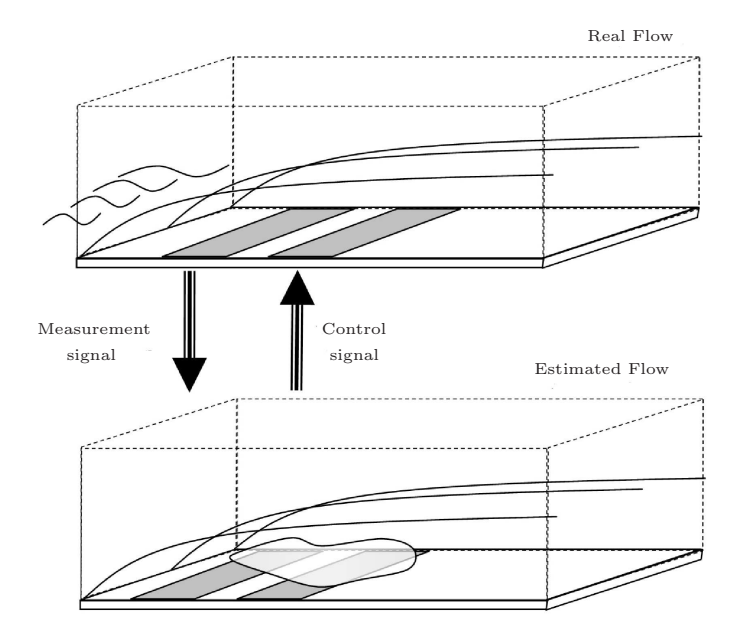


FIGURE 2. A schematic drawing of the compensator. Wall measurements are taken in the real flow and compared to those from the estimator. The control signal is computed based on the reconstructed velocity field and applied in the real flow.

with two smooth step functions around the chosen locations (Chevalier *et al.* 2007a).

3. Simulation approach

3.1. Numerical method

For the present computations, the three-dimensional, time dependent, incompressible Navier-Stokes equations are solved using a spectral method (Chevalier $et\ al.\ 2007b$). The algorithm uses Fourier representation in the streamwise and spanwise directions and Chebyshev polynomials in the wall-normal direction, together with a pseudo-spectral treatment of the nonlinear terms. Dealiasing using the 3/2-rule is employed in the wall-parallel (Fourier) directions, whereas a slightly increased resolution is used in the wall-normal direction to reduce aliasing errors. The time is advanced with a four-step low-storage third-order Runge-Kutta method for the nonlinear terms and all the forcing contributions, and a second-order Crank-Nicolson scheme for the linear terms and boundary conditions. To correctly account for the downstream boundary-layer growth the spatial simulation approach is necessary. This requirement is combined with the periodic streamwise boundary condition by the implementation of a fringe region (Nordström $et\ al.\ 1999$; Lundbladh $et\ al.\ 1999$). In this region,

positioned at the downstream end of the computational box occupying approximately 10% of the flow domain, a volume forcing is smoothly raised from zero to force the flow from the outflow to the desired inflow condition. The inflow consists of the laminar Blasius boundary layer with superimposed spatially and temporally varying disturbances, i.e. the free-stream turbulence in the present case.

3.1.1. MPI implementation and performance

The numerical code described above is parallelised to run on distributed-memory architectures (i.e. clusters) using the Message Passing Interface (MPI). As detailed in section 2.3, the simulation of the estimator and compensator actually requires the time-advancement of two flow fields, i.e. the "real" flow field and the estimated field. These two fields are coupled by the measurements and the control actuation (in case of compensator), and feature different inflow conditions and may have different spatial resolution and domain size. In the present implementation this is achieved by having two simulations running simultaneously on a subset of the available processors; the two simulations have two different executables, compiled with different options but running within the same MPI environment. Information exchange is then accomplished using distinct messages sent between the two codes. Details on the implementation can be found in Seyed (2007).

To give an estimate of the computational cost, the details of a typical simulation are now outlined. The "real" flow is simulated via direct numerical simulation (DNS) discretised on a domain with approximately $20 \cdot 10^6$ grid points. The corresponding estimator simulation can be run as a large-eddy simulation (LES) (see section 3.2 below) with a lower resolution of approximately $2.5 \cdot 10^6$ grid points. In this example, the DNS is run on 24 processors, and the estimator LES on 6 processors, i.e. employing a total of 30 processors. The necessary runtime in order to obtain fully converged statistics (simulated time $\Delta t = 4000$) is about 300 hours on 30 processors corresponding to 9000 CPU hours.

3.2. Sub-grid scale modelling

The fine grids (and the corresponding small time steps) necessary in the DNS of turbulent flows at moderate to high Reynolds numbers give rise to very high computational costs. Therefore, other approaches based on large-eddy simulations (LES) have been developed to be able to simulate transitional and turbulent flows in large-enough domains and at high Re. In LES the mesh size is chosen considerably larger than for DNS. This implies that the structures present in the flow are only resolved above a certain size corresponding to the cutoff wavenumber $\omega_{c,grid}$. This length scale is chosen to be small enough to capture well the structures that are involved in the physical phenomena under investigation. On the other hand, the scales below the cutoff scale are not resolved on the numerical grid, but their influence due to nonlinearity onto

the resolved scales must be modelled by a subgrid-scale (SGS) model. For flows with solid walls, the thin boundary layers adjacent to the walls need to be resolved in both DNS and LES for accurate results. Therefore, even LES requires a substantial computational effort, albeit lower than DNS: A typical resolution for an LES is approximately 1-20% of a corresponding fully-resolved DNS.

Formally, the solution in an LES calculation is obtained by applying a generic low-pass filter G^P with a certain filter width Δ suitable for the problem under consideration,

$$\bar{u}_i(x) := G^P * u_i := \int_{\mathcal{V}} G^P(x, x', \Delta) u_i(x') dx' ,$$
 (21)

where $\bar{u}_i(x)$ denotes the filtered quantity and \mathcal{V} the computational domain. G^P is referred to as the primary LES filter. The governing momentum equations for the filtered quantities become

$$\frac{\partial \bar{u}_i}{\partial t} + \frac{\partial \bar{u}_i \bar{u}_j}{\partial x_j} = -\frac{\partial \bar{p}}{\partial x_i} - \frac{\partial \tau_{ij}}{\partial x_j} + \frac{1}{Re} \frac{\partial^2 \bar{u}_i}{\partial x_j \partial x_j}$$
(22)

together with filtered incompressibility constraint

$$\frac{\partial \bar{u}_i}{\partial x_i} = 0 \ . \tag{23}$$

The interaction between the resolved and unresolved scales is given by the SGS stresses,

which is an unclosed term and thus has to be modelled based on the filtered velocity field \overline{u}_i . In most LES approaches the primary filter is not applied explicitly, but rather given by the implicit filter due to the lower grid resolution.

The ADM-RT model used here acts on the velocity components directly. The model employs the relaxation term proposed in the context of the approximate deconvolution model (ADM) (Stolz & Adams 1999). It has been shown in e.g. Schlatter $et\ al.\ (2006a,b)$ that for spectral simulations the deconvolution operation applied in the ADM approach is not necessary. Therefore, the SGS force due to the ADM-RT model is given by (Schlatter $et\ al.\ 2004$)

$$\frac{\partial \tau_{ij}}{\partial x_i} = \chi H_N * \bar{u}_i , \qquad (25)$$

with χ being the model coefficient. H_N denotes a high-order three-dimensional high-pass filter (Stolz *et al.* 2001), and the symbol * stands for convolution in physical space, i.e. a multiplication with the respective transfer function \hat{H}_N in Fourier space.

The high-pass filter H_N used in the present work is obtained by the repeated application of a low-pass filter G according to

$$H_N = (I - G)^{N+1}, \quad N > 0.$$
 (26)

Typically, G is chosen as the low-order low-pass filter suggested by Stolz *et al.* (2001). The cutoff frequency is defined as $\hat{G}(\omega_c) = 1/2$ and can be adjusted. For the present results, $\omega_c = 2\pi/3$ and N = 5. H_N is at least of order r(N+1) with r being the order of G. The latter is at least r = 3 on non-equidistant grids.

 χ is the model coefficient which is set to a constant value herein motivated by previous studies showing little dependency of the results on the actual value of the coefficient (see e.g. Schlatter *et al.* (2006b)). If the model coefficient χ is chosen inversely proportional to the time-step size the relaxation term has a similar effect as a filtering of the velocities after every time step, as mentioned in Stolz & Adams (1999).

The relaxation term $\chi H_N * \bar{u}_i$ is proportional to the small-scale velocity fluctuations in the flow field. Therefore, it will damp out these oscillations leading to a drain of kinetic energy from the smallest resolved scales.

The ADM-RT model proved to be accurate and robust in predicting transitional and turbulent incompressible flows with spectral methods (Schlatter et al. 2004, 2006b). Note that the relaxation-term model is related to the spectral vanishing viscosity approach (Karamanos & Karniadakis 2000). Due to the high-order filter H_N with a cutoff frequency of $\omega_c \approx 0.86\pi$ only the smallest represented eddies are affected, whereas the larger, energy-carrying scales are not directly influenced by the model contributions.

3.3. Free-stream turbulence generation

The boundary layer considered here is subject to external disturbances, in particular free-stream turbulence. To generate this inflow a superposition of eigenmodes from the continuous spectrum of the OSS operator is used (Jacobs & Durbin 2001; Brandt et al. 2004). In the present implementation disturbances can be introduced in the flow in three different ways: forcing them in the fringe region, with a body force as in the estimation problem, or via blowing and suction at the wall by a non-homogeneous boundary condition as done in the control problem. The free-stream turbulence is forced at the inflow by adding the modes to the laminar base-flow profile in the fringe region.

Detailed description of the procedure adopted can be found in Brandt et al. (2004). Here the free-stream generation is shortly outlined. A three-dimensional wave vector $\mathbf{k}=(k_x,k_y,k_z)$ is associated to each eigenfunction of the continuous spectrum where, k_x and k_z are defined by the normal-mode expansion along the wall-parallel directions of the underlying linear problem while the wall-normal wavelength is determined by the eigenvalue along the continuous spectrum. If Taylor's hypothesis is applied the streamwise wavenumber k_x can be replaced by a frequency $\omega=k_xU_\infty$ and the disturbance signal is written as

$$u_{dist} = \sum A_N \hat{u}_N(y) e^{ik_z z + ik_x x - i\omega t}, \qquad (27)$$

where the wall-normal wavenumber k_y is implicit in the shape of the eigenfunction $\hat{u}_N(y)$ (Grosch & Salwen 1978). The complex wavenumber k_x is determined

by the dispersion relation once the real wall-normal wavenumber k_y and the real wavenumbers k_z and ω are selected according to the procedure described below. The wavenumbers pertaining to the modes used in the expansion are selected by defining a number of spherical shells of radius |k| in the wavenumber space (ω, k_y, k_z) . 40 points are then placed at equal intervals on the surface of these spheres. The coordinates of these points define the wavenumbers of the modes used in the expansion above. The complex coefficients A_N provides random phase but a given amplitude. The amplitude $|A_N|$ is in fact the same for all modes on each shell and is chosen to reproduce the Von Kármán spectrum

$$E(k) = \frac{2}{3} \frac{a(kL_I)^4}{(b + (kL)^2)^{17/6}} L_I T u.$$
(28)

This spectrum is for large scales asymptotically proportional to k^4 , whereas it matches the Kolmogorov-(5/3)-law for small scales. In the expression above, Tu is the turbulence intensity, L_I is a characteristic integral length scale such that $k_{max} = 1.8/L_I$ where k_{max} is the wavenumber of maximum energy and a, b two normalisation constants.

3.3.1. Free-stream turbulence generation in the LES

Due to the lower resolution employed for the LES runs, the imposed turbulence spectrum at the inlet has to be adapted. To obtain results that are as close to the DNS as possible, it was decided to use exactly the same set of modes and the same random phases on all the various grids, without any modification of the turbulence intensity level at the inlet. Modes with wavenumbers too large to be resolved on a given coarser LES grid were discarded and consequently not forced at the inlet. All the other parameters specifying the inlet spectrum, i.e. length scale, choice of modes and the individual scaling of the modes, are the same on all grids. This leads to the observation that the measured turbulence intensity at the inlet is smaller for coarser grids, because less modes are actually forced. To obtain the true Tu one had to also include the unresolved fluctuations, which are however not available during an LES. The results show that the transition process is not crucially influenced by that difference in inlet Tu. If, on the other hand, the resolved Tu at the inlet is adapted to exactly match the level on the finest (i.e. DNS) grid, premature transition corresponding to the higher turbulence levels is observed. The explanation for this behaviour is that the receptivity of the boundary layer is mainly dominated by low-frequency modes of the free stream. The amplitudes of these modes, which are resolved on both the DNS and LES grids, should therefore not be modified.

3.4. Simulation parameters

The parameters defining the problem are the Reynolds number, the intensity and the integral length scale of the free-stream turbulence and the size of the computational box. The inflow Reynolds number $Re_{\delta_0^*}$, defined using the displacement thickness of the boundary layer at the inflow of the computational domain, was chosen to be 300 for all cases under consideration.

Table 1. Different computational boxes used. Resolution for each box dimensions and type of simulation. The box dimensions include the fringe region and are non-dimensionalised with respect to the displacement thickness δ_0^* at the inflow $(Re_{\delta_0^*} = 300)$

Box	Method	$L_x \times L_y \times L_z$	$N_x \times N_y \times N_z$
		δ_0^*	(resolution)
Small	DNS	$1000 \times 60 \times 50$	$1024 \times 121 \times 72$
Small	LES	$1000 \times 60 \times 50$	$256\times121\times36$
Medium	LES	$2000\times60\times90$	$512 \times 121 \times 64$
Large	LES	$2000 \times 60 \times 180$	$512 \times 121 \times 128$
X-Large	LES	$4000\times60\times180$	$1024\times121\times128$

The different computational boxes used are reported in table 1. Direct numerical simulations were only performed in the small box, while the largest boxes were used to allow the transition to turbulence to occur within the computational domain. The latter computational domains are thus used for the parametric study of bypass transition and its control. The medium-size box was used when investigating the influence of limiting the control signal (see section 4.2.1).

The code was run in four different modes, corresponding to four different physical problems: no control (used as reference case), full information control, estimation without control and compensator, i.e. control based on estimation.

4. Results

Based on the theory and numerical methods presented in the previous sections, simulations of transition in a flat-plate boundary layer subject to free-stream turbulence are performed. Linear feedback control is then applied to the flow in order to delay transition. Both LES and DNS are presented here and all the statistics presented are obtained by averaging in time and in the spanwise direction.

In the following results the streamwise coordinate is indicated by the Reynolds number based on the distance from the leading edge

$$Re_x = \frac{U_{\infty}x}{\nu} = \frac{Re_{\delta^*}^2}{1.7208},$$
 (29)

where the value of δ^* for the laminar Blasius solution is used. All the quantities presented are non-dimensionalised with the free-stream velocity, U_{∞} , the viscosity, ν and the displacement thickness at the inflow of the computational domain δ_0^* .

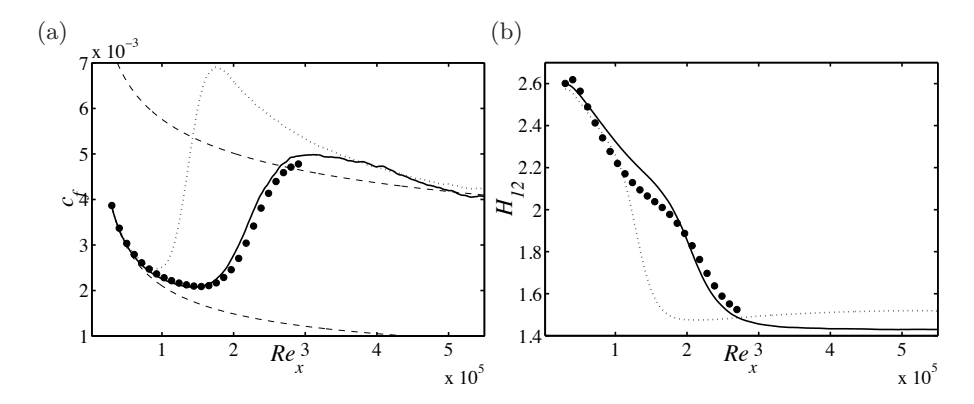


FIGURE 3. Integral quantities during bypass transition (Tu = 4.7%) for different SGS models. (a): skin-friction coefficient c_f , (b): shape factor H_{12} . ADM-RT, ——; no-model LES,; DNS, • (Brandt et al. 2004). The thin dashed lines correspond to analytical correlations for both laminar and turbulent boundary-layer flow.

4.1. LES validation

In a first step, the possibility to reduce the numerical resolution and consequently replacing the effect of the non-resolved scales by a subgrid-scale model (see section 3.2) is explored. In particular, additional to fully-resolved DNS, two different modelling approaches are considered: under-resolved DNS without model where the interaction between the resolved and unresolved scales is essentially neglected and the ADM-RT model. This SGS model has been shown to perform particularly well with transitional wall-bounded flows (Schlatter et al. 2006b). All the LES presented in this section are performed with a free-stream turbulence intensity of Tu = 4.7% on the "Large LES" grid given in table 1. The reference DNS data is taken from Brandt et al. (2004) using the same numerical method and inflow turbulence generation algorithm.

Figure 3 shows the evolution of the statistically averaged skin friction coefficient c_f and the shape factor H_{12} as a function of the downstream distance Re_x . The skin friction coefficient gives a measure on how well the near-wall flow structures can be represented, whereas the shape factor, being the ratio between the boundary-layer displacement thickness and the momentum thickness, describes the flow development and structural reordering of the boundary layer during laminar-turbulent transition further away from the wall.

The evolution of the skin friction (figure 3a) clearly shows that the nomodel approach without employing a subgrid-scale model leads to inaccurate results. This behaviour of under-resolved simulations is however well-known from other studies: The reduced dissipation present in the flow leads to an increased fluctuation level at the scales close to the numerical cutoff; in case of flows undergoing transition this increased energy may be causing premature





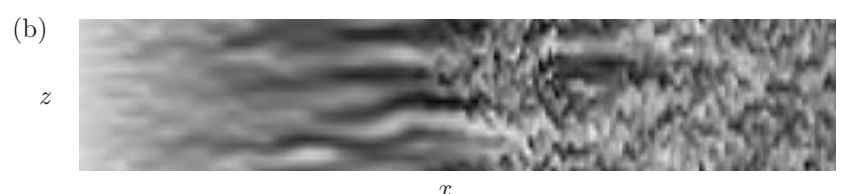


FIGURE 4. Instantaneous streamwise velocity in a plane parallel to the wall. (a): DNS. (b): LES using ADM-RT. Light colour indicates low velocity, dark colour high velocity. Streamwise extent $Re_x = [32000, 300000]$, spanwise extent enlarged by a factor of 5.

breakdown. Usually, increased values of the wall-normal velocity gradient close to the wall lead to a dominant overshoot of the skin friction, until the flow has settled down to a new equilibrium state accounting for the missing dissipation in the small scales. The ADM-RT model with a constant model coefficient however is seen to provide an accurate prediction of the skin friction throughout the laminar initial phase dominated by the streaky structures ($Re_x < 150000$), the stage dominated by the intermittent appearance and growth of turbulent spots ($Re_x < 300000$), and the fully-developed turbulent region thereafter.

The shape factor given in figure 3b confirms the previous findings: The initial phase ($Re_x < 100000$) characterised by only minor disturbances within the boundary layer is predicted accurately also by the no-model LES. However, as soon the boundary-layer distortion becomes too large, the under-resolved DNS will immediately break down to turbulence. It is interesting to note that the SGS model feature a slight departure from the reference level of H_{12} between $Re_x = 100000$ and $Re_x = 170000$; however the final stages of transition seem not to be influenced.

A comparison of an instantaneous visualisation of a wall-parallel plane at $y=2\delta_0^*$ from both DNS and ADM-RT is presented in figure 4. Note that for both simulations the same amplitudes and phase shifts in the inlet free-stream turbulence have been used (see section 3.3.1), consequently the flow structures can be directly compared between DNS and LES. The most obvious feature is that the LES data looks slightly blurred, which is a natural consequence of the lower resolution. Nevertheless, many of the flow structures present in the DNS flow field can also be detected in the LES field, and vice versa: the shape and location of the dominant strong streaks, the intermittent breakdown to localised turbulent spots, and a calm region even more downstream than the

Table 2. Control penalties, estimation sensor noise, measurement-strip position, actuation-strip position and location of the base flow target profiles for the estimator and the controller.

Estimation			Control		
Sensor noise	p	50	penalties	l	10^{2}
	$ \tau_x $	0.07		r^2	0
	τ_z	0.07			
$Re_{x_{start}}$		6.04×10^4	$Re_{x_{start}}$		1.95×10^{5}
$Re_{x_{end}}$		1.50×10^{5}	$Re_{x_{end}}$		2.85×10^{5}
location of tar-		1.05×10^{5}	location of tar-		2.40×10^{5}
get profile			get profile		

first turbulent patch. This figure clearly shows that – despite the lower resolution used in the LES – a good prediction of the dominating flow physics and the processes leading to turbulent breakdown can be obtained via appropriate subgrid-scale modelling. It can also be shown that the LES is able to capture the instantaneous structures just prior to turbulent breakdown.

4.2. Full information control

Results on linear feedback control of a boundary layer subject to free-stream turbulence are reported next. The design parameters for the compensator problem are reported in table 2 and will be discussed when presenting the results for each specific case.

The first step when applying control is to design a reasonably good full-information controller. This can be used as reference for the compensation, since the best possible performance is expected when the whole flow field is known. This case is also used as a benchmark for LES: Since LES is used for most of the simulations, it is considered important to evaluate the SGS model against DNS data not only in the general case without control, but also in the case of full information control. Further, in order to later compare these results to those from the compensator, the blowing and suction strip are placed further downstream, so that there will be enough space for the measurement region at the beginning of the computational domain, see table 2. Note that in the following figures the gray areas correspond to the regions where measurements are taken, and blowing and suction is applied, respectively. The simulations in the remaining part of this section are performed with a turbulence level Tu = 3.0% except the results in figure 6 where Tu = 4.7%.

In figure 5 the wall-normal maximum of the streamwise velocity perturbation is shown for both DNS and LES of the uncontrolled case as well as for the two cases with full information control. This quantity is selected since

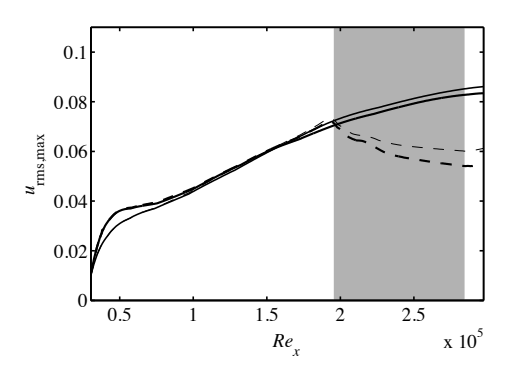


FIGURE 5. Wall-normal maximum u_{rms} . no control DNS, —; no control LES, —; control DNS, ----; control LES, ----.

it indicates the growth of the streaks inside the boundary layer. It can be clearly seen that the control is able to inhibit the streak growth and that using LES-(ADM-RT) gives similar decrease of the streak amplitude as in the fully-resolved DNS. Slight differences between LES and DNS can be noticed at the inlet of the domain. This can be explained by noting that the wall-normal maximum of the rms value is a very sensitive quantity, involving both the location and the amplitude of the fluctuations. Indeed mean quantities, like the skin friction, would not show any difference at all in such a plot.

A study to investigate the influence of the length of the control region on the transition delay was also performed. The free-stream turbulence level was chosen to be 4.7% to be able to reproduce the full transition process within the small computational domain (Barri 2006). The initial and final locations of the control region are reported in table 3, whereas the value of the wallnormal maximum of the streamwise velocity fluctuations and the skin friction are displayed in figure 6 for the three cases under consideration together with the reference uncontrolled case. It can be noticed in figure 6a that with a longer control domain, it is possible to reduce the streak growth even more. The effect of the control is more pronounced when looking at the friction coefficient c_f as shown in figure 6b. By comparing the two plots it can be deduced that the large values of streamwise velocity fluctuations at the end of the computational domain are not associated to a fully turbulent flow. The results farther show that for the longest control region the streak growth is indeed quenched for a larger distance but the downstream recovery is faster and the differences between the cases "Medium" and "Long" are attenuated further downstream.

In order to understand the physical mechanism behind the control, instantaneous features that appear in the controlled field are examined. In figure 7 the streamwise velocity component on a plane parallel to the wall at $y=2\delta_0^*$ (figure 7a) along with the wall-normal velocity component at the wall (figure 7b) indicating the control actuation via wall blowing and suction is displayed.

TABLE 3. Study on the influence of the control region length. The initial and final location of the control region are given in units of Re_x .

	Start	End
	(Re_x)	(Re_x)
No control		_
Short	5.3×10^{4}	1.4×10^{5}
Medium	5.3×10^{4}	1.9×10^{5}
Long	5.3×10^4	2.3×10^5

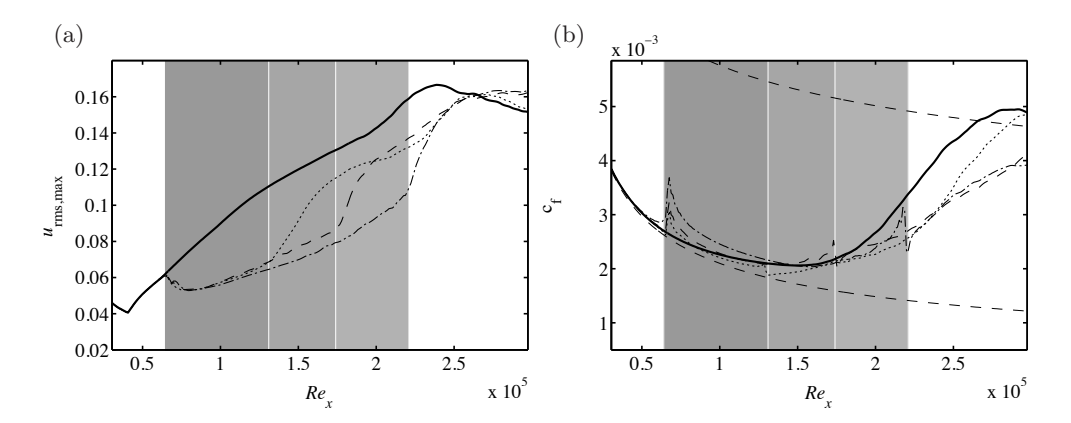


FIGURE 6. Wall-normal maximum u_{rms} (a) and skin friction coefficient c_f (b). no control, ——; short, ……; medium, ———; long, ——.

From these two instantaneous images of the flow one can see the correlation between the flow state and the control signal. In the case of a high-speed streak blowing is induced from the controller. This causes the flow downstream of the actuation to settle in a more stable state since the fast moving fluid is forced to move upwards away from the wall. The opposite action is happening for low-speed streaks i.e. the controller is applying suction to move high-speed fluid from the free stream to cancel the region of decelerated flow. One other aspect to note from this figure is that most of the control effort is concentrated at the beginning of the control region in agreement with the results by Chevalier $et\ al.$ (2007a).

4.2.1. Limiting of control signal

When extending the linear control to these highly nonlinear scenarios, problems may arise and $ad\ hoc$ tuning may be necessary. For our case, Brandt &



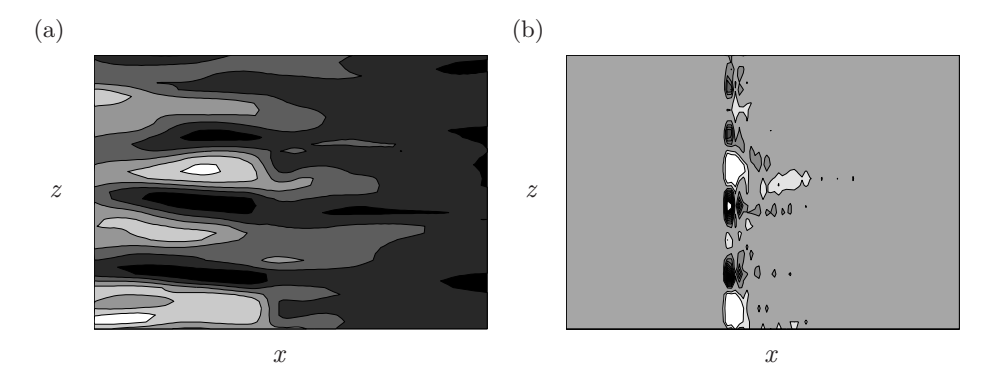


FIGURE 7. (a): Instantaneous streamwise velocity at $y=2\delta_0^*$. (b): corresponding control signal. The levels of the contours are $u=[0.3U_\infty,0.6U_\infty]$ for (a) and $v=[-2\times 10^{-2}U_\infty,5\times 10^{-3}U_\infty]$ for (b). White corresponds to the minimum value and black to the maximum.

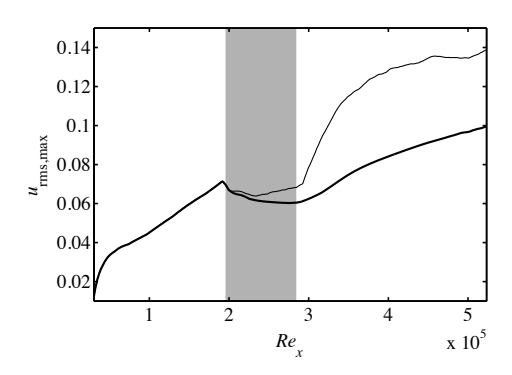


FIGURE 8. Wall normal maximum $u_{\rm rms}$. Control with clipping of the blowing, ——; Control without the clipping blowing,

Henningson (2004) observed that, if too strong localised blowing is applied, turbulent spots may be induced by local instabilities due to wall-normal inflectional profiles already inside the control region. An improvement of the transition delay can therefore be expected by limiting the blowing at the wall. This was implemented in the numerical code by imposing an artificial clipping to the control signal

$$v(x, y, z, t)|_{y=0} = \min\{v(x, y, z, t)_{y=0}, v_{\text{max}}\}|.$$
(30)

The clipping threshold v_{max} is set to $0.01U_{\infty}$, for cases where the (unlimited) maximum of the blowing at the wall occasionally reaches values of the order of $0.02U_{\infty}$. The value of v_{max} is chosen by examining the instantaneous values of

the blowing in cases where transition was triggered by the wall actuation. The comparison between the optimal linear control and control with limited blowing is displayed in figure 8, where the evolution of the wall-normal maximum of the streamwise velocity fluctuations is depicted for cases with and without clipping. The performance of the control is on average improved by limiting the blowing; analysis of the instantaneous velocity fields reveals that this is due to the absence of the localised spots intermittently induced by the strong control signals and not by an overall decrease of the streak amplitudes, or increase of the actuation efficiency. The results presented in the following are all obtained by limiting the blowing at the wall.

4.3. State estimation

The construction of the estimator involved extensive tuning of several parameters associated with the theoretical tools described in section 2.2. In particular, these parameters are: the covariance matrix as a model for the stochastic disturbances involved in the estimation process, the sensor noise quantifying the confidence in the measurements taken and the length of the estimation region.

The covariance matrix is essential for the estimator (see equation 19). In the ideal case, the measurements indicated in equation 20 would uniquely identify the current state of the system (Bewley & Protas 2004). This is not the case since there are unknown initial conditions, unknown external disturbances and noise corrupting the measurements. To improve the estimation in the case of free-stream turbulence, the variance of the external disturbances needed to be extended further out in the free stream if compared to that used in Chevalier $et\ al.\ (2007a)$. A diagonal matrix was used as covariance matrix for the external disturbances. For the covariance of the wall measurements a simple function proportional to the boundary-layer velocity profile was selected.

The parameters that define the strength of the forcing that is applied to the system are the sensor noise. The tuning of these parameters was also performed by testing different sets of values; the set of values yielding the best performance is reported in table 2. Note that a relatively large value of the pressure sensor is needed to achieve good estimation. This limits the use of this measurement and can be explained by the fact that the pressure at the wall appears to be more sensitive to the free-stream turbulence than to the streaks inside the boundary layer.

One would expect that the longer the measurement strip the better the estimation since more information from the flow is available. However, since the gains are computed for a parallel flow, this may not be the case and above a certain length the quality of the estimation degrades. The optimal length was found to be 500 approximately δ_0^* units. Further, it was found that at these high levels of perturbation, estimation works better if the forcing is active only on the scales that correspond to the streaks. Thus the gains where rescaled in wavenumber space with a two-dimensional Gaussian function. The parameters of this function were determined by applying two-dimensional Fourier

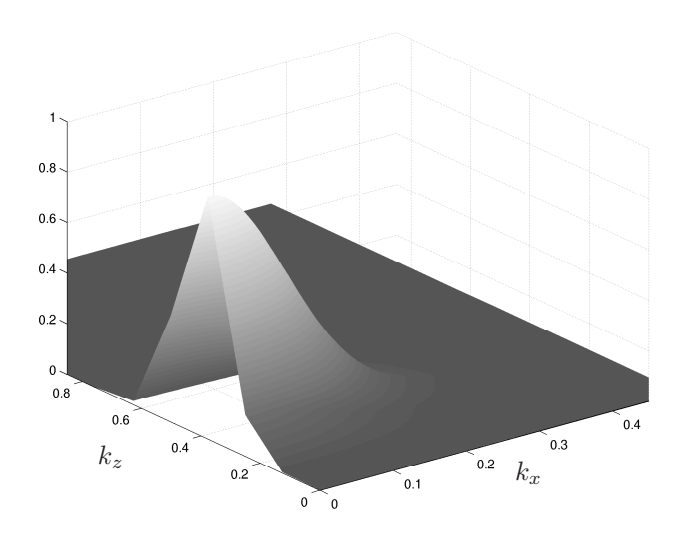


FIGURE 9. The Gaussian function scaling the estimation gains in wavenumber space. The centre of the Gaussian is at $k_x = 0$ and $k_z = 0.4$ in units of δ_0^{*-1} .

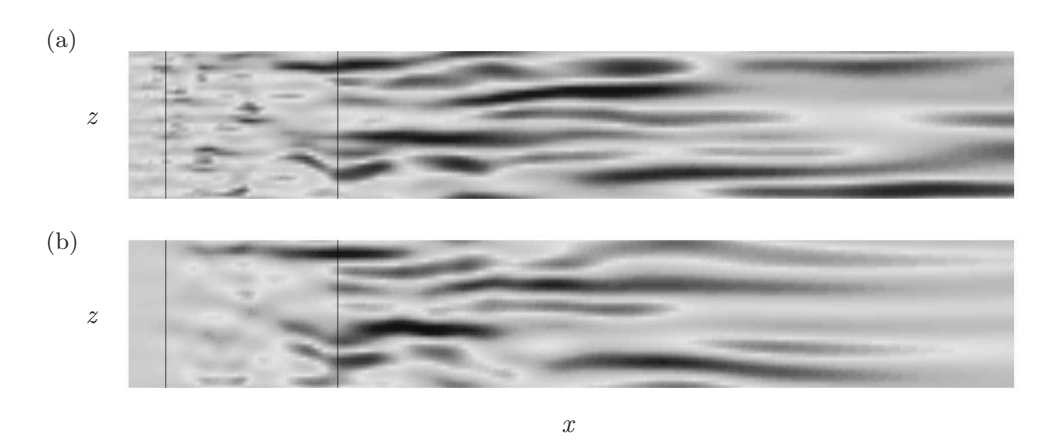


FIGURE 10. Instantaneous streamwise velocity fields. (a): real flow; (b): estimated flow. The measurement strip is indicated with two vertical lines. Streamwise extent $Re_x = [32000, 570000]$, spanwise extent enlarged by a factor of 5.

transforms along the wall-parallel directions to the flow fields to be estimated and extracting the wavenumbers of richest energy content. One example of this weighting function is shown in figure 9. The gains are focused around wavenumber $k_x=0.0$ in the streamwise direction, which corresponds to infinitely long structures and around $k_z=0.4$ which corresponds to the spanwise width of the most energetic structures, namely the streaks.

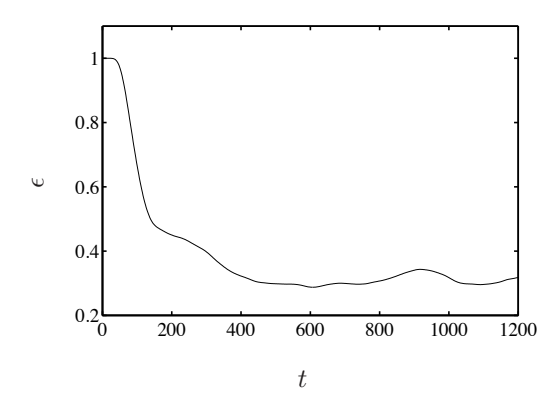


Figure 11. Estimation error according to equation 31.

Two different criteria were used to determine the performance of the estimator. The first was visual inspection of the instantaneous velocity fields: One example of this comparison can be seen in figure 10, where the streamwise velocity in a plane parallel to the wall is displayed for the real and the estimated flow. It can be seen in the figure that the main features of the incoming streaks are well reproduced in the estimated field. A second, more systematic way, is to calculate the estimation error given by

$$\epsilon = \frac{\int_{\Omega} (q - \hat{q}) d\Omega}{\int_{\Omega} (q) d\Omega}, \qquad (31)$$

where Ω is the region selected to evaluate the estimation error. In figure 11 the estimation error is plotted as a function of time. In this case the error is computed in a plane parallel to the wall, $y/\delta_0^*=2$, over the whole region where the control will be applied. This is selected as the most relevant area in terms of compensator performance since the flow in this region is used to compute the control signal. It can be seen in the figure that the estimation is converging toward values of $\epsilon \approx 0.3$ after an initial transient of about 400 time units.

The wall-normal maximum of the streamwise velocity perturbation is shown for both the real and the estimated flow in figure 12. The perturbations are weaker in the estimated flow, a strong estimation forcing leading directly to transition in the estimator simulation. In the real flow, the streaks are forming and growing also downstream of the estimation region, whereas in the estimated flow the streaks decay downstream of the measurement region. This can be explained by the fact that the free-stream turbulence is continuously forcing the streaks all along the plate whereas the estimation forcing is active only in a limited streamwise region, i.e. the gray area in the plot.

In figure 13 the wall-normal profiles of $u_{\rm rms}$ at different streamwise locations are shown. Again it can be seen that the streaks are weaker in the estimated flow than in the real flow, and that the difference between the two fields increases further downstream. Perturbations in the free stream are not

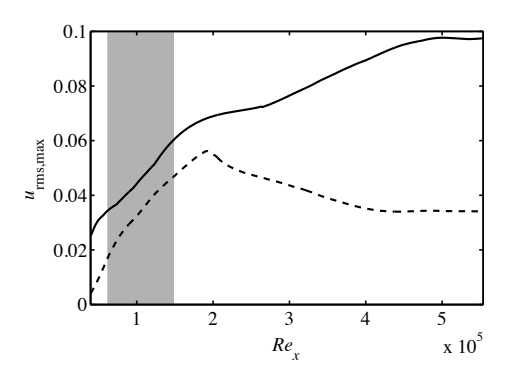


FIGURE 12. Wall-normal maximum of $u_{\rm rms}$. Real flow, ——; Estimated flow, ----. The shaded area indicates the measurement region.

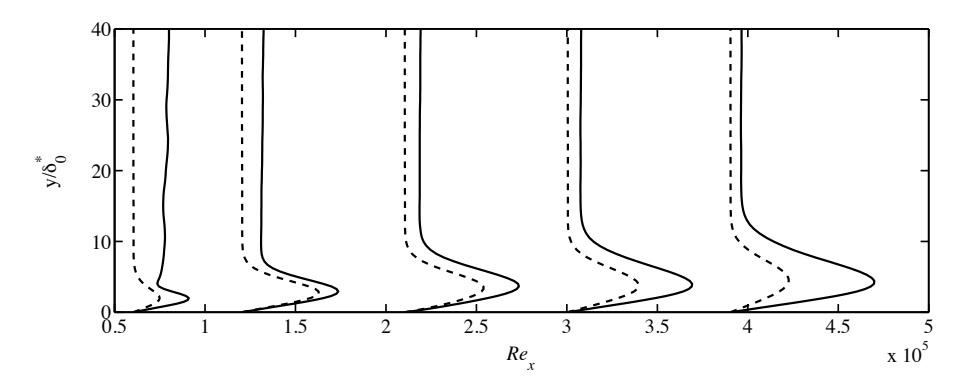


FIGURE 13. Wall normal profile of $u_{\rm rms}$ at different streamwise positions $Re_x = [0.6, 1.2, 2.1, 3.0, 3.9] \times 10^5$. The values of $u_{\rm rms}$ are scaled with 9.0×10^5 . Real flow, ——; Estimated flow, ———:

reproduced in the estimator and the estimation is more accurate close to the wall.

4.4. Compensator

The final stage is combining the full information controller and the estimator into the compensator. The procedure requires the estimator to run first without the control until the estimated field approaches the real flow; afterwards the control forcing is turned on. The control region is placed downstream of the estimated field and an overlap between the two strips is avoided. At the location where the actuation is active, the amplitude of the streaks is significantly increased. The perturbations to be controlled are further downstream i.e. in the region where non-linear effects are more important.

A visualisation of the controlled and uncontrolled flow field is displayed in figure 14 in a wall-parallel plane. The decrease of the streak amplitude in the control region is clearly visible. A turbulent spot is appearing further downstream in the uncontrolled flow while the flow is laminar when blowing/suction is applied. It can also be noticed that the control often changes an incoming high-speed streak into a low-speed region and vice versa. Further, a rapid increase in the streak amplitude is occurring after the end of the control region.

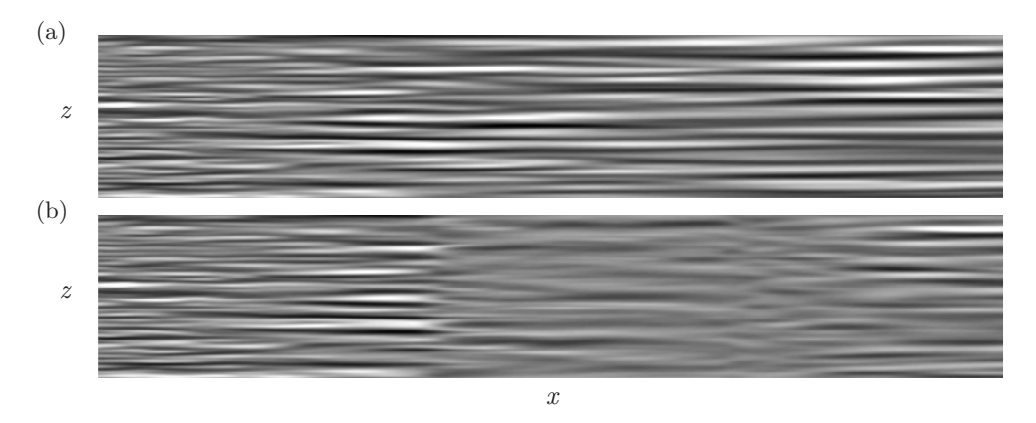


FIGURE 14. Instantaneous streamwise velocity fields. (a): uncontrolled; (b): controlled. Streamwise extent $Re_x = [32000,\ 382000]$, wall-normal distance $2\delta_0^*$, true aspect ratio.

In figure 15a the wall-normal maximum of the rms-value of the streamwise velocity perturbation is shown for the uncontrolled case and for both full information control and compensation. As observed by the flow visualisation in figure 15a, the growth of the the streaks is reduced within the control region. However, downstream of the control region, velocity fluctuations continue to grow. This can be explained by the presence of the free-stream turbulence above the boundary layer that is able to induce new perturbations inside the boundary layer.

The skin friction coefficient is shown in figure 15b. This plot quantifies the transition delay which can be achieved in the case of boundary-layer transition induced by free-stream turbulence. The transition delay obtained without estimation corresponds approximately to the length of the control region. The delay is between $120000\nu/U_{\infty}$ and corresponds to approximately 15-20% of the full length of a typical turbine blade, resulting in a reduction of the total friction drag of 5-10%. The loss of performance to be expected in the case of control based on estimation from wall measurements is not severe. Thus, a longer control region or alternatively a sequence of measurement and blowing/suction strips may lead to further delay or even prevent the transition process.

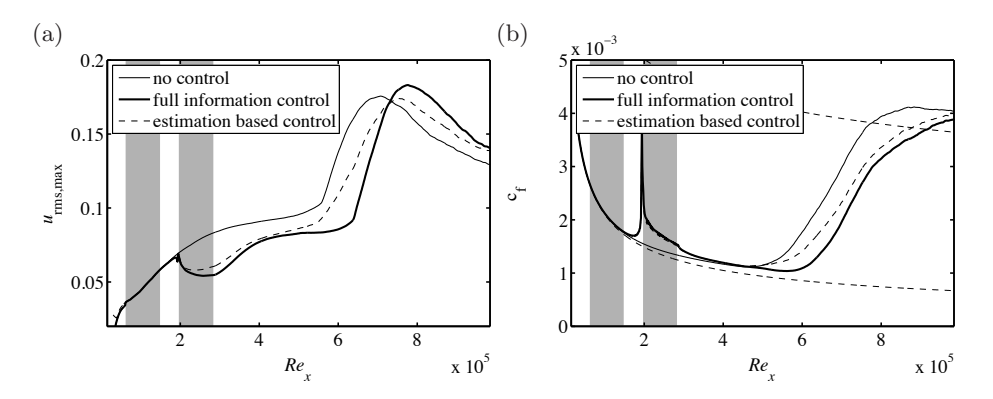


FIGURE 15. (a): Wall normal maximum u_{rms} ; (b): skin friction coefficient c_f . No control, ——; Full information control, ——; Compensator, ----.

In figure 16, wall-normal profiles of the rms value of the streamwise velocity perturbation are shown at different streamwise stations along the plate for the three cases under consideration. The reduction of streak amplitude is evident in the control region. Note also that where blowing/suction is applied the profiles feature a double-peak structure: the lowest peak closest to the wall is due to the local effect of the actuation, while the largest peak, representing the streak, is moved away from the wall. The changeover from laminar to turbulent streaks is occurring in the region $5\times 10^5 < Re_x < 7\times 10^5$. The typical profiles for $u_{\rm rms}$ of a turbulent boundary layer are observed at the end of the computational domain.

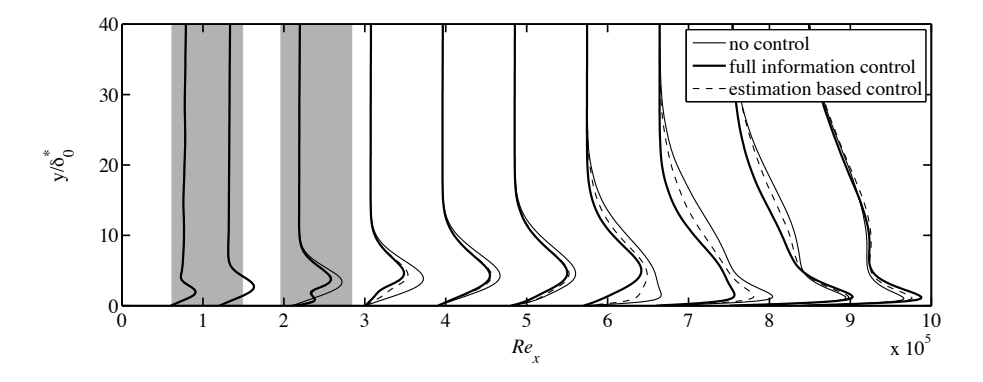


FIGURE 16. Wall normal profiles of $u_{\rm rms}$ at different streamwise positions $Re_x = [0.6, 1.2, 2.1, 3.0, 3.9, 4.8, 5.7, 6.6, 7.5, 8.4] \times 10^5$. The values of $u_{\rm rms}$ are scaled with 8.5×10^5 . No control, ——; Full information control, ——;

The production of turbulent kinetic energy $\overline{uv}\partial U/\partial y$ with the Reynolds shear stress \overline{uv} , is considered to characterise the effect of the blowing/suction at the wall. The wall-normal profiles of the turbulent production at two streamwise positions are displayed in figure 17. It can be seen that the turbulence production increases near the wall due to the blowing and suction while it decreases farther up in the boundary layer, attaining negative values at the beginning of the control region. In the compensator a reduction over the whole profile is observed as well as a small peak near the wall.

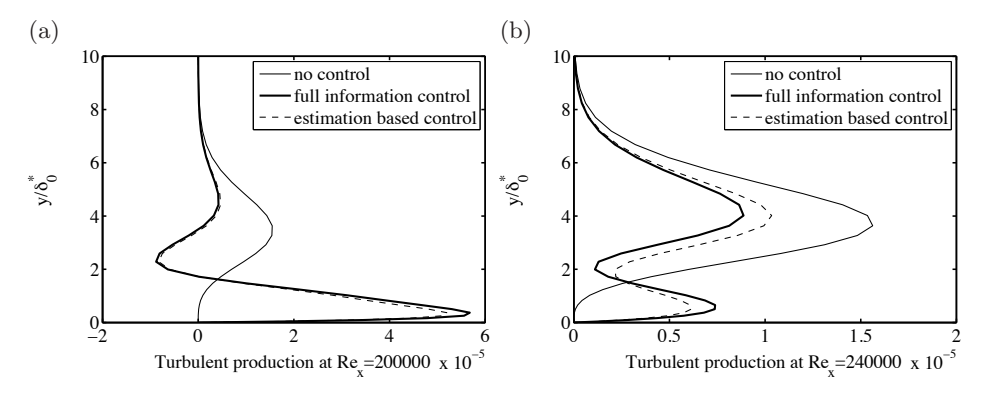


FIGURE 17. Wall normal profiles of turbulent production at (a) $Re_x = 2.0 \times 10^5$ and (b) $Re_x = 2.4 \times 10^5$. No control, —; Full information control, —; Compensator, ----.

In order to study the performance of the control for higher streak amplitudes, simulations with turbulence intensity Tu=4.0% are also performed. Owing to the larger turbulence intensity the growth of the streaks is faster, the transition location is moved upstream and the amplitude of the streaks within the control region are further increased. Overall, the performance of the estimation is as in the case presented above, while the extension of the transition delay is reduced. Even though the growth of the streaks is reduced in the control region, the regeneration downstream is more rapid at this higher free-stream turbulence levels. As shown by Barri (2006), for the control to be more effective, maybe the actuation region should be placed further upstream.

From this project it was desiphed that transision delay can

5. Conclusions

Numerical simulations of the transition to turbulence occurring in a flat-plate boundary-layer flow subjected to high levels of free-stream turbulence are performed. This scenario, denoted bypass transition, is characterised by the non-modal growth of streamwise elongated disturbances, so-called streaks. When these streaks reach large enough amplitudes, breakdown into turbulent spots occurs via their secondary instability. The scenario under consideration is highly intermittent in nature, i.e. streaks appear randomly in the boundary

layer, and therefore large computational domains and long integration times are needed to obtain converged statistical data.

In order to reduce the computational cost, mostly large-eddy simulations are performed. The ADM-RT subgrid-scale model is shown to be particularly suited for transitional flows: It is thoroughly validated before examining the effect on the transition process. The results indicate that the details of the streak breakdown can and need to be captured by LES. The high-frequency oscillations of the elongated streaks appearing as spot precursors define the grid size on which the LES can be performed. The reduction in terms of number of degrees of freedom compared to a full DNS is of the order of 10, while the computational cost is reduced about 50 times.

Linear model-based feedback control is applied in order to delay transition, where the linear parallel Orr-Sommerfeld/Squire system is used to design the estimation and control laws. The method presented here was previously developed by Hoepffner $et\ al.\ (2005)$; Chevalier $et\ al.\ (2006,\ 2007a)$ and shown to be successful in damping linear and weakly nonlinear perturbation in a variety of wall-bounded shear flows. The method is now applied to flows with highly nonlinear behaviour.

In practical situations, the full flow field is usually not accessible. The control problem is therefore combined with an estimation procedure based on wall measurements, the two wall-parallel components of the wall-shear stress and the pressure at the wall being considered here. It is found that to achieve an accurate estimation most of the confidence should be put in the shear-stress data; the pressure measurements are in fact too affected by the high-level fluctuations in the free stream.

The results presented show that the control is able to reduce the energy of the streaks, which are responsible, through their secondary instabilities, for the considered bypass-transition scenario and thus delay the whole process. The delay achieved is of order of the streamwise extent of the area where control is applied. For turbomachinery applications, this amounts to about 15-20% of the length of a typical turbine blade, resulting in a reduction of the total friction drag of 5-10%. The control performance is limited by the fast growth of the streaks just downstream of the region where blowing and suction is applied. This recovery is similar to that observed when control of turbulent flow is investigated and it can be explained by considering the action of the control in these highly disturbed flow: When blowing/suction is applied, the streamwise streaks are quenched close to the wall while the upper part of the boundary layer is less affected. As a consequence, as soon as the actuation is turned off, the streaks diffuse into the shear layer near the wall and can again be amplified. The relatively fast recovery of the streamwise streaks downstream of the control region was also observed in the recent experimental work by Lundell (2007). This author considers the same transition scenario but a different control strategy: reactive control is applied with sensors and actuators placed in a staggered manner. A more direct comparison between

the linear optimal control and the experiments appears therefore relevant and it is the object of new investigations.

The streamwise streaks can be estimated from wall measurements alone; however the structures occurring in the real flow are reproduced correctly mainly in the region where the measurements are taken. Downstream of this region the estimated field gradually diverges from the real field, revealing the importance of the continuous excitation of the boundary layer by the external free-stream turbulence (Westin et al. 1998). Control based on estimation (termed compensator) is therefore less effective than full information control. For actual implementations of feedback control the estimation process needs to be improved, in particular by reducing its cost. With this aim, two directions may be followed. First, model reduction can be introduced in the estimation problem. Global modes of the flow can be used for this, as global eigenmodes (Åkervik et al. 2007) or balanced POD modes (Rowley 2005). The model based on these two- or three-dimensional modes does not need to be linear, possibly improving the estimation performance for this type of flows. Alternatively, the relation between sensors and actuators may be deduced directly from flow measurements, relaxing the need for a flow model, as suggested e.g. by Lundell (2007). The latter option will be the object of future work, in the context of a closer interplay between experiments and simulations.

Acknowledgements

The authors wish to thank Mattias Chevalier, Espen Åkervik and Jérôme Hæpffner for many fruitful discussions. Computer time was provided by the Centre for Parallel Computing (PDC) at KTH, Stockholm. The present work is supported by the EOARD grant FA8655-04-1-3032 which is gratefully acknowledged.

References

- ÅKERVIK, E., HOEPFFNER, J., EHRENSTEIN, U. & HENNINGSON, D. S. 2007 Optimal growth, model reduction and control in a separated boundary-layer flow using global modes. *J. Fluid Mech.* **579**, 305–314.
- Andersson, P., Berggren, M. & Henningson, D. S. 1999 Optimal disturbances and bypass transition in boundary layers. *Phys. Fluids* 11, 134–150.
- Bagheri, S., Hoepffner, J., Schmid, P. J. & Henningson, D. S. 2007 Inputoutput analysis and control design applied to a linear model of spatially developing flows. *Appl. Mech. Rev.* Accepted.
- BARRI, M. 2006 Optimal contol of bypass transition in boundary layers. Master's thesis, KTH Mechanics, Stockholm, Sweden.
- BERGGREN, M. 1998 Numerical solution of a flow-control problem: vorticity reduction by dynamic boundary action. SIAM J. Sci. Comp. 19 (3), 829–860.
- Bewley, T., Temam, R. & Ziane, M. 2000 A general framework for robust control in fluid mechanics. *Physica D.* **138**, 360–392.
- Bewley, T. R. 2001 Flow control: New challenges for a new renaissance. *Prog. Aerosp. Sci.* 37, 21–58.
- Bewley, T. R., Moin, P. & Teman, R. 2001 DNS-based predictive control of turbulence: an optimal benchmark for feedback algorithms. *J. Fluid Mech.* 447, 179–295
- Bewley, T. R. & Protas, B. 2004 Skin friction and pressure: the 'footprints' of turbulence. *Physica D* **196**, 28–44.
- Brandt, L. 2007 Numerical studies of the instablity and breakdown of a boundary-layer low-speed streak. Eur. J. Mech./B Fluids 26 (1), 64–82.
- Brandt, L. & Henningson, D. S. 2002 Transition of streamwise streaks in zero-pressure-gradient boundary layers. *J. Fluid Mech.* 472, 229–262.
- Brandt, L. & Henningson, D. S. 2004 Linear feedback control of perturbations developing in a boundary layer under free-stream turbulence. In *Advances in Turbulence X, Proc. of the Tenth European Turbulence Conference* (ed. H. I. Andersson & P. Å. Krogstad), pp. 767–770. CIMNE.
- Brandt, L., Schlatter, P. & Henningson, D. S. 2004 Transition in boundary layers subject to free-stream turbulence. *J. Fluid Mech.* **517**, 167–198.
- Chevalier, M., Hoepffner, J., Åkervik, E. & Henningson, D. S. 2007a Linear feedback control and estimation applied to instabilities in spatially developing boundary layers. *J. Fluid Mech.* 588, 163–187, 167-187.
- Chevalier, M., Hoepffner, J., Bewley, T. R. & Henningson, D. S. 2006 State estimation in wall-bounded flow systems. Part 2. Turbulent flows. *J. Fluid Mech.* **552**, 167-187.
- Chevalier, M., Schlatter, P., Lundbladh, A. & Henningson, D. S. 2007b Simson: A pseudo-spectral solver for incompressible boundary layer flows. Technical Report KTH/MEK/TR-07/07–SE. KTH, Department of Mechanics, Stockholm.
- Collis, S., Chang, Y., Kellogg, S. & Prabhu, R. D. 2000 Large eddy simulation and turbulence control. *AIAA paper* (2000-2564).
- FARRELL, B. F. & IOANNOU, P. J. 1996 Turbulence suspension by active control. *Phys. Fluids* 8 (5), 1257–1268.

- FRIEDLAND, B. 1986 Control system design: An introduction to state-space methods. Mineola, New York: Dover.
- GROSCH, C. E. & SALWEN, H. 1978 The continuous spectrum of the Orr-Sommerfeld equation. Part 1. The spectrum and the eigenfunctions. J. Fluid Mech. 87, 33–54.
- Henningson, D. S. 1996 Comment on: "Transition in shear flows. Nonlinear normality versus non-normal linearity" [Phys. Fluids 7, 3060 (1995)]. *Phys. Fluid* 8 (8), 2257–2258.
- Hoepffner, J., Chevalier, M., Bewley, T. R. & Henningson, D. S. 2005 State estimation in wall-bounded flow systems. Part 1. Perturbed laminar flows. *J. Fluid Mech.* **534**, 263–294.
- HÖGBERG, M., BEWLEY, M. & HENNINGSON, D. S. 2003a Relaminarization of $Re_{\tau}=100$ turbulence using gain scheduling and linear state-feedback control. *Phys. Fluids* **15**, 3572–3575.
- HÖGBERG, M., BEWLEY, M. & HENNINGSON, D. S. 2003c Linear feedback control and estimation of transition in plane channel flow. J. Fluid Mech. 481, 149–175.
- HÖGBERG, M., CHEVALIER, M. & HENNINGSON, D. S. 2003b Linear compensator control of a pointsource induced perturbation in a Falkner-Skan-Cooke boundary layer. *Phys. Fluids* **15**, 2449–2452.
- HÖGBERG, M. & HENNINGSON, D. S. 2002 Linear optimal control applied to instabilities in spatially developing boundary layers. J. Fluid Mech. 470, 151–179.
- JACOBS, R. G. & DURBIN, P. A. 2001 Simulations of bypass transition. J. Fluid Mech. 428, 185–212.
- Joshi, S. S., Speyer, J. L. & Kim, J. 1995 Modeling and control of two dimensional poisuille flow. In 34th IEEE Conf on Decision and Control, pp. 921–927.
- Joslin, R. D. 1998 Aircraft laminar flow control. Annu. Rev. Fluid Mech. 30, 1-29.
- JOSLIN, R. D., ERLEBACHER, G. & HUSSAINI, M. Y. 1996 Active control of instabilities in laminar boundary layers-overview and concept validation. J. Fluids Eng. 118 (3), 494–497.
- JOSLIN, RONALD D., GUNZBURGER, MAX D. & NICOLAIDES, R. A. 1997 A self-contained automated methodology for optimal flow. AIAA J. 35 (5), 816–824.
- KAILATH, T. & HASSIBI, A. H. SAYED B. 2000 *Linear Estimation*. New Jersey: Prentice Hall.
- KARAMANOS, G.-S. & KARNIADAKIS, G. E. 2000 A spectral vanishing viscosity method for large-eddy simulations. *J. Comput. Phys.* **163**, 22–50.
- Kim, J. & Bewley, T. R. 2007 A linear systems approach to flow control. *Annu. Rev. Fluid Mech.* **38** (1), 383–417.
- Kim, J. & Lim, J. 2000 A linear process in wall-bounded turbulent shear flows. *Phys. Fluids* **12** (8), 1885–1888.
- LANDAHL, M. T. 1980 A note on an algebraic instability of inviscid parallel shear flows. J. Fluid Mech. 98, 243–251.
- Laurien, E. & Kleiser, L. 1989 Numerical simulation of boundary-layer transition and transition control. *J. Fluid Mech.* **199**, 403–440.
- Lewis, F. L. & Syrmos, V. L. 1995 Optimal Control. New York: Wiley-Interscience.
- Lundbladh, A., Berlin, S., Skote, M., Hildings, C., Choi, J., Kim, J. & Henningson, D. S. 1999 An efficient spectral method for simulation of incompressible flow over a flat plate. Technical Report KTH/MEK/TR-99/11-SE. KTH, Department of Mechanics, Stockholm.

- Lundell, F. 2007 Reactive control of transition induced by free-stream turbulence: an experimental demonstration. *J. Fluid Mech.* **585**, 41–71.
- Mans, J., de Lange, H. C. & van Steenhoven, A. A. 2007 Sinuous breakdown in a flat plate boundary layer exposed to free-stream turbulence. *Phys. Fluids* **19** (088101).
- MATSUBARA, M. & ALFREDSSON, P. H. 2001 Disturbance growth in boundary layers subjected to free stream turbulence. *J. Fluid. Mech.* 430, 149–168.
- METCALFE, R. W. 1994 Boundary layer control: A brief review. In Computational Fluid Dynamics '94, Invited lectures of the Second European CFD Conference; Stuttgart, Germany (ed. S. Wagner, J. Periaux & E. Hirschel), Progress in Astronautics and Aeronautics, pp. 52–60. John Wiley & Sons.
- Moin, P. & Bewley, T. 1994 Feedback control of turbulence. Appl. Mech. 47 (6), part 2, S3–S13.
- Moin, P. & Mahesh, K. 1998 Numerical simulation: A tool in turbulence research. *Annu. Rev. Fluid Mech.* **30**, 539–578.
- NORDSTRÖM, J., NORDIN, N. & HENNINGSON, D. S. 1999 The fringe region technique and the Fourier method used in the direct numerical simulation of spatially evolving viscous flows. SIAM J. Sci. Comp. 20, 1365–1393.
- REDDY, S. C. & HENNINGSON, D. S. 1993 Energy growth in viscous channel flows. J. Fluid Mech. 252, 209–238.
- ROBINSON, S. K. 1991 The kinematics of turbulent boundary layer structure. Tech. Rep. TM 103859. NASA.
- Rowley, C. W. 2005 Model reduction for fluids using balanced proper orthogonal decomposition. *Intl J. Bifurcation Chaos* **15** (3), 997–1013.
- SCHLATTER, P., STOLZ, S. & KLEISER, L. 2004 LES of transitional flows using the approximate deconvolution model. *Int. J. Heat Fluid Flow* **25** (3), 549–558.
- Schlatter, P., Stolz, S. & Kleiser, L. 2006a Analysis of the SGS energy budget for deconvolution- and relaxation-based models in channel flow. In *Direct and Large-Eddy Simulation VI* (ed. E. Lamballais, R. Friedrich, B. J. Geurts & O. Métais), pp. 135–142. Springer, Dordrecht, The Netherlands.
- Schlatter, P., Stolz, S. & Kleiser, L. 2006b LES of spatial transition in plane channel flow. J. Turbulence 7 (33), 1–24.
- Schmid, P. J. & Henningson, D. S. 2001 Stability and Transition in Shear Flows. New York: Springer.
- SEYED, M. M. 2007 Esimation and contol of bypass transition in the Blasius boundary layer. Master's thesis, KTH Mechanics, Stockholm, Sweden.
- Skogestad, S. & Postlethwaite, I. 2005 Multivariable feedback control, Analysis and Design, 2nd edition. West Sussex: Wiley.
- Stolz, S. & Adams, N. A. 1999 An approximate deconvolution procedure for large-eddy simulation. *Phys. Fluids* **11** (7), 1699–1701.
- Stolz, S., Adams, N. A. & Kleiser, L. 2001 An approximate deconvolution model for large–eddy simulation with application to incompressible wall–bounded flows. *Phys. Fluids* **13** (4), 997–1015.
- Thomas, A. S. W. 1983 The control of boundary-layer transition using a wave-superposition principle. *J. Fluid Mech.* **137**, 233–250.
- THOMAS, A. S. W. 1990 Active wave control of boundary-layer transition. In *Viscous Drag Reduction in Boundary Layers* (ed. D. M. Bushnell & J. N. Hefner),

- $Progress\ in\ Astronautics\ and\ Aeronautics,$ vol. 123. Washington D.C.: American Institute of Aeronautics and Astronautics.
- Westin, K. J. A., Bakchinov, A. A., Kozlov, V. V. & Alfredsson, P. H. 1998 Experiments on localized disturbances in a flat plate boundary layer. Part 1: the receptivity and evolution of a localized free stream disturbance. *Eur. J. Mech.* B/Fluids 17, 823–846.

Paper 5

5

Feedback Control of Boundary Layer Bypass Transition: Comparison of a numerical study with experiments

By Antonios Monokrousos, Fredrik Lundell & Luca Brandt

Linné Flow Centre, Department of Mechanics Royal Institute of Technology, SE-100 44 Stockholm, Sweden

AIAA Journal, 48 (8), 1848-1851, 2010

Two examples of experimental and numerical work on active control of transition induced by free-stream turbulence is reviewed and two extensions to previous work are reported. Previously, an experimental setup with upstream sensors and downstream actuators has been built. It has been demonstrated that an ad-hoc control algorithm is able to give a considerable attenuation of the disturbance amplitude downstream of the actuators. Furthermore, large-eddy simulations (LES) of optimal feedback control have been performed for a similar flow configuration. In the LES study, disturbance attenuation as well as transition delay have been obtained. Here, the numerical and experimenta efforts are used by side. First, an effort is made to match the disturbance behavior in the experimental flow case and in the LES. Control is applied in simulations of the matched system aiming at approaching the type of actuation used in the experiments (localized suction). The control law is still computed as optimal feedback of the linear system. As the actuation ability approaches the experiments, so does the control effect.

1. Introduction

1.1. Objective and outline

Feedback manipulation (or control) of flows aiming to reduce the friction drag is a promising way of using the knowledge and predicting ability provided by supercomputers in the last decades. In order to go from computer simulations to physical experiments, it is not sufficient to reproduce a physical configuration. It is also necessary to use (and possible model) sensors and actuators. A general review on the application of control theory to fluid dynamics is given in Ref. . Studies on the application of model-based linear feedback control have shown possibilities to delay transition. More recent efforts aim to build reduced-order models for the flow enabling fast computation of the control signal in large systems; .

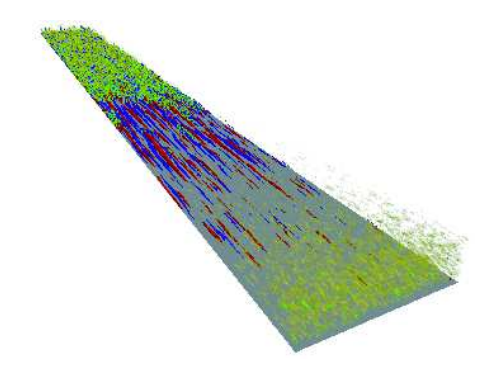


FIGURE 1. Visualisation of boundary layer transition induced by free-stream turbulence.

Numerical studies of flow control usually show a large potential whereas the experimental results are more modest. In this paper, however, we aim at bridging the gap between experiments and simulations. The flow case under study is bypass transition in a flat-plate boundary layer. We will first briefly introduce our previous experimental and numerical work. A LES (large-eddy simulation) will then be matched to the experiments and control is applied in the matched simulation. This work is performed in order to identify critical technologies (sensor, controller, actuator) and possible benefits.

1.2. Bypass transition

The term boundary layer bypass transition denotes transition scenarios where the dominant instability mechanism is not the exponential growth of two-dimensional Tollmien-Schlichting waves. The most common example is probably transition induced by high levels of free-stream turbulence (typically above 0.5-1% of the free-stream velocity). A visualisation of the process, taken from the present simulation, is shown in figure 1. Owing to the non-modal effect, elongated streamwise streaks are induced inside the boundary layer by streamwise vortices. This process is known as the lift-up effect . These streaks grow in strength and become susceptible to high-frequency secondary instabilities. These form localised regions of chaotic swirly motion, turbulent spots. Subsequently spots grow, merge and a fully-developed turbulent flow is observed.

1.3. Experimental demonstration of feedback control

An experimental demonstration of feedback control of bypass transition has been reported earlier. The data from this experiment will here be used as reference in a numerical study aiming at reproducing the disturbance conditions in the experiment as well as the control performance. A schematic of the experimental setup is shown in figure 2 (a). Free-stream turbulence was generated by a grid upstream of the plate and the velocity was measured by a hot wire traversed in the flow. One control unit is depicted in figure 2 (b). TuTurbulence

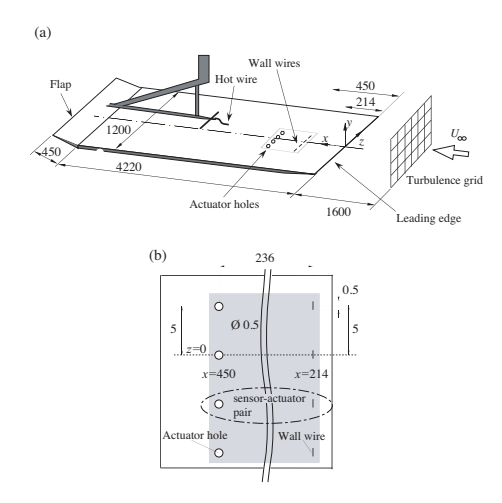


FIGURE 2. (a) Setup and (b) close up of a control unit. Measures are in mm.

intensity xDistance from the leading edge Variations of the streamwise wall shear stress were measured by the upstream wall wires. Control suction through the actuator holes was turned on (with a time delay to account for the disturbance propagation downstream) during periods when the shear was below a preset threshold. The effect of the control is measured by studying the attenuation of the maximum of u_{rms} at different positions. The disturbance attenuation is quantified as

$$\Omega_{rms} = 1 - \frac{u_{rms,max,on}}{u_{rms,max,off}},\tag{1}$$

so that Ω_{rms} is the relative decrease of the disturbance level in the boundary layer due to the control.

 Ω_{rms} Disturbance attenuation due to the control $u_{rms,max}$ Wall-normal maximum of the rms value of the streamwise disturbance velocity

2. Numerical simulations of feedback control

This transition scenario was simulated using direct numerical simulations (DNS) and large-eddy simulations (LES). A thorough study on different LES models was performed and the ADM-RT sub-grid-scale model turned out to be particularly suited for this transitional flow. The simulation code employed uses Fourier representation in the streamwise and spanwise directions and Chebyshev polynomials in the wall-normal direction. Resolution and domain size are reported in table 1.

A linear feedback control scheme was employed in order to reduce the disturbance growth and consequently delay transition. The case of bypass transition represents an extension of the linear approach to flows characterised by strong nonlinearities. Control was applied by distributed blowing and suction

TABLE 1. Computational box used. Resolution and box dimensions are shown. The box dimensions include the fringe region and are non-dimensionalised with respect to the displacement thickness δ_0^* at the inflow $(Re_{\delta_0^*} = 300)$

$\overline{L_x \times L_y \times L_z}$	$N_x \times N_y \times N_z$
δ_0^*	(resolution)
$2250 \times 60 \times 96$	$576 \times 121 \times 64$

at a portion of the wall. Initially, the control signal was based on the full knowledge of the instantaneous velocity field (i.e. full information control). In order to relax this unphysical requirement possible only in a numerical simulation, an estimator based on wall measurements was built.

Both the full information controller and the estimator are derived within the Linear Quadratic Gaussian (LQG) framework where a Linear Quadratic Regulator (LQR) is combined with a Kalman filter. The boundary layer flow is modelled by the Orr-Sommerfeld and Squire system governing the evolution of perturbations in parallel flows. The objective is to minimise the kinetic energy of the perturbations.

The results showed that the control was able to delay the growth of the streaks in the region where it is active. The flow field can be estimated from wall measurements alone: the structures occurring in the "real" flow are reproduced correctly in the region where the measurements are taken. Downstream of this region the estimated field gradually diverges from the "real" flow, revealing the importance of the continuous excitation of the boundary layer by the external stochastic free-stream turbulence. Control based on estimation, termed compensator, was able to delay transition but less effective than the full information control.

3. Matching of LES and experiments

In the following we will attempt to apply the control strategy described in the previous section to a numerical simulation that resembles the experimental conditions with Tu = 2.5%. Once agreement in the disturbance development has been achieved, we will limit the actuation in the simulation to approach the physical characteristics of the control implemented in the experiment.

3.1. Matching of the disturbance growth without control

 δ_0^* Displacement thickness at the inflow ReReynolds number

The first task is to set up a numerical simulation of the flow that reproduces as close as possible the actual flow of the experiment. However, there are restrictions that make a perfect matching with the experiment virtually impossible. The two main differences are that (i) the code we employ can not include

the leading edge and therefore perturbations cannot penetrate the boundary layer directly furthest upstream and (ii) the size of the computational domain is smaller than the wind-tunnel test section and therefore only free-stream turbulence with shorter integral length scale can be simulated. The difference in length scales causes different decay rates of the external turbulence and thus different effects upon the underlying boundary layer. However, a wider computational domain would make the simulations too time-consuming and the extensive parameter studies reported here would not be feasible. Thus we are aiming at a simulation that reproduces the main features of the experimental data in terms of disturbance growth and subsequent transition. An exact match is not possible due to the differences mentioned detailed above.

The matching is performed by varying the turbulence intensity and the integral length scale of the inlet free-stream turbulence and compare the growth of the wall-normal maximum of the streamwise velocity $u_{rms,max}$. We tried seven different length scales $l/\delta_0^*=2.5,\ 3.5,\ 4.5,\ 5.5,\ 6.5,\ 7.5,\ 8.5$ and three turbulence intensities at the inlet, $Tu=3,\ 3.5,\ 4\%$.

From figure 3 we see that the case with Tu = 3.5% and $l = 4.5\delta_0^*$ is closest to the experiment in terms of initial growth and transition location and this is our reference case below. The parametric study confirms that transition is enhanced when increasing the turbulence intensity and the integral length scale of the turbulence (owing to slower decay). The turbulence level matching the experimental data is therefore considerable higher than in the experiments.

3.2. Optimal control

In this study we are interested in the difference between distributed and localised actuation and in the effect of suction only; we therefore neglect the estimation problem and only consider the full-information control. The time-and-space varying control suction/blowing is applied in a stripe from $x=350\delta_0^*$ to $x=550\delta_0^*$. In the figures to come, the uncontrolled reference case is shown with blue and the full-information, full-actuation controlled case is shown with green. The green line can indeed be seen as the best possible performance we could achieve by tuning different control parameters (penalty in wave-number space) and is thus our control reference case. Experimental data is shown as dashed lines.

At this point it is useful to recall the differences between the actuator in the experiment and in the simulations. These pertain (i) the way the control signal is calculated and (ii) the area over which control is applied. In the experiment opposition control is adopted where the (preset) suction velocity and the time delay between the sensor and the actuator are varied. In the LES an optimisation of the distributed and modulated control action is performed and no further tuning is required. Note however that the control signal is computed assuming linearly evolving disturbances and parallel base flow. Secondly, it should be mentioned that the control is active over a large area of the plate where relatively weak blowing/suction is applied in the case of the numerical

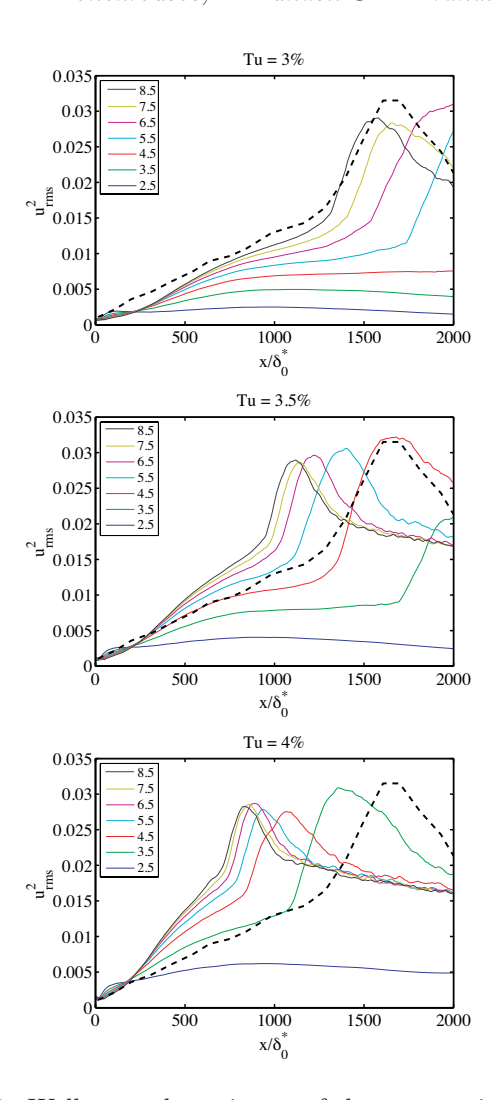


FIGURE 3. Wall-normal maximum of the streamwise velocity fluctuations u_{rms} . Levels of turbulence intensity from top to bottom: 3%, 3.5% and 4%. Each line on the plots to corresponds to a predefined integral length scale of the free-stream turbulence at the inlet. The legend shows the length scale in δ_0^* units. The dashed black line indicates the experimental data.

simulations. On the contrary, small holes with strong suction velocity are used in the experiment. Further, in the LES we apply control over the full spanwise width of the domain while in the experiment the control units are positioned

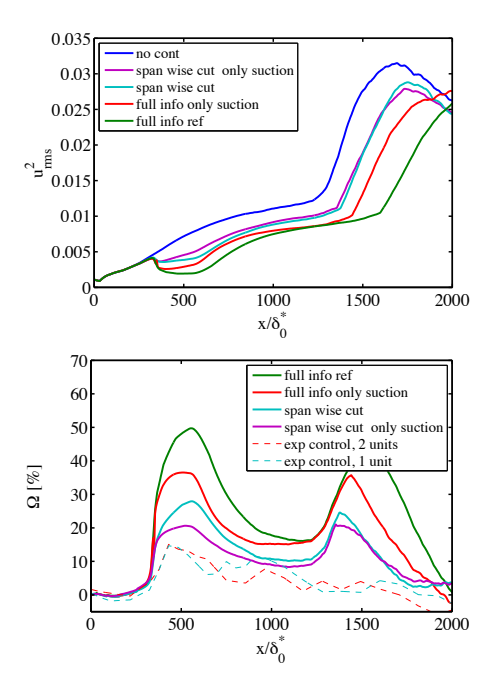


FIGURE 4. Control effect as a function of streamwise distance. Solid lines are simulations: blue: reference case, green line: control reference case, red line: control with only suction case, light blue: control with spanwise cut , purple: control with only suction and spanwise cut. Dashed lines as before. Top: wall-normal maximum of u_{rms} . Bottom: disturbance attenuation Ω .

near the middle of the plate and have a spanwise width of about 20 mm through four discrete 0.5 mm holes (for each control unit).

We will now try to wind down these differences. The control strategy in terms of the way the control signal is calculated will not be changed. Instead, we will focus on the geometrical/functioning aspects of the actuator itself. The following restrictions will be used alone or in combination: (i) apply only suction, (ii) restrict the area of actuation to spanwise strips, (iii) decrease the streamwise extension of the area where suction is applied ad increase the maximum suction amplitude. The amplitude increase is obtained by decreasing the cost of the control in the overall cost function (referred to as a "cheaper" control).

In figure 4 we see three cases where the actuation characteristics are varied. In particular, we first keep the actuation area the same but remove all the blowing while maintaining the suction unchanged (red line in the figure); second we keep the blowing and suction unchanged but apply it only in spanwise areas of width $5\delta_0^*$ (light blue line) with a centre-to-centre distance of $10\delta_0^*$; finally we

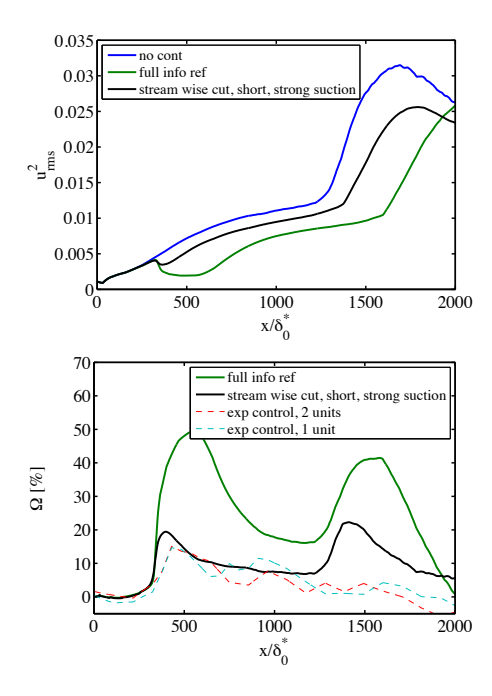


FIGURE 5. Control effect as a function of streamwise distance. Solid lines are simulations: blue: reference case, green line: control reference case, black line: control with only suction, spanwise and streamwise cut and stronger maximum suction (cheaper control). Dashed lines as before. Top: wall-normal maximum of u_{rms} . Bottom: disturbance attenuation Ω .

combine the two cases above applying only suction and cutting the signal in the spanwise direction (purple line). We see that the performance of the control in the LES is gradually degrading, approaching the experimental results. However a certain delay in the transition location remains.

l^2 Control penalty

In figure 5 we see the results from the simulation where all the previous restrictions on the actuator have been applied but also the streamwise extent of the control has been reduced from $200\delta_0^*$ to $20\delta_0^*$. Additionally we reduce the penalty put on the control during the design process from $l^2=10$ to $l^2=2$ (see Ref.) resulting in stronger suction. In this last case the control effect is almost the same for both the experiment and the simulation near the actuation region but downstream there is a delay of transition only in the numerical study. This can be explained by the fact that in the experiment control is applied near the middle of the plate and where transition occurs fully developed turbulence "invades" the controlled area from the uncontrolled sides.

4. Conclusions

Feedback control of bypass transition has been studied. One experimental (suction through holes triggered by the varying wall shear stress via threshold and delay) and one numerical (LQR with and without Kalman filter estimation) study are described. A simulation giving a similar development of the disturbance amplitude as the experiment has been obtained and the LQR has been applied to this simulation.

- 1. The LQR with time and space varying blowing/suction gives much larger initial disturbance attenuation than the experiments (55% as compared to 15%) and a considerable transition delay.
- 2. The initial disturbance attenuation in the simulations approaches the one obtained in the experiments if the capability of the actuator coupled to the LQR is limited towards the ability of the experimental ones (by (i) using only suction, (ii) limiting the actuation to limited spanwise positions and (iii) decreasing the streamwise length of the actuation stripe).
- 3. Compared to the case with complete actuation, a smaller, but still distinct, transition delay is obtained as the actuation ability is decreased.

Based on these observations, we find it plausible that an experiment in which the full span of the wind tunnel was controlled, would produce a transition delay. The results clearly indicate the importance of a good model for the actuators. This enables us to extract relevant information on the performance of the control from numerical simulations.

Acknowledgements

This work has relied on inspiration and support from professor D. S. Henningson and professor P. H. Alfredsson at KTH Mechanics. Financial support has been received from the Swedish Research Council.

References

- Kim, J. and Bewley, T.R. A Linear Systems Approach to Flow Control, Ann. Rev. Fluid Mech., 2007, 39, 383-417.
- Chevalier, M., Hoepffner, J., Åkervik E. and Henningson, D. S. Linear feedback control and estimation applied to instabilities in spatially developing boundary layers, J. Fluid Mech., 2007, 588, 163-187.
- Rowley, C. W. Model reduction for fluids using balanced proper orthogonal decomposition Int. J. Bifurcation Chaos Appl. Sci. Eng., 2005, 15, 997
- Bagheri, S., Åkervik, E., Brandt, L. and Henningson, D.S. Matrix-Free Methods for the Stability and Control of Boundary Layers AIAA Journal, 2009, 47(5), 1057-1068
- Lundell F. Reactive control of transition induced by free-stream turbulence: an experimental demonstration, J. Fluid Mech., 2007, 585, 41-71.
- Monokrousos, A., Brandt, L., Schlatter, P. and Henningson, D.S. *DNS and LES of estimation and control of transition in boundary layers subject to free-stream turbulence*, Int. J. Heat and Fluid Flow, 2008, 29, 841-855.
- Matsubara, M. and Alfredsson, P. H. Disturbance growth in boundary layers subjected to free stream turbulence, J. Fluid. Mech., 2001, 430, 149-168.
- Landahl, M. T. A note on an algebraic instability of inviscid parallel shear flows, J. Fluid Mech., 1980, 98, 243-251.
- Brandt, L., Schlatter, P. and Henningson, D. S. Transition in boundary layers subject to free-stream turbulence J. Fluid Mech., 517, 2004, 167-198.
- Chevalier, M., Schlatter, P., Lundbladh, A. and Henningson, D. S. SIMSON: A Pseudo-Spectral Solver for Incompressible Boundary Layer Flows, KTH Mechanics, Stockholm 2007, Technical Report, KTH/MEK/TR-07/07-SE
- Friedland, B. Control system design: An introduction to state-space methods, Dover, Mineola, New York, 1986.

Paper 6

Control of a separating boundary layer with travelling waves on the wall

By Antonios Monokrousos & Luca Brandt

Linné Flow Centre, Department of Mechanics Royal Institute of Technology, SE-100 44 Stockholm, Sweden

Technical report, 2011

We perform numerical simulations of control of a separating laminar boundary layer by means of blowing and suction at the wall in the form of traveling waves. Separation is imposed by prescribing accelerating and decelerating free-stream velocity for the flow over a flat plate. We find that downstream traveling waves already at very low amplitudes are able to eliminate the separation and induce a turbulent but attached boundary layer flow. Upstream traveling waves of relatively higher amplitudes only slightly reduce separation while keeping the flow laminar. The amplitude of the blowing/suction needed to achieve such significant effects are considerably smaller than those previously considered for drag reduction and transition delay in plane geometries.

1. Introduction

Understanding the flow around solid bodies is a challenging task due to its high complexity. The problem becomes substantially more complicated when we study living creatures that fly in the air or swim in the water. Both experiments and simulations are very difficult in this case. On the other hand, mimicking the solutions that nature has chosen has proven to give substantial improvement to similar engineering application on many instances.

One of the fluid mechanics problems of great potential applicability but still unsolved is related to fish swimming. In particular, we cannot explain the large gap between the estimated drag of the fish and the thrust it can provide, the latter estimated considering its muscle mass (Rome & Swank 1992; Rome et al. 1993; Coughlin et al. 1996). Indeed it has been calculated that a solid body with the form of a fish would experience a drag too large for it to move with the speeds that have been actually observed. This lead to the idea that the fish must have a way to reduce its drag, either its form drag by cancelling or delaying the separation or its friction drag by re-laminarising the boundary layer close to the skin, or probably both. The potential benefits from using some similar technique in man-made vehicles would be enormous. The concept of actively modifying the flow in order to have some gain is known as flow control.

Some of the hypotheses suggested to explain the reduced drag are body shape (Wehrmann 1965), flexible skin (Landahl 1962), active skin (Kendall 1970), riblets (Walsh 1982), to mention few. Active skin can be modelled as small amplitude waves at the wall, much smaller than the boundary layer thickness. In the case of flexible skin the wave amplitude is much larger than the boundary layer (Taneda & Tomonari 1974; Anderson et al. 2001).

In this study, we apply blowing and suction at the wall in the form of upstream and downstream traveling waves and observe whether and how we can modify laminar separation in a boundary-layer flow. Recent investigations indicate that sensorless (open-loop) control of transition to turbulence and drag reduction in turbulent flows is a feasible option. Inspired by the investigations of Min et al. (2006), the influence on turbulent channel flow of traveling waves induced at the wall by blowing/suction has been studied theoretically and by means of numerical simulations. In the original publication by Min et al. (2006) blowing/suction at the wall in the form of upstream traveling waves are applied in a turbulent channel flow. Their two- and three-dimensional numerical simulations show that upstream traveling waves in turbulent channel flow reduce the average friction coefficient to a (sub-)laminar level. This is explained by the extra pumping provided by the wall-actuation (Hoepffner & Fukagata 2009), leading to negative power savings for the proposed strategy. Recently, Bewley (2009) has theoretically shown that for any boundary control, the power exerted at the walls is always larger than the power saved by reducing to sub-laminar drag. The net power gain is therefore always negative if the uncontrolled flow is laminar. However, a positive gain can be achieved when the uncontrolled flow becomes turbulent but the controlled flow remains laminar. The conclusion drawn in the complete analysis by Moarref & Jovanović (2010); Lieu et al. (2010) is that the optimal control solution is to relaminarize the flow and transition control a viable approach. To this aim, control in the form of downstream-traveling waves is more promising as we show here and as previously suggested also by Lee et al. (2008). These authors examine the linear stability of channel flow modulated by upstream-traveling and downstreamtraveling waves and show that downstream traveling waves can have stabilizing effect on the flow, while upstream-traveling waves are destabilizing. It is now understood that the physical mechanisms behind travelling waves in channels with moving walls and waves of blowing and suction are rather different. In particular the moving walls are producing streaming near the wall in the same direction of the travelling waves while in the case of actuation by blowing and suction, flow is induced in the opposite direction (see Hoepffner & Fukagata 2009).

A logical extension of the upstream-traveling and downstream-traveling waves is the application of spanwise-traveling, blowing-and-suction waves. These waves sustain streaky structures which are not optimal for transition or to sustain turbulence and could thus reduce the drag. Du & Karniadakis (2000) showed drag reduction for spanstream-traveling waves in turbulent channel flow

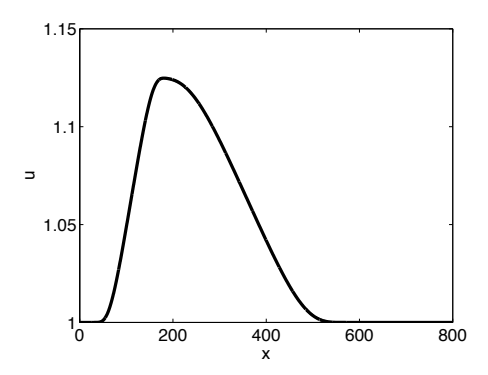


FIGURE 1. Stream-wise velocity, imposed at the top boundary, at $y = 60\delta_0^*$ versus the streamwise coordinate x, also in units of δ_0^* , the boundary layer thickness at the inflow.

using volume forcing. More recently, Quadrio et al. (2009) examined the drag reduction in turbulent channel flow by wall actuation in the form of streamwise traveling waves of spanwise velocity perturbations. In these investigations a more feasible actuation is considered.

The effect on boundary-layer transition of traveling waves induced at the wall by blowing/suction over a finite length region is studied numerically in de Lange & Brandt (2010). Up- and downstream traveling waves are applied over a limited wall-region in an attempt to reduce the friction drag of boundary layer flows subjected to high-levels of free-stream turbulence (4.7%). It is found that the introduction of upstream traveling waves promotes the transition. On the other hand, downstream traveling waves can be used to delay transition and reduce the drag. For moderate wave amplitudes, it is observed that turbulent production is damped.

None of the previous studies considered the effect on a separating flow, such as a boundary layer exposed to adverse pressure gradient. Here we carry out numerical simulations as a first attempt to anticipate and capture some of the essential dynamics of a separating flow on a flat plate when control is applied at the wall; hence far from a realistic model for active skin. However, we also hope to identify some potential benefits for engineering type of flows where our model could be closer to realistic implementations.

2. Flow configuration

2.1. Free-stream bounary condition

We consider a flat plate with the Blasius boundary layer as inflow profile and impose a varying pressure gradient by prescribing the velocity at the top boundary via a Dirichlet boundary condition. The streamwise dependence of the free-stream velocity is shown in figure 1. Initially, the slow increase of the velocity implies an accelerated boundary layer, followed by a fast decrease downstream,

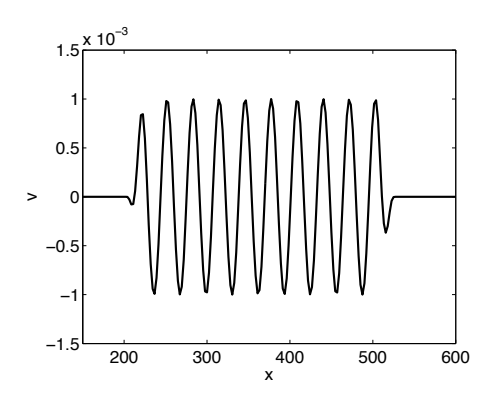


FIGURE 2. Wall-normal velocity, imposed at the wall in order to control the boundary, at $y = 60\delta_0^*$.

associated to deceleration. The accelerated-decelerated boundary layer is used here as a model for the flow around an obstacle with a curved solid surface. The external pressure distribution applied on the laminar boundary layer leads to unsteady separation and a recirculation bubble. The strong shear region generated between the back flow and the separated boundary layer becomes unstable and shedding is observed downstream. An instantaneous visualization of the flow is reported in figure 3a). The Reynolds number at the inflow is $Re_{\delta_0^*} = \frac{U_0^\infty \delta_0^*}{\nu} = 400$, based on the inflow free-stream velocity U_0^∞ , inflow displacement thickness δ_0^* and kinematic viscosity ν . Even though it is a relatively low Reynolds number, the flow is globally unstable due to the separated region. Nevertheless, we add a small amount ($\sim 1\%$) of free-stream turbulence in order to better model a realistic flow environment where the background flow is never fully laminar.

2.2. Wall actuation

Blowing and suction is applied in the form of travelling waves at the wall. The wall-normal velocity at the boundary is defined as

$$v(y = 0, t) = \phi f(x) \cos \alpha (x - ct) = \phi f(x) \cos(\alpha x - \omega t), \tag{1}$$

where f a smooth function rising from 0 to 1 in the control region, $\alpha = \frac{2\pi}{\lambda_x}$ the streamwise wavenumber of the actuation. In figure 2 we show the wall-normal velocity at the wall to document the wave-like behavior as well as the smooth ramping. For the results presented here control is applied for a finite length, 200 < x < 500, corresponding to the region of decelerating free-stream velocity and separated flow, (see fig. 3a). We consider both downstream-traveling and upstream-travelling waves, differing for the sign of the phase speed c.

The type of the control is open-loop; we run through the available parameters to find an optimal choice. In this case we have as control parameters the wavenumber (α) , temporal frequency (ω) and amplitude (ϕ) of the wave, with

the phase speed defined as $c=\frac{\omega}{\alpha}$. We note that the phenomenon is strongly non-linear and unsteady thus it is very difficult to a priory guess the correct parameters. The flow is fully three dimensional, however there is no mean spanwise component hence we only considered two dimensional waves i.e. zero spanwise wavenumber.

2.3. Simulation parameters

The numerical code employed is based on a pseudo-spectral method and it is described in detail in Chevalier et al. (2007). The algorithm uses Fourier representation in the streamwise and spanwise directions and Chebyshev polynomials in the wall-normal direction. To correctly account for the downstream boundary layer growth a spatial technique is necessary. This requirement is combined with the periodic boundary condition in the streamwise direction by the implementation of a "fringe region". In this region, the flow is smoothly forced to the prescribed inflow velocity vector. This is normally a boundary layer profile, but can also contain a disturbance.

The simulation is a well resolved large eddy simulation with the ADM-RT subgrid-scale model (Schlatter et al. 2006a, b). The dimensions of the computational box are $1200 \times 60 \times 50$ in units of δ_0^* in the streamwise, wall-normal and spanwise directions. The resolution is 512×48 Fourier modes in the streamwise and spanwise directions and 121 Chebyshev polynomials in the wall-normal direction. Free-stream turbulence is forced at the inflow by a superposition of modes of the continuous spectra of the Orr-Sommerfeld and Squire operators. See Brandt et al. (2004); Monokrousos et al. (2008) for further details.

3. Results

We will show here that downstream-traveling waves can be used to delay or cancel separation of the boundary layer while the upstream-traveling waves are suitable to attenuate the shedding produced by the shear layer associated with the re-circulation bubble, thus delay the transition or even fully re-laminarise the flow. In order to evaluate the efficiency of the control, we run the simulations for long time and gather statistics by averaging in time and in the homogeneous spanwise direction. We first run without any wall actuation until a fully developed separating flow is established and then we turn on the control. We start to collect statistics after 3000 time units the control has been active, when all the transient effects have been washed away. Typically we collect statistics for about 15000 time units.

We display instantaneous flow visualizations pertaining to the uncontrolled case and to two of the most characteristic results obtained for downstream and upstream traveling waves in figure 3. From these instantaneous pictures we observe already a very distinct behavior for the two types of actuation considered. The downstream-traveling waves promote transition but eliminate the separation thus leading to a reduction to the form drag in the case of bluff

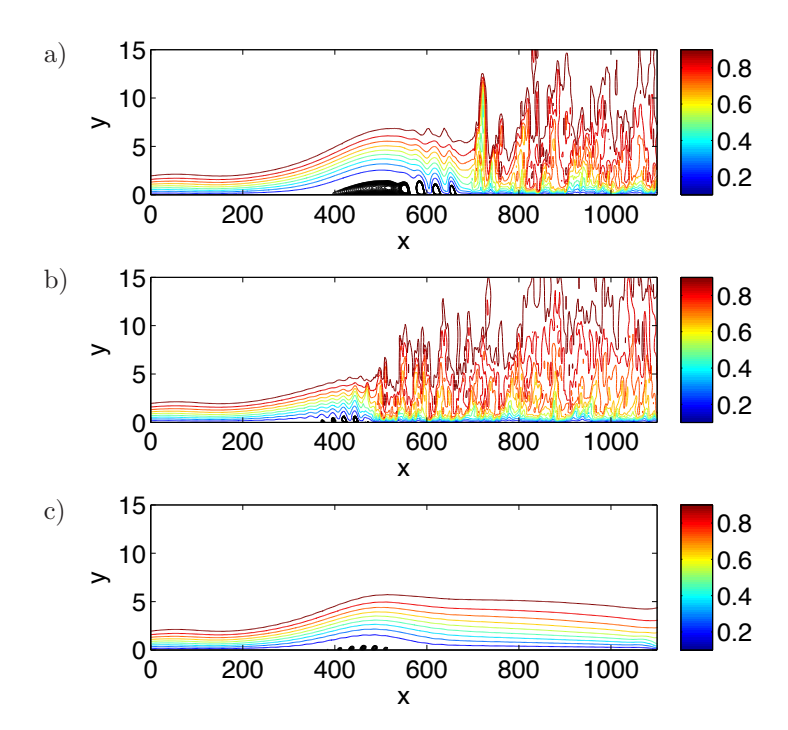


FIGURE 3. Flow visualisation of (a) the uncontrolled flow and the controlled flow with (b) downstream ($\phi = 5 \times 10^{-5}$, $\alpha = 0.25$, $\omega = 0.08$) and (c) upstream ($\phi = 3 \times 10^{-2}$, $\alpha = 0.35$, $\omega = 0.2$) traveling waves. The streamwise velocity component is shown. The black isocontours mark negative velocities implying the existence of a back-flow.

bodies; the upstream-traveling waves still may reduce the separation but mainly eliminate the shedding (turbulent wake) leading a reduction in the friction drag.

The mean flow for the cases considered above is displayed in figure 4. The results confirm the impression given in figure 3. Re-attachment is triggered by downstream-traveling waves while upstream-traveling waves delay transition. A thicker boundary layer is seen in the case of downstream waves, while the slower growth of the boundary-layer thickness in the case of upstream waves documents the transition delay (lower mixing).

To quantify the efficiency of the control, we introduce two different criteria. The first relates to the effect on the separation and the length of the recirculation bubble. We consider the integral of the mean streamwise velocity \tilde{U} along a plane near the wall (y=0.01) taken only over negative values

$$S_s = \int_{x_1}^{x_2} \tilde{U}(x, y)|_{y=0.01} dx \tag{2}$$

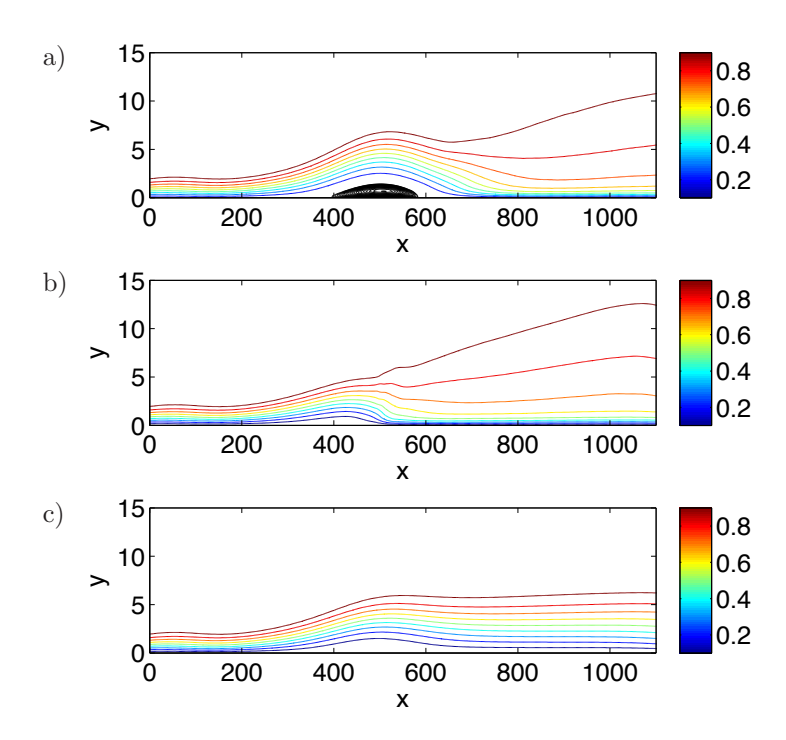


FIGURE 4. Mean streamwise velocity for (a) the uncontrolled flow and the controlled flow with (b) downstream ($\phi = 5 \times 10^{-5}$, $\alpha = 0.25$, $\omega = 0.08$) and (c) upstream ($\phi = 3 \times 10^{-2}$, $\alpha = 0.35$, $\omega = 0.2$) traveling waves.

where x_1 is the first location where \tilde{U} becomes negative and x_2 where it becomes positive again. When this integral is zero ($\tilde{U} > 0$ for all x) separation is suppressed and the control is considered successful. Note that larger negative values of \tilde{U} can be associated to higher bubbles.

The second criterion relates to delay of transition to turbulence. We choose the integral along the streamwise direction of the skin friction coefficient in the second half of the plate, where transition typically occurs for the uncontrolled case

$$S_t = \int_0^{L_x} c_f(x) dx. \tag{3}$$

In the expression above, c_f is the skin friction coefficient. In this case, lower values of S_t imply better control performance, laminar flow, although there is no strict bound in the value of S_t . However, typically values below 1 imply a laminar flow.

We first present results for downstream-traveling waves. After running several simulations varying the control parameters α , ω and ϕ , we find this

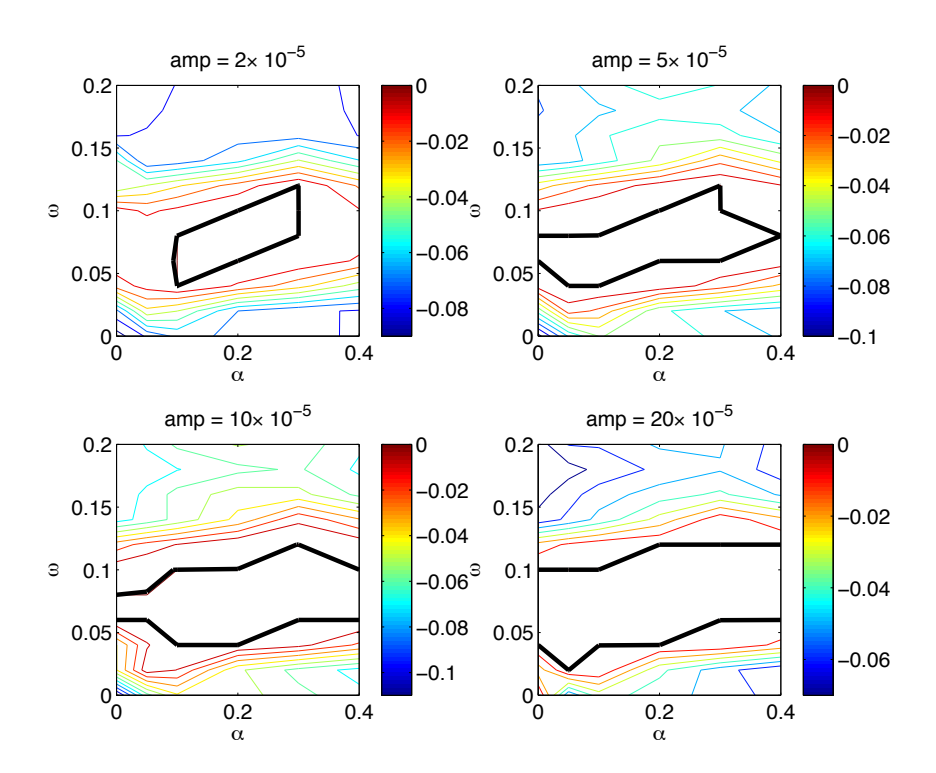


FIGURE 5. Isocontours of S_s , the control efficiency based on mitigation of the back-flow (negative streamwise velocity) near the wall. Longer and stronger separation appears as larger negative values, whereas no back-flow implies $S_s = 0$ and it is indicated by the black isocontours. Each subplot corresponds to different amplitudes of the wall waves, normalized by the free-stream velocity.

approach to be useful to reduce separation; hence we will display the results in terms of the observable S_s .

In figure 5 we plot isocontours of the control efficiency S_s for different amplitudes of the waves in the (α, ω) plane. The control is effective for almost all values of α tested but in a relatively narrow band of ω . We also note that the higher the amplitude, the broader the set of parameters for which we find that separation is suppressed. A snapshot of the instantaneous streamwise velocity for the case of control with downstream-traveling wavesis shown in figure 3b). As noted above, the control manages to completely eliminate the separation bubble by igniting a turbulent boundary layer, early on in the separated region. It is also important to note that the amplitude of the wall blowing and suction is relatively low, about 3 orders of magnitudes lower that that necessary to affect a zero-pressure-gradient transitional boundary layer. Indeed in de Lange

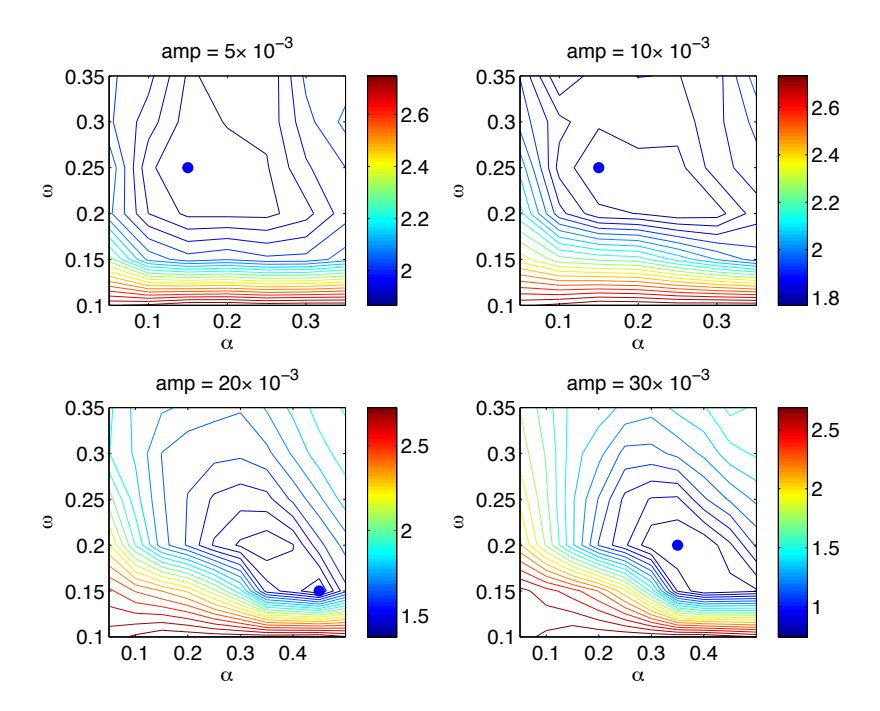


FIGURE 6. Isocontours of S_t , the control efficiency based on mitigating transition to turbulence (integrated skin friction coefficient). Lower values imply longer part of the domain with laminar flow. Values bellow 1 imply complete relaminarisation. The actuation amplitude is only in the wall-normal component and is normalised with the free stream velocity.

& Brandt (2010), the blowing and suction needed to delay the turbulence onset was 0.15.

The picture is rather different for upstream-traveling waves. In this case, the wall actuation do not significantly delay separation but rather cancel the shedding and re-laminarize the flow. In figure 6 we plot isocontours of the control efficiency S_t for different amplitudes of the upstream waves. First, notice that a larger amplitude is necessary for the control to have any effect. The flow stays laminar only for the highest amplitudes and a narrow band of α and ω . A snapshot of instantaneous streamwise velocity for the case of control with upstream-traveling waveswas reported in figure 3c), where a completely laminar flow is displayed. Note that it is not possible to argue that a laminar flow would be observed also for pressure gradients stronger than that considered here. However, based on our observations, we can speculate that higher amplitudes of the actuation would be necessary to delay transition when

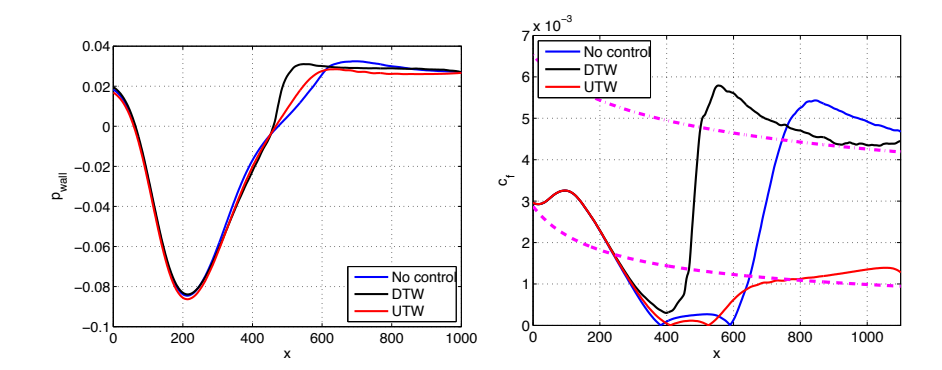


FIGURE 7. a) Mean pressure at the wall, and b) Skin-friction coefficient versus the streamwise location for best choice of downstream-traveling waves and upstream-traveling waves.

increasing the flow deceleration; above a certain threshold upstream-traveling waves would no more be able to keep the flow laminar.

Finally, we consider the two cases that, based on the two criteria introduced above, performed best. In particular, for downstream-traveling waves , when the separation was suppressed for a broad set of parameters and amplitudes, we choose the case of lowest amplitude since this implies the least effort, $\phi = 5 \times 10^{-5}$. The wave parameters are $\alpha = 0.25$ and $\omega = 0.08$. As concerns upstream-traveling waves where we may aim to delay transition, we will consider $\phi = 3 \times 10^{-2}$, $\alpha = 0.35$ and $\omega = 0.2$. These values have been chosen within the rather limited range of values for which the flow is kept laminar.

In figure 7 we plot the time-averaged pressure on the wall and skin friction coefficient for three cases: uncontrolled, controlled with downstream waves and controlled with upstream waves. Considering the pressure, we notice that the downstream waves are able to fully recover the pressure drop associated to separation. This suggests that the form drag associated to the lack of pressure recovery behind a bluff object would be reduced. Conversely, control by upstream waves leave the pressure recovery almost unchanged with respect to the uncontrolled case. The downstream waves strongly promote transition to turbulence as shown by the skin friction coefficient, while the upstream waves completely suppress it. Transition moves from $x \approx 700$ in the uncontrolled case to $x \approx 500$ when blowing/suction takes the form of downstream-traveling waves; the skin friction is still around laminar values for waves with negative phase speed. As a consequence, upstream-traveling waves can induce a reduction of friction drag around moving bodies.

To explain our observations on the effect of waves of blowing and suction on a separating laminar boundary layer we suggest the following. The separating flow is highly unstable and the presence of free-stream turbulence (background noise) triggers unstable modes which distort the laminar flow and induce shedding from the separation bubble. When adding disturbances in the form of downstream-traveling waves, we introduce weak disturbances of the right frequency to enhance and accelerate the transition process. Indeed, control is effective for a limited range of frequencies and the amplitudes of the actuation is very low. Downstream-traveling waves therefore increase time-dependent fluctuations and momentum mixing; the latter clearly affects separation.

The mechanisms is quite different when the control takes the form of upstream-traveling waves. First we observe a reduction of the recirculation length; together with the larger level of actuation this implies that the control alters the base flow by nonlinear effects. The upstream waves can be shown to create downstream streaming (Hoepffner & Fukagata 2009) and hence possibly to reduce the shear associated to the separation. This is causing the flow to be more stable.

4. Conclusions

We apply control on a separating laminar boundary layer in the form of traveling waves of blowing and suction at the wall. We perform a parametric analysis of the influence of the control parameters characterizing the waves (wavenumber, frequency and amplitude) as well as their direction (downstream and upstream).

We find that for specific values of the wave frequency the downstream-traveling waves are able to suppress separation. This may result into a potential reduction of the form drag for objects moving through a fluid even for very small amplitude of the waves. Our results suggest that the downstream-traveling waves in phase with naturally occurring instabilities, enhance the latter and trigger early transition. This, in turn, promotes faster re-attachment of the boundary layer. This effect could explain drag reduction associated to fish swimming (Triantafyllou et al. 2002).

On the other hand, control in the form of upstream-traveling waves is mitigating the instability arising in the shear layer associated to flow separation, such that laminar flow can be seen downstream of separation. For this control to work the wave amplitude needs to be much higher than the amplitudes used to suppress separation by downstream-traveling waves. The stabilizing effects is therefore most likely associated to modifications of the mean shear.

The reduction of skin friction associated to the stabilizing effect of upstream-traveling waves is probably less important than the reduction of form drag induced by the downstream-traveling waves. The latter strategy seems therefore more promising for application to moving bluff body. However, before any final conclusion on the practical feasibility of such a control approach can be drawn one needs to consider the effect of waves of blowing and suction on turbulence separation and on boundary layer with stronger pressure gradients. This is the object of current and future research.

Acknowledgements

We are grateful to Jerome Heopffner for fruitfull discussions. Computer time provided by SNIC (Swedish National Infrastructure Centre) is acknowledged.

References

- Anderson, E.J., McGillis, W.R. & Grosenbaugh, M.A. 2001 The boundary layer of swimming fish. *Journal of Experimental Biology* **204** (1), 81–102.
- Bewley, T. R. 2009 A fundamental limit on the balance of power in a transpiration-controlled channel flow. *J. Fluid Mech.* **632**, 442–446.
- Brandt, L., Schlatter, P. & Henningson, D. S. 2004 Transition in boundary layers subject to free-stream turbulence. *J. Fluid Mech.* **517**, 167–198.
- CHEVALIER, M., SCHLATTER, P., LUNDBLADH, A. & S., HENNINGSON D. 2007 A pseudo spectral solver for incompressible boundary layer flows. *Technical Report*, *Trita-Mek* 7.
- Coughlin, D.J., Zhang, G. & L.C., Rome 1996 Contraction dynamics and power production of pink muscle of the scup (stenotomus chrysops). *Journal of Experimental Biology* **199**, 2703–2712.
- Du, Y. & Karniadakis, G. E. 2000 Suppressing wall turbulence by means of transverse traveling wave. Science 288.
- Hoepffner, J. & Fukagata, K. 2009 Pumping or drag reduction? *Journal of Fluid Mechanics* **635**, 171–187.
- Kendall, James M. 1970 The turbulent boundary layer over a wall with progressive surface waves. *Journal of Fluid Mechanics* 41 (02), 259–281.
- Landahl, Marten T. 1962 On the stability of a laminar incompressible boundary layer over a flexible surface. *Journal of Fluid Mechanics* **13** (04), 609–632.
- DE LANGE, H. C. & Brandt, L. 2010 Drag reduction on external surfaces induced by wall waves. In *Direct and Large-Eddy Simulation DLES-8*, *Eindhoven University of Technology*.
- Lee, C., Min, T. & Kim, J. 2008 Stability of channel flow subject to wall blowing and suction in the form of a traveling wave. *Phys. Fluids* **20** (101513).
- LIEU, B., MOARREF, R. & JOVANOVIĆ, M. R. 2010 Controlling the onset of turbulence by streamwise traveling waves. Part 2: Direct numerical simulations. *J. Fluid Mech.* **663**, 100–119.
- MIN, T., KANG, S.M., SPEYER, J. L. & KIM, J. 2006 Sustained sub-laminar drag in a fully developed channel flow. J. Fluid Mech. 558, 309–318.
- MOARREF, R. & JOVANOVIĆ, M. R. 2010 Controlling the onset of turbulence by streamwise traveling waves. Part 1: Receptivity analysis. *J. Fluid Mech.* **663**, 70–99.
- Monokrousos, A., Brandt, L., Schlatter, P. & Henningson, D. S. 2008 DNS and LES of estimation and control of transition in boundary layers subject to free-stream turbulence. *Int. J. Heat Fluid Flow* **29** (3), 841–855.
- Quadrio, M., Ricco, P. & Viotti, C. 2009 Streamwise-traveling waves of spanwise wall velocity in a turbulent channel flow. *J. Fluid Mech.* **627**, 161–178.
- ROME, L.C. & SWANK, D. 1992 The influence of temperature on power output of scup red muscle during cyclical length changes. *Journal of Experimental Biology* 171 (1), 261–281.
- Rome, L.C., Swank, D. & Corda, D. 1993 How fish power swimming. *Science* **261** (5119), 340–343.
- Schlatter, P., Stolz, S. & Kleiser, L. 2006a Analysis of the SGS energy budget

- for deconvolution- and relaxation-based models in channel flow. In *Direct and Large-Eddy Simulation VI* (ed. E. Lamballais, R. Friedrich, B. J. Geurts & O. Métais), pp. 135–142. Springer, Dordrecht, The Netherlands.
- Schlatter, P., Stolz, S. & Kleiser, L. 2006b LES of spatial transition in plane channel flow. J. Turbulence 7 (33), 1–24.
- Taneda, Sadatoshi & Tomonari, Yoshimasa 1974 An experiment on the flow around a waving plate. *Journal of the Physical Society of Japan* **36** (6), 1683–1689.
- TRIANTAFYLLOU, M. S., TECHET, A. H., ZHU, Q., BEAL, D. N., HOVER, F. S. & YUE, D. K. P. 2002 Vorticity control in fish-like propulsion and maneuvering. *Integr. Comp. Biol.* 42, 1026–1031.
- Walsh, M.J. 1982 Turbulent boundary layer drag reduction using riblets. AIAA Paper (71-0169).
- Wehrmann, O. H. 1965 Tollmien-schlichting waves under the influence of a flexible wall. *Physics of Fluids* 8 (7), 1389–1390.